High-power, fiber-laser-pumped optical parametric oscillators from the visible to mid-infrared

Suddapalli Chaitanya Kumar

Universitat Politecnica de Catalunya

Barcelona, September 2011

Doctorate Program: **Photonics**

Duration: **2007-2011**

Thesis advisor: **Prof. Majid Ebrahim-Zadeh**

Thesis submitted in partial fulfillment of the requirements for the degree of Doctor of Philosophy of the Universitat Politecnica de Catalunya

September 2011

Dedicated to my loving parents

Declaration

I hereby declare that the matter embodied in the thesis entitled, **"High-power, fiber-laser-pumped optical parametric oscillators from the visible to mid-infrared"** is the result of investigations carried out by me at the ICFO-Institute of Photonic Sciences, Castelldefels, Barcelona, Spain under the supervision of Prof. Majid Ebrahim-Zadeh, and that it has not been submitted elsewhere for the award of any degree or diploma.

In keeping with the general practice in reporting scientific observations, due acknowledgment has been made whenever the work described is based on the findings of other investigators.

_____

S. Chaitanya Kumar

Certificate

I hereby certify that the matter embodied in this thesis entitled, **"High-power, fiber-laser-pumped optical parametric oscillators from the visible to mid-infrared"** has been carried out by Mr. S. Chaitanya Kumar at the ICFO-Institute of Photonic Sciences, Castelldefels, Barcelona, Spain, under my supervision, and that it has not been submitted elsewhere for the award of any degree or diploma.

Prof. Majid Ebrahim-Zadeh

(ICFO, Research Supervisor)

Acknowledgements

My path to ICFO constitutes a series of fortunate events and my time here at ICFO has been great learning experience scientifically and personally.

First of all, I would like to express my sincere gratitude to Prof. Majid Ebrahim-Zadeh for giving me this opportunity to pursue doctoral studies under his supervision. This thesis would not have been possible without his constant guidance and encouragement, which gave me confidence and motivation to be ever ready for new challenges. His truly scientific intuition, deep understanding of the subject and vast academic as well as industrial experience has been inspirational. He always gave me freedom to get involved in various research projects and many fruitful collaborations, giving me extraordinary experience throughout the course of this work. His ever friendly attitude made it easy for me to express my thoughts, explore and implement new ideas. I am deeply indebted to him for all the support.

I have also been gifted with a wonderful team of labmates. It is my pleasure to thank Goutam Samanta with whom I worked on many projects right from the beginning. I have learnt a lot from him, which include technical skills in the lab and philosophy outside the lab. His absence in the lab is very much felt after he left to India. He has always been supportive. My special thanks to present labmates, Adolfo, Kavita, Ramaiah, Ossi and Enrique for creating such a great environment in the lab, sharing instruments, thoughts and expertise. I would like to thank Stefano Sanguinetti, for sharing his expertise in active stabilization of lasers. I would also like to thank A. Valencia for helping me translate the abstract of this thesis into Spanish.

Thanks to Prof. A. Agnesi and his group at University of Pavia, for providing the high energy pump laser to develop a mid-IR OPO for surgical applications. I would like to thank P. Dallocchio and F. Pirzio for building the pump laser at Pavia and bringing it to ICFO. Their efforts are very much appreciated. My special thanks are

also due to P. G. Schunemann, at BAE Systems Inc., for providing the best samples of the CSP nonlinear crystal. I would also like to express my sincere appreciation to Prof. A. S. Helmy and his group members, S. J. Wagner and J. B. Han, for the nice collaborations on the ultrafast experiments. Many thanks to Prof. Dmitriv Petrov, for helping me by lending instruments at the time of need.

I want to express my gratitude to Prof. Lluis Torner, Director of the ICFO-The Institute of Photonic Sciences, and his management team, for financial support during my research work, and for making the ICFO such a wonderful place for research. A significant part of the progress of science and technology at ICFO, is due to the supporting administrative staff. I would like to thank the Knowledge and Technology Transfer unit and Human Resource unit for their kind and timely help, taking care of all the responsibilities of administration and bureaucratic matters during my stay in ICFO and helping me to concentrate only on my research. I convey special acknowledgment to the purchasing unit for their indispensable help and rapid processing of equipment purchases and travel funds. This work would not be possible without the timely support from the mechanical and electronic workshop of ICFO. Therefore, I would like to thank all the members of the mechanical and electronic workshop.

I would also like to thank all my friends, Aditi(di), Ujwal(da), Manoj, Osamu, Anisha, Sudhir, Dhriti, Saurabh, Mousumi, Rajan, Pavan, Ritwick, Arup, Prim, Sabitha, and many others including M.Sc., and college friends for sharing their views (scientific and non-scientific). My special thanks are due to C. S. S. Raman, S. J. Mathew and R. Rajeev, who supported me at various turning points in my career.

I am grateful to all my teachers and professors at the school and University for sharing their immense knowledge. I would like to express my sincere thanks to my friend and philosopher, more than a teacher, Late. Sri Dasika Padmapada Somayaji, for his encouragement which led me to take research as my career path. I would also like to thank my professors during M.Sc., at Indian Institute of Technology

Guwahati, for making me capable of achieving my goals. I express my thanks to Dr. S. Venugopal Rao, Dr. G. Jose and Dr. A. Perumal for their encouragement and faith in me.

I would like to thank all my friends and family. Near or far, big or small, I thank all my friends for being supportive during my educational experiences, particularly Raghava and Srikanth. I would like to thank all my extended family members including my cousins, uncles, aunts and grandparents for their support. I would like to thank my mother, Suddapalli Subbalakshmi and father, Suddapalli Venkatappaiah, who have given me their unconditional love and always encouraged me with faith. If I have accomplished anything, the real credit lies with them. Special thanks to my brother, Suddapalli Karthikeyan, my sister, Gollapudi Vijayalakshmi Kameswari and brother-in-law Gollapudi Srikrishna Koundinya, for their constant support.

Abstract

High-power, continuous-wave (cw), mid-infrared (mid-IR) laser sources are of interest for variety of applications such as trace gas detection and remote sensing, which require broad spectral coverage to address the most prominent absorption features of a wide range of molecular species particularly in the mid-IR fingerprint region. On the other hand, surgical applications require high energy sources with unique pulse structure at specific wavelength in the mid-IR ranging from 6-6.5 μm.

Optical parametric oscillators (OPOs) offer potential sources for all the above applications. The output wavelengths of a singly-resonant oscillator (SRO) can be coarsely tuned over wide ranges through the adjustment of the nonlinear crystal temperature, phase-matching angle or, in the case of quasi-phase-matched (QPM) materials, the QPM grating period. The combination of SRO with a tunable pump laser allows the development of uniquely flexible and rapidly tunable class of mid-IR sources.

In this thesis we have demonstrated several mid-IR OPOs in the cw as well as ultrafast picosecond regime pumped by fiber-lasers making them compact and robust.

In the cw regime, we developed a high-power, Yb-fiber-laser pumped mid-IR OPO based on MgO:PPLN spanning 1506-1945 nm in the near-IR and 2304-3615 nm wavelength range in the mid-IR, efficiently addressing the thermal effects by implementing the optimum signal output coupling. Novel materials such a MgO:sPPLT, with better optical and thermal properties for cw mid-IR generation are explored. High-power broadband, cw mid-IR generation is also demonstrated by using the extended phase-matching properties of MgO:PPLN.

Further, we also demonstrated a simple, inexpensive and novel interferometric technique for absolute optimization of output power from a ring optical oscillator. We deployed a picosecond Yb-fiber-laser pumped mid-IR OPO based on MgO:PPLN in ring cavity configuration to demonstrate this proof-of-principle experiment for

the first time. The high-energy CSP OPO marked the first demonstration of a compact, high-repetition-rate OPO synchronously pumped by a master oscillator power amplifier system at 1064 nm, generating an milli-joule pulses in the 6-6.5 μm spectral range, which is technologically important for surgical applications.

Additionally, we also demonstrated a fiber-based-green source at 532 nm, based on single-pass second harmonic generation (SHG) in MgO:sPPLT, as an alternative pump source for Ti:sapphire laser, pointing towards the future, compact fiber-laser pumped Ti:sapphire lasers. Further efforts to improve the SHG efficiency led to the development of a novel multi-crystal scheme, enabling single-pass SHG efficiency as high as 56%. This generic technique is simple and can be implemented at any wavelength.

Resumen

Fuentes coherentes de luz continua y de alta potencia en el infrarrojo-medio (mid-IR) son de gran interés por su aplicación en la detección de gases, detección remota y la observación de imágenes. Estas aplicaciones requieren un ancho de banda amplio para evidenciar las características que ofrece la absorción de una gran variedad de especies moleculares, particularmente en la región "finger print" del mid-IR. Por otra parte, fuentes altamente energéticas con pulsos que posean estructuras peculiares en rangos específicos de longitud de onda en el mid-IR, entre 6-6.5 μm. , prometen características únicas para nuevas aplicaciones en cirugía.

Osciladores ópticos paramétricos (OPOs) constituyen fuentes de luz versátiles y apropiadas para todas las aplicaciones mencionadas anteriormente. La longitud de onda de un OPO puede ser sintonizada en regiones amplias del espectro cambiando la temperatura del cristal no-lineal, el ángulo de ajuste de fase o, al considerar materiales cuasi ajuste de fase (QPM), cambiando el periodo de red.

En esta tesis, hemos demostrado una gran variedad de OPOs en el mid-IR en régimen continuo y de pulsos de picosegundo. Estos OPOs han sido bombeados por láseres de fibra permitiendo un diseño compacto y resistente.

En el régimen de emisión continua, hemos implementado un OPO de alta potencia basado en MgO:PPLN bombeado por un láser de fibra. Este OPO es sintonízable en el rango 1506-1945 nm correspondiente al infrarrojo-cercano y en el rango 2304-3615 nm correspondiente al mid-IR. Esta capacidad de sintonización se logra al sobrepasar eficientemente los efectos térmicos optimizando el acoplamiento de salida. Materiales nuevos como el MgO:sPPLT, con propiedades ópticas y térmicas mejoradas para la generación de radiación continua en el mid-IR han sido estudiados. Utilizando las propiedades ajuste de la fase extendió del MgO:sPPLT, fuentes continuas de alta potencia con un gran ancho de banda en el infrarrojo-medio también han sido implementadas.

En el régimen ultrarápido, hemos demostrado una nueva técnica de interferometría para la optimización absoluta de la potencia de salida de un oscilador óptico con una cavidad de anillo. Como demostración de principio, implementamos, por primera vez, un OPO de picosegundos en el mid-IR basado en MgO:PPLN con una cavidad de anillo bombeado por un láser de fibra de Yb. Además, hemos desarrollado un nuevo OPO de alta energía en el mid-IR basado en el material nolineal CSP. Esto representa la primera demostración de un OPO compacto de alta repetición sincrónicamente bombeado por un láser de estado sólido a 1064 nm generando pulsos de milijulios en el rango espectral 6-6.5 μm. Esta radiación es importante para aplicaciones en cirugía.

Adicionalmente, hemos demostrado una fuente verde, 532 nm, basada en láseres de fibra. Esta radiación se obtiene por medio de la generación de segundo harmónico (SHG) en un paso individual en MgO:sPPLT. Esto representa una nueva alternativa de bombeo para los láseres de Ti:sapphire que los harán compactos en el futuro. Los esfuerzos para mejorar la eficiencia de segundo harmónico resultaron en el desarrollo de un novedoso esquema que utiliza múltiples cristales y permite eficiencias de SHG de paso individual del 56%. Este esquema es general y simple y puede ser implementado para cualquier longitud de onda.

Publications

Journal publications

1. **S. Chaitanya Kumar** and M. Ebrahim-Zadeh: "High-power, fiber-laser-pumped, picosecond optical parametric oscillator based on MgO:sPPLT," Opt. Exp. (In press).

2. **S. Chaitanya Kumar**, G. K. Samanta, K. Devi, S. Sanguinetti and M. Ebrahim-Zadeh: "Single-frequency, high-power, continuous-wave fiber-laser-pumped Ti:sapphire laser," Appl. Opt. (In press).

3. A. Esteban-Martin, G. K. Samanta, K. Devi, **S. Chaitanya Kumar** and M. Ebrahim-Zadeh: "Frequency-modulation-mode-locked optical parametric oscillator," Opt. Lett. (In press).

4. G. K. Samanta, **S. Chaitanya Kumar**, K. Devi, and M Ebrahim-Zadeh: "High-power, continuous-wave Ti:sapphire laser pumped by a fiber-laser green source at 532 nm," Opt Lasers Eng. 50(2), 215-219, Feb 2012.

5. **S. Chaitanya Kumar**, A. Agnesi, P. Dallocchio, F. Pirzio, G. Reali, K. T. Zawilski, P. G. Schunemann, and M. Ebrahim-Zadeh: "1.5 mJ, 450 MHz, $CdSiP_2$ picosecond optical parametric oscillator near 6.3 μm," Opt. Lett. 36(16), 3236-3238, Aug 2011.(Also listed in October issue of Virtual Journal of Biomedical Optics, 6(9), 2011).

6. **S. Chaitanya Kumar** and M. Ebrahim-Zadeh: "High-power, continuous-wave, mid-infrared optical parametric oscillator based on MgO:sPPLT," Opt. Lett. 36(13), 2578-2580, July 2011.

7. K. Devi, **S. Chaitanya Kumar**, and M. Ebrahim-Zadeh: "13.1 W, high-beam-quality, narrow-linewidth continuous-wave fiber-based source at 970 nm," Opt.

Exp. 19 (12), 11631-11637, Jun 2011. (Also listed in July issue of Virtual Journal of Biomedical Optics, 6(7), 2011).

8. **S. Chaitanya Kumar**, G. K. Samanta, K. Devi, and M. Ebrahim-Zadeh: "High-efficiency, multicrystal, single-pass, continuous-wave second harmonic generation," Opt. Exp. 19 (12), 11152-11169, Jun 2011.

9. **S. Chaitanya Kumar**, A. Esteban-Martin, and M. Ebrahim-Zadeh: "Interferometric output coupling of ring optical oscillators," Opt. Lett. 36 (7), 1068-1070, Mar 2011.

10. **S. Chaitanya Kumar**, K. Devi, G. K. Samanta, and M. Ebrahim-Zadeh: "Fiber laser based green pumped continuous wave singly resonant optical parametric oscillator," Laser Physics, 21 (4), 782-789, Mar 2011.

11. **S. Chaitanya Kumar**, R. Das, G. K. Samanta, and M. Ebrahim-Zadeh: "Optimally-output-coupled, 17.5 W, fiber-laser-pumped continuous-wave optical parametric oscillator," Appl. Phys. B: Lasers Opt. 102 (1), 31-35, Jan 2011.

12. G. K. Samanta, **S. Chaitanya Kumar**, K. Devi, and M. Ebrahim-Zadeh: "Multi-crystal, continuous-wave, single-pass second-harmonic-generation with 56% efficiency," Opt. Lett. 35 (20), 3513-3515, Oct 2010.

13. J. Han, P. Abolghasem, B. J. Bijlani, A. Arjmand, **S. Chaitanya Kumar**, A. Esteban-Martin, M. Ebrahimzadeh, and A. S. Helmy: "Femtosecond second-harmonic generation in AlGaAs bragg reflection waveguides: Theory and experiment," J. Opt. Soc. Am. B 27 (6), 1291-1298, May 2010.

14. R. Das, **S. Chaitanya Kumar**, G. K. Samanta, and M. Ebrahim-Zadeh: "Broadband, high-power, continuous-wave, mid-infrared source using extended phase-matching bandwidth in MgO:PPLN," Opt. Lett. 34 (24), 3836-3838, Dec 2009.

15. **S. Chaitanya Kumar**, G. K. Samanta, and M. Ebrahim-Zadeh: "High-power, single-frequency, continuous-wave second-harmonic-generation of ytterbium fiber laser in PPKTP and MgO:sPPLT," Opt. Exp. 17 (16), 13711-13726, Aug 2009.

16. G. K. Samanta, **S. Chaitanya Kumar**, R. Das, and M. Ebrahim-Zadeh: "Continuous-wave optical parametric oscillator pumped by a fiber laser green source at 532 nm," Opt. Lett. 34 (15), 2255-2257, Aug 2009.(Also listed in September issue of Virtual Journal of Ultrafast Science, 8(9), 2009).

17. G. K. Samanta, **S. Chaitanya Kumar**, and M. Ebrahim-Zadeh: "Stable, 9.6 W, continuous-wave, single-frequency, fiber-based green source at 532 nm," Opt. Lett. 34 (10), 1561-1563, May 2009.(TOP-10 downloaded articles (OSA) in May, 2009).

18. G. K. Samanta, **S. Chaitanya Kumar**, M. Mathew, C. Canalias, V. Pasiskevicius, F. Laurell, and M. Ebrahim-Zadeh: "High-power, continuous-wave, second-harmonic generation at 532 nm in periodically poled $KTiOPO_4$," Opt. Lett. 33 (24), 2955-2957, Dec 2008.(TOP-10 downloaded articles (OSA) in December, 2008).

Proceeding publications

1. **S. Chaitanya Kumar**, A. Agnesi, P. Dallocchio, F. Pirzio, G. Reali, K. T. Zawilski, P. G. Schunemann, andand M. Ebrahim Zadeh: "High-energy 450-MHz $CdSiP_2$ picosecond optical parametric oscillator near 6.3 μm for biomedical applications," Proc. SPIE 8240-24 (In press).

2. Kavita Devi, **S. Chaitanya Kumar**, G. K. Samanta, and M. Ebrahim Zadeh: "Highly efficient continuous-wave single-pass second-harmonic generation using multicrystal scheme," Proc. SPIE 8173, 81730K, Dec 2010.

3. Kavita Devi, **S. Chaitanya Kumar**, G. K. Samanta, and M. Ebrahim Zadeh: "Continuous-wave-fiber-laser-pumped Ti:sapphire laser," Proc. SPIE 8173, 81730J, Dec 2010.

4. S. J. Wagner, **S. Chaitanya Kumar**, O. Kokabee, B. M. Holmes, U. Younis, M. Ebrahim Zadeh, D. C. Hutchings, A. S. Helmy, and J. S. Aitchison: "Performance and limitations of quasi-phase matching semiconductor waveguides with picosecond pulses," Proc. SPIE 7750, 77501K, Nov 2010.

Research Highlights

1. Nature Photonics, page 326-327, June 2011.

2. Laser Focus World, page 30-32, January 2011.

Conference Publications

1. **S. Chaitanya Kumar**, A. Agnesi, P. Dallocchio, F. Pirzio, G. Reali, K. T. Zawilski, P. G. Schunemann, andand M. Ebrahim Zadeh: "Compact, high-energy, picosecond optical parametric oscillator at 450 MHz near 6 μm," ASSP, San Diego, USA, January 2012.

2. **S. Chaitanya Kumar**, A. Agnesi, P. Dallocchio, F. Pirzio, G. Reali, K. T. Zawilski, P. G. Schunemann, andand M. Ebrahim Zadeh: "High-energy 450-MHz $CdSiP_2$ picosecond optical parametric oscillator near 6.3 μm for biomedical applications," SPIE Photonics West, San Francisco, USA, January 2012.

3. **S. Chaitanya Kumar** and M. Ebrahim-Zadeh: "Fiber-laser-pumped, high-power, continuous-wave, singly-resonant optical parametric oscillator based on MgO:sPPLT," CLEO/Europe-EQEC, Munich, Germany, May 2011.

4. **S. Chaitanya Kumar**, G. K. Samanta, K. Devi, S. Sanguinetti, and M. Ebrahim-Zadeh: "High-power, single-frequency Ti:Sapphire laser pumped by a continuous-wave fiber laser green source," CLEO/Europe-EQEC, Munich, Germany, May 2011.

5. A. Esteban-Martin, **S. Chaitanya Kumar**, and M. Ebrahim-Zadeh: "Optimum output coupling in optical oscillators using antiresonant ring interferometry," CLEO/Europe-EQEC, Munich, Germany, May 2011.

6. **S. Chaitanya Kumar**, A. Esteban-Martin, O. Kokabee, and M. Ebrahim-Zadeh: "Interferometric output coupling of a high-power picosecond ring optical parametric oscillator," CLEO, Baltimore, USA, May 2011.

7. **S. Chaitanya Kumar**, and M. Ebrahim-Zadeh: "Fiber-Laser-Pumped, High-Power, Continuous-Wave, Mid-Infrared Optical Parametric Oscillator Based on MgO:sPPLT," CLEO, Baltimore, USA, May 2011.

8. K. Devi, **S. Chaitanya Kumar**, G. K. Samanta, and M. Ebrahim-Zadeh: "Highly-efficient, continuous-wave, single-pass second-harmonic-generation using multi-crystal scheme," Photonics 2010, Guwahati, India, December 2010.

9. K. Devi, **S. Chaitanya Kumar**, G. K. Samanta, and M. Ebrahim-Zadeh: "Continuous-wave, fiber-laser-pumped Ti:Sapphire laser," Photonics 2010, Guwahati, India, December 2010.

10. **S. Chaitanya Kumar**, Ritwick Das, G. K. Samanta, and M. Ebrahim-Zadeh: "High-power, broadband, continuous-wave, mid-infrared optical parametric oscillator based on MgO:PPLN," CLEO, San Jose, USA, May 2010.

11. **S. Chaitanya Kumar**, Ritwick Das, G. K. Samanta, and M. Ebrahim-Zadeh: "Stable, 17.5 W, Optimally-output-coupled, Yb-fiber-pumped mid-infrared optical parametric oscillator," CLEO, San Jose, USA, May 2010.

12. G. K. Samanta, **S. Chaitanya Kumar**, Kavita Devi, and M. Ebrahim-Zadeh: "55%-efficient, 13-W, Single-pass SHG of a CW Fiber Laser at 532 nm in a double-crystal scheme," CLEO, San Jose, USA, May 2010.

13. G. K. Samanta, **S. Chaitanya Kumar**, Kavita Devi, and M. Ebrahim-Zadeh: "Fiber-laser-pumped Ti:sapphire laser," CLEO, San Jose, USA, May 2010.

14. **S. Chaitanya Kumar**, Ritwick Das, G. K. Samanta, and M. Ebrahim-Zadeh: "Optimally-output-coupled, 17.5 W, Yb-fiber-laser-pumped continuous-wave optical parametric oscillator," 1^{st} EOS Topical Meeting on Lasers, Capri, Italy, September 2009.(Post deadline paper)

15. G. K. Samanta, **S. Chaitanya Kumar**, Ritwick Das and M. Ebrahim-Zadeh: "Fiber based SHG pumped, high-power, continuous-wave, single-frequency optical parametric oscillator," 1^{st} EOS Topical Meeting on Lasers, Capri, Italy, September 2009.

16. **S. Chaitanya Kumar**, G. K. Samanta, C. Canalias, V. Pasiskevicius, F. Laurell, and M. Ebrahim-Zadeh: "6.2 W, Continuous-wave, single-frequency, Yb-fiber-based green source at 532 nm using periodically-poled $KTiOPO_4$," 1^{st} EOS Topical Meeting on Lasers, Capri, Italy, September 2009.

17. **S.Chaitanya Kumar**, R. Das, G. K. Samanta, and M. Ebrahim-Zadeh: "16.6 W, Near- and mid-Infrared optical parametric oscillator pumped by an Yb fiber laser," 17^{th} International Conference on Advanced Laser Technologies, Antalya, Turkey, September 2009.

18. G. K. Samanta, **S. Chaitanya Kumar**, R. Das, and M. Ebrahim-Zadeh: "Continuous-wave, single-frequency optical parametric oscillator pumped by a frequency-doubled fiber laser," 17^{th} International Conference on Advanced Laser Technologies, Antalya, Turkey, September 2009.

19. **S. Chaitanya Kumar**, Ritwick Das, G. K. Samanta, and M. Ebrahim-Zadeh: "16.6W, Continuous-wave, Yb-fiber-laser-pumped, singly-resonant optical parametric oscillator based on MgO:PPLN," CLEO/Europe-EQEC, Munich, Germany, June 2009.

20. Ritwick Das, G. K. Samanta, **S. Chaitanya Kumar**, and M. Ebrahim-Zadeh: "32.7% efficient, continuous wave, Yb-fiber laser pumped single pass second-harmonic-generation in MgO:sPPLT," CLEO/Europe-EQEC, Munich, Germany, June 2009.

21. **S. Chaitanya Kumar**, Ritwick Das, G. K. Samanta, and M. Ebrahim-Zadeh: "Generation of 16.6 W, tunable mid-infrared radiation with a Yb-fiber-laser-pumped, continuous-wave, optical parametric oscillator," Mid-Infrared Coherent Sources, MICS'2009, Trouville, France, June 2009.

22. G. K. Samanta, **S. Chaitanya Kumar**, Ritwick Das, and M. Ebrahim-Zadeh: "Stable, continuous-wave, single-frequency, singly resonant optical parametric

oscillator pumped in the green by frequency-doubled fiber laser," CLEO/Europe-EQEC, Munich, Germany, June 2009.

23. **S. Chaitanya Kumar**, G. K. Samanta, and Majid Ebrahim-Zadeh: "Stable, high-power, continuous-wave, single-frequency source at 532 nm using MgO:sPPLT crystal," CLEO, Baltimore, USA, May 2009.

24. **S. Chaitanya Kumar**, G. K. Samanta, M. Ebrahim-Zadeh: "Efficient frequency conversion of continuous-wave laser light into the green using periodically-poled $KTiOPO_4$," Nolineal, Barcelona, España, June 2008.

High-power, fiber-laser-pumped optical parametric oscillators from the visible to mid-infrared

Contents

List of Tables

List of Figures

1 Introduction

Lasers have become an integral part of our life. While they appear in different aspects of our regular activities like shopping and listening to music, they play a vital role in the industries and hospitals improving quality of our life. The art of making laser light work to address various technological challenges involve tailoring the properties of light according to specific needs. Many practical applications require high output power accompanied by the need for high efficiency, good beam quality and, more importantly, wavelength tunability. Development of such tunable laser sources catering ever-demanding applications is a very active field of research [1]. Ever since the invention of the laser, there has always been a great deal of interest in the development of continuously tunable coherent light sources. Such sources would have a great impact not only on research and industry, but also on the society as a whole. The development of tunable lasers has been difficult because conventional lasers tend to be discrete-wavelength devices, involving stimulated emission between quantized energy levels in the laser media. A continuously tunable laser can be realized only when these quantized energy levels are tunable, or when the neighboring energy levels are sufficiently broadened to merge into each other forming a continuous band. Even then, the tunability tends to be limited [2]. Moreover, even after half-a-century since the invention of laser, many regions of the optical spectrum extending from ultraviolet (UV) to mid-infrared (mid-IR) remain inaccessible to lasers due to the unavailability of suitable gain media. Nonlinear optics, and in particular nonlinear frequency conversion, has majorly contributed in this direction,

leading to the development of coherent light sources, known as optical parametric oscillators (OPOs), enabling access to the spectral regions that are unavailable to conventional lasers, and potentially capable of providing wavelength tunability across extended spectral regions from a single device. Further, they offer practical output power with high efficiency and can be operated in all temporal regimes, ranging from continuous-wave (cw), quasi-cw, and pulsed nanosecond to ultrafast picosecond and femtosecond time-scales. Such devices are of great interest for variety of application in spectroscopy, biomedicine, remote sensing and environmental monitoring [3].

An OPO essentially consists of an optical oscillator and a nonlinear crystal. It is a device based on three-wave mixing process involving three optical fields. The energy of the input pump photon with frequency, ω_p, is divided among two new photons with frequencies, ω_s and ω_i, with the frequencies satisfying the energy conservation ($\omega_p = \omega_s + \omega_i$) and momentum conservation ($k_p = k_s + k_i$) conditions in a second-order nonlinear gain medium. Traditionally, among the two generated photons, the one with higher energy is called 'signal' and the photon with lower energy is called 'idler'. The momentum conservation condition, which actually governs the efficient generation of the two new photons, is also known as 'phase-matching' condition. In other words, an OPO converts a fixed 'pump' laser wavelength in to two different wavelengths known as 'signal' and 'idler'. Operation of an OPO critically depends on the spectral and spatial quality of the pump laser as well as the properties of the nonlinear material to achieve phase-matching [4].

The basic idea of the parametric processes was known long before the advent of the laser. The earliest report on the observation of purely nonlinear optical effect dates back to 1926, when S. Vavilov and V. L. Levishin, found a reduction in the light absorption by Uranium doped glass as the intensity of light was increased [5].

In 1943, E. Schrodinger introduced the word 'Nonlinear Optics' for the first time [6, 7]. Nonlinear optics is the study of the nonlinear response of materials to optical fields. This phenomenon of nonlinear response usually requires very high field

Event	**Reference**	**Year**
Earliest observation of optical nonlinearity	S. Vavilov et. al.	1926
Introduction of the word "Nonlinear Optics"	E. Schrodinger	1943
First proposal of the concept of phase-matching in the context of radio waves	P. K. Tien	1958
First demonstration of laser	T. H. Maiman	1960
First experimental observation of second harmonic generation	P. Franken et. al.	1961
First demonstration of optical mixing	M. Bass et. al.	1962
Experimental proof of phase-matching	J. A. Giordmaine	1962
First proposal and theory of optical parametric oscillator	N. M. Kroll	1962
First demonstration of third harmonic generation	R. W. Terhune et. al.	1962
First observation of difference frequency generation	A. W. Smith et. al.	1963
First experimental demonstration of an optical parametric oscillator	J. A. Giordmaine et. al	1965
First demonstration of femtosecond OPO	D. C. Edelstein et. al.	1989
First demonstration of Periodic poling technology	S. Matsumoto, et. al	1991
First singly resonant continuous-wave OPO	S. T. Yang et. al.	1993

Table 1.1: Advances in nonlinear optics.

strength. As a result, the invention of laser in 1960 by T. Maiman, opened up new avenues to study various nonlinear optical phenomena [8]. If the laser was a solution, then nonlinear optics was one of the major problems that it was seeking. Soon after the demonstration of the laser, while endless applications were being discussed, P. A. Franken was thinking about some exciting experiments, for which he rented a ruby laser form Trion instruments Inc., the first ever company to manufacture ruby lasers. The laser produced 3 J, 1 ms-long pulses at 694.3 nm. By focusing this beam into quartz crystal, he successfully demonstrated the experimental observation of second harmonic generation (SHG) at 347.2 nm, for the first time, along with his graduate students at University of Michigan in 1961 [9]. The year 1962 was a great year in the history of nonlinear optics, which saw a lot of interesting advances, as listed in Table. 1.1. In January 1962, M. Bass and his associates reported on the first experimental observation of optical mixing. In his experiments, he deployed two ruby lasers from the same company, Trion instruments Inc., and operated one of them at room temperature and the other at liquid nitrogen temperature, thereby operating the two lasers at two different wavelengths separated by 1 nm. He then tried using various crystals to observe optical harmonics and found that 'Triglycine sulfate' was the most effective crystal for his apparatus, using which he demonstrated the first experimental observation of sum frequency generation (SFG) [10]. Although SHG and SFG were observed by then, the conversion efficiencies were very low. In order to realize an efficient nonlinear optical process, phase-matching is a mandatory condition to be satisfied, as highlighted earlier. In the same issue of Physical Review Letters, J. A. Giordmaine reported his observations about the generation of intense SHG radiation with out focusing in Potassium Dyhydrogen Phosphate (KDP) crystal. This was made possible by high intensity monochromatic light and exploiting the inherent material properties of the anisotropic KDP crystal to match the phase velocities of the fundamental and the second harmonic light. This was the first experimental demonstration of phase-matching during SHG [11]. The technique of

phase-matching was also suggested by Maker et al. [12] in the same year. In fact this report was published right next to the report of M. Bass on optical mixing. However, the concept of phase-matching was proposed even before the invention of laser, way back in 1958 by P. K. Tien in the context of radio waves [13, 14]. Following the demonstration of phase-matched SHG, R. W. Terhune and his associates at Ford motor company, reported the observation of third harmonic generation in calcite, for the first time, in May 1962 [15]. Soon after, the first predictions of parametric amplification and oscillation were given by R. H. Kingston [16], S. A. Akhmanov and R. V. Khokhlov [17] in Russia, and N. M. Kroll, at the University of California, USA, along with the theoretical framework, in August 1962 [18].

As the performance and understanding of harmonic generation and mixing improved with the explosion of new experimental results, also came the theoretical formulation such as the famous Physical Review paper in September 1962 by Armstrong, Bloembergen, Ducuing, and Pershan, postulating the general permutation symmetry relations in nonlinear optics [19].

During early 1963, the first observation of difference frequency generation (DFG) was reported by A. W. Smith and N. Braslau [20]. With major theoretical framework at hand and all different types of laser that were being developed, J. A. Giordmaine and R. C. Miller reported the first experimental demonstration of an OPO in 1965 [21]. The pump source was the second harmonic of $Nd_3^+ : CaWO_4$ laser and the nonlinear crystal was a 0.539 cm long lithium metaniobate, antireflection coated for high reflectivity (>99.6 %) in the range 0.96 μm to 1.16 μm and 50% transmission at 0.529 μm. The OPO was tunable from 0.97 μm to 1.15 μm.

Although the progress in OPO technology had been hindered for more than 20 years, the development of new nonlinear optical materials and new laser sources with improved spectral and spatial coherence in 1980s again prompted a major insurgence in the development of pulsed OPOs [22, 23, 24, 25]. This was followed by the first demonstration of synchronously pumped femtosecond OPO by D. C. Edelstein in

1989 [26]. On the other hand, the first cw singly resonant oscillator (SRO) based on KTP was demonstrated by S.T.Yang and his associates at Stanford University in 1993 [27]. However, in the cw regime, due to low nonlinear optical gain and the requirement for powerful pump lasers, development of high-power cw OPOs in SRO configuration was not possible until the the advent of engineered nonlinear materials to achieve quasi-phase-matching (QPM) by periodical poling in 1991 [28]. The first cw OPO based on periodically poled lithium niobate (PPLN), was demonstrated by W. R. Bosenberg and co-workers in 1996 [29].

Today, from a myriad of nonlinear optical materials, there are established technologies for pulsed OPOs in spectral regions from the mid-IR [1, 2, 3] to visible [30] and further down to UV [31] using $\beta - BaB_2O_4$ (BBO), LiB_3O_5 (LBO) and BiB_3O_6 (BIBO) as nonlinear crystals. On the other hand, development of high-power cw OPOs is still a challenge. A vast majority of them are majorly confined to near and mid-IR spectral region and are based on MgO-doped periodically poled lithium niobate (MgO:PPLN) [32, 33, 34] and MgO-doped periodically poled lithium tantalate (MgO:sPPLT) [35].

The research work presented in this thesis deals with both cw and pulsed OPOs in SRO configuration. The cw OPOs are pumped at 1 μm and are based on MgO:PPLN and MgO:sPPLT, generating high-power mid-IR radiation in 1.4 – 3.8 μm spectral range. The pulsed OPOs are also pumped at 1 μm, generating picosecond mid-IR pulses in the 6 – 6.5 μm wavelength range using a new nonlinear material, Cadmium Silicon Phosphide, $CdSiP_2$ (CSP). Moreover, majority of the devices presented here are based on fiber laser technology making them compact, practical and robust. Apart from OPOs, novel designs for efficient single-pass SHG in to the green, based on MgO:sPPLT has been investigated and this fiber-based green source is proposed as an alternative pump source for Ti:sapphire laser. The thesis is organized into 10 chapters.

Chapter 2 provides introduction to various nonlinear optical phenomena including

SHG, SFG, DFG and OPO, along with the necessary theoretical frame work. As the successful operation of an OPO device requires proper cavity design, we have also discussed the design issues in this chapter. Using this theoretical background and the cavity design criteria, several OPOs based on MgO:PPLN, MgO:sPPLT and CSP have been developed during the course of this research work.

In chapter 3 we demonstrate a stable, high-power, fiber-laser-pumped, cw SRO, based on MgO:PPLN, for the mid-IR spectral region. Generation of high output power was challenging, because of heavy thermal load of the nonlinear crystal due high intracavity signal power. But, we have efficiently managed the thermal effects by optimizing the signal output coupling thereby extracting record practical output powers not only in the mid-IR idler wavelength region, but also in the near-IR signal wavelength range [34].

In chapter 4 we demonstrate a compact and viable source of broadband, high-power, cw, mid-IR radiation based on an SRO pumped by a wide-bandwidth cw Yb fiber laser centered at 1060 nm. By exploiting the extended phase-matching bandwidth in a 50 mm long crystal of MgOPPLN and a ring SRO cavity, we obtain high power broadband idler output. The results of output power scaling, reconstructed mid-IR idler spectrum and beam quality measurements are discussed in this chapter [36].

In chapter 5 we demonstrate a stable, high-power, cw SRO for the mid-IR using MgO:sPPLT nonlinear crystal pumped by a Yb fiber laser at 1064 nm. Owing to the better thermal conductivity of this nonlinear material, reduced thermal effects, enabled room temperature operation, while generating high mid-IR output power. The power scaling results of MgO:sPPLT cw SRO are compared with that of MgO:PPLN based cw SRO and long term power stability and frequency stability measurements of the mid-IR idler are presented in this chapter [37].

In chapter 6 we demonstrate the successful deployment of an antiresonant ring (ARR) interferometer within a ring optical resonator, and its use for absolute op-

timization of output power. The integration of the ARR interferometer in a folded arm of the ring oscillator provides continuously variable output coupling over broad spectral range and under any operating conditions. We demonstrate the technique using a picosecond OPO based on MgO:PPLN, where we show continuously adjustable output coupling and optimization of the output power for different pump power conditions. We also show that the inclusion of the ARR interferometer has no detrimental effect on the spatial, temporal, and spectral characteristics of OPO output [38].

In chapter 7 we present a compact, efficient, high-energy, and high-repetition-rate picosecond OPO for the mid-IR based on the new nonlinear material, CSP. The OPO is synchronously pumped by a master-oscillator power-amplifier system at 1064.1 nm and can be tuned across 6091-6577 nm, covering the technologically important wavelength range for surgical applications. Further, we have also estimated the energy bandgap of the new nonlinear material. Results on power scaling, wavelength tuning and beam quality of the CSP OPO are presented in this chapter [39].

In chapter 8 we demonstrate a high-power, cw, single-frequency, green source based on single-pass SHG of a Yb-fiber-laser in MgO:sPPLT, and successfully deployed it as an alternative pump source for a cw Ti:Sapphire ring laser. The laser is carefully designed and optimized, to achieve high output power with competitive performance. Further, it is actively frequency stabilized using a home-made super-invar interferometer, enabling continuous tuning. Power scaling, coarse and continuous tuning, power stability and beam quality measurements of the single-frequency Ti:Sapphire laser are presented in this chapter [40, 41, 42].

In chapter 9 we describe the critical design parameters and present detailed experimental and theoretical studies for efficient, cw, single-pass SHG based on novel cascaded multicrystal scheme, providing >55% conversion efficiency and multiwatt output powers at 532 nm for a wide range of input fundamental powers at 1064 nm. Systematic characterization of the technique in single-crystal, double-crystal

and multicrystal schemes has been performed using MgO:sPPLT crystals and the results are compared. Optimization of vital parameters including focusing and phase-matching temperature at the output of each stage is investigated in this chapter [43, 44]. Finally, we conclude the thesis with future outlook in chapter 10.

2 Basics of nonlinear optics

2.1 Origin of nonlinearity

Optics is the the study of interaction of light and matter. When an electromagnetic field propagates through a linear medium, its properties are not influenced neither by its own intensity nor by the presence of any other fields. However, when different electromagnetic field propagate through a nonlinear medium, they can interact and the propagation characteristics of one field can be influenced by the other fields [45, 48]. This interaction is the basis for the various nonlinear optical phenomena. When a material is subjected to electromagnetic radiation, the electrons are displaced with respect to the nuclei and the system is thus polarized. The electromagnetic response of a material to the applied field can be described by the dependence of the dipole moment per unit volume, or the polarization, of the material on the magnitude of the applied electric field. In the case where the electric field is small, the induced polarization of the medium is linearly proportional to the applied field.,

$$P = \varepsilon_0 \chi^{(1)} E(t) \tag{2.1}$$

where P and E are the polarization and electric field vectors, respectively, $\chi^{(1)}$ is the linear susceptibility of the medium, and ε_0 is the permittivity of free space. This is the regime of linear optics. In general, χ is a tensor and is dependent on frequency, ω, of the optical radiation. In the case where the electric field strength is comparable to intra-atomic electric field, as with laser radiation, the response of the material is

no longer linear. The nonlinear optical response of the material can be described by expressing the polarization as power series in the applied electric field,

$$P = \varepsilon_0(\chi^{(1)}E(t) + \chi^{(2)}E(t)^2 + \chi^{(3)}E(t)^3 + \cdots\cdots) \tag{2.2}$$

Hence the invention of laser propelled the field of modern nonlinear optics, and initiated intensive research, leading to the observation of various nonlinear optical effects. Today, nonlinear optics is a vast and one of the most important fields of physics with diverse range of applications in many other areas of science. The work presented in this thesis is mainly based on second-order nonlinear processes. So, this brief discussion will only be limited to interactions involving second-order nonlinear susceptibility, $\chi^{(2)}$, and treatment of other interactions can be found in multitude of references [19, 45, 49].

2.2 Second-order nonlinear processes

All the second-order nonlinear optical processes based on $\chi^{(2)}$ involve three interacting fields

$$P^{NL}(t) = \varepsilon_0\chi^{(2)}E(t)^2 \tag{2.3}$$

Consider an optical field incident upon a second-order nonlinear optical medium consisting of two distinct frequency components, ω_1 and ω_2, represented as

$$E(t) = E_1(t)e^{-i\omega_1 t} + E_2(t)e^{-i\omega_2 t} + c.c \tag{2.4}$$

Then, using equations 2.3 and 2.4, we find that second-order nonlinear polarizability is given by

$$
\begin{aligned}
P^{NL}(t) &= \sum_n P(\omega_n) e^{-i\omega_n t} \\
&= \varepsilon_0 \chi^{(2)} \Big[E_1^2 e^{-2i\omega_1 t} + E_2^2 e^{-2i\omega_2 t} + 2E_1 E_2 e^{-i(\omega_1+\omega_2)t} \qquad (2.5) \\
&\quad + 2E_1 E_2^* e^{-i(\omega_1-\omega_2)t} + c.c \Big] + 2\varepsilon_0 \chi^{(2)} \left[E_1 E_1^* + E_2 E_2^* \right] \qquad (2.6)
\end{aligned}
$$

Here, in equation 2.6, the first two terms represent the second harmonic generation (SHG) process. The thrid term represents the sum frequency generation (SFG) and the fourth term represents the difference frequency generation (DFG) process. The physical meaning of these second-order nonlinear optical processes is illustrated in Fig. 2.1. SFG is a process in which two input photons at frequencies ω_1 and ω_2 are coverted into one photon at frequency $\omega_3 = \omega_1 + \omega_2$, as shown in Fig. 2.1(a). SHG is the degenerate case of SFG process, in which ω_1=ω_2=ω, hence generating output at 2ω, as shown in Fig. 2.1(b). In DFG process, two input photons at frequencies ω_2 and ω_3 are coverted into one photon at a frequency $\omega_1 = \omega_3 - \omega_2$, as shown in Fig. 2.1(c). This process also leads to the possibility of achieving parametric gain to realize optical parametric amplification (OPA). Another special case that found important applications is when $\omega_1 = 0$ and $\omega_3 = \omega_2 = \omega$. Then, one of the input fields is static and the refractive index is effected through the linear electro-optic effect. This is also known as Pockels effect. Figure. 2.1(d) shows another type of process known as parametric down conversion or optical parametric generation (OPG), which starts with one input photon at ω_3 and generates two lower energy photons at ω_1 and ω_2. The two generated photons are generally called "signal" (the shorter wavelength) and "idler" (the longer wavelength). An OPG in combination with an optical oscillator to resonate one or both the generated fields, thereby enhancing the efficiency of the process, constitutes an optical parametric oscillator (OPO).

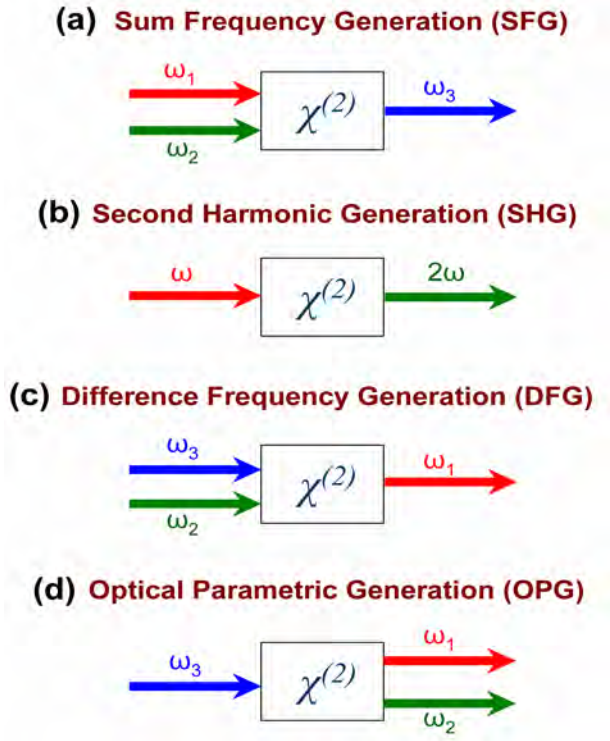

Figure 2.1: Schematic of various second order nonlinear optical processes.

2.3 Nonlinear susceptibility

The second-order nonlinear susceptibility, $\chi^{(2)}$, tensor has 27 elements. Explicitly written, $\chi^{(2)} = \chi^{(2)}_{ijk}$, where the indices i, j, k correspond to x, y, z, and represent the optical polarization directions. A common practice in nonlinear optics is to use the d-matrix notation instead of the susceptibility tensor according to

$$d_{ijk} = \frac{1}{2}\chi^{(2)}_{ijk} \tag{2.7}$$

Based on the Kleinman symmetry [49, 50, 52] condition, which states that when nonlinear interactions occur for frequencies that are far from any resonant frequency of the material, the nonlinear susceptibility is essentially independent of frequency. Kleinman symmetry implies that the indices of $\chi^{(2)}_{ijk}$can be permuted without permuting the frequencies since $\chi^{(2)}_{ijk}$ is independent of frequency. Hence, the tensor can

be contracted in to 3 × 6-element matrix, yielding

$$\begin{pmatrix} P_x(\omega_3) \\ P_y(\omega_3) \\ P_z(\omega_3) \end{pmatrix} = 2\varepsilon_0 K \begin{bmatrix} d_{11} & d_{12} & d_{13} & d_{14} & d_{15} & d_{16} \\ d_{21} & d_{22} & d_{23} & d_{24} & d_{25} & d_{26} \\ d_{31} & d_{32} & d_{33} & d_{34} & d_{35} & d_{36} \end{bmatrix} \begin{pmatrix} E_x(\omega_1)E_x(\omega_2) \\ E_y(\omega_1)E_y(\omega_2) \\ E_z(\omega_1)E_z(\omega_2) \\ E_y(\omega_1)E_z(\omega_2) + E_z(\omega_1)E_y(\omega_2) \\ E_x(\omega_1)E_z(\omega_2) + E_z(\omega_1)E_x(\omega_2) \\ E_x(\omega_1)E_y(\omega_2) + E_y(\omega_1)E_x(\omega_2) \end{pmatrix} \tag{2.8}$$

where K is the degeneracy factor, which takes the value of 1 for SFG, DFG, and OPG, while it takes a value of 1/2 for degenerate cases such as optical rectification (ω_1=ω, ω_2= -ω) and SHG (ω_1=ω_2=ω). Hence for SHG, the equation can be expressed as

$$\begin{pmatrix} P_x(2\omega) \\ P_y(2\omega) \\ P_z(2\omega) \end{pmatrix} = \varepsilon_0 \begin{bmatrix} d_{11} & d_{12} & d_{13} & d_{14} & d_{15} & d_{16} \\ d_{21} & d_{22} & d_{23} & d_{24} & d_{25} & d_{26} \\ d_{31} & d_{32} & d_{33} & d_{34} & d_{35} & d_{36} \end{bmatrix} \begin{pmatrix} E_x^2(\omega) \\ E_y^2(\omega) \\ E_z^2(\omega) \\ 2E_y(\omega)E_z(\omega) \\ 2E_x(\omega)E_z(\omega) \\ 2E_x(\omega)E_y(\omega) \end{pmatrix} \tag{2.9}$$

The matrix components "d_{im}" are known as the nonlinear coefficients of the material.

Another important symmetry condition that can be viewed as the geometrical symmetry, arising from the structural or spatial symmetry of the material. This crystal structural symmetry can further reduce the number of independent nonlinear coefficients. One of the major consequences of this symmetry condition is that for materials possessing inversion symmetry in their crystal structure, all nonlinear

coefficients vanish altogether [53]. Such materials are known as *centrosymmetric* materials. Inversion symmetry means that if we change the sign of the applied electric field $E(t)$, then the sign of the induced polarization must also change. Hence, equation 2.3 becomes

$$-P^{NL}(t) = \varepsilon_0 \chi^{(2)}(-E(t))^2 \tag{2.10}$$

which implies

$$-P^{NL}(t) = \varepsilon_0 \chi^{(2)} E(t)^2 \tag{2.11}$$

By comparison of equation 2.10 with 2.11, we see that $P^{NL}(t)$ must be equal to $-P^{NL}(t)$, which is only possible if $P^{NL}(t)$ identically vanishes, resulting in

$$\chi^{(2)} = 0 \tag{2.12}$$

Therefore, all second-order nonlinear optical effects are excluded in centrosymmetric materials and are only possible in *non-centrosymmetric* materials. Thus, out of the 32 crystal classes that are classified according to their point group symmetry, as summarized in Table. 2.1 [54, 55], only 20 of the 21 accentric class exhibit quadratic susceptibility.

2.4 Coupled-wave equations for second order nonlinear processes

The previous sections have delt with the nonlinear response of a medium to an applied electromagnetic field. The nonlinear polarization thus induced results in the generation of new frequencies. The interaction between the involved fields can be expressed using Maxwell's equations,

$$\nabla \times E = -\mu_0 \frac{\partial H}{\partial t} \tag{2.13}$$

Optic Axis	**Crystal Class**	**Centro-Symmetric Point Groups**		**Non-Centro-Symmetric Point Groups**				
				Polar		**Non-Polar**		
Biaxial	Triclinic	$\bar{1}$		1		None		
	Monoclinic	2 or m		2	m	None		
	Orthorhombic	mmm		mm2		222		
Uniaxial	Tetragonal	4 or m	4 or mmm	4	4mm	$\bar{4}$	$\bar{4}$2m	422
	Trigonal	$\bar{3}$	$\bar{3}$m	3	3m	32		
	Hexagonal	6 or m	6 or mmm	6	6mm	$\bar{6}$	$\bar{6}$m2	622
Optically Isotropic	Cubic	m3	m3m	None		432	$\bar{3}$m	23
Total Number		11 Groups		10 Groups		11 Groups		

Table 2.1: Classification of crystal groups.

$$\nabla \times H = \frac{\partial D}{\partial t} \tag{2.14}$$

where the D is the electric displacement vector, defined as $D = \varepsilon_0 E + P$, and H is the magnetic field strength, related to the magnetic flux by $B = \mu_0 H$, μ_0 is the permeability of free space. Equations 2.13 and 2.14 are the Maxwell´s equations describing light propagation through a material which is non-magnetic and transparent ($J = 0$) at the frequencies of the propagating waves. Using these equations, the wave equation describing the electric field in the medium generated by the driving polarization can be expresses as,

$$\nabla^2 E - \frac{1}{c^2}\frac{\partial^2 E}{\partial t^2} = \frac{1}{\varepsilon_0 c^2}\frac{\partial^2 P}{\partial t^2} \tag{2.15}$$

Now, for the lossless medium, we assume that the electric field, E, and polarization, P, are described by the sum of three uniform plane waves propagating along $x-$axis according to

$$E_j(x,t) = E(x,\omega_j)e^{-i(k_j x - \omega_j t)} + c.c \tag{2.16}$$

$$P_j(x,t) = P(x,\omega_j)e^{-i(k_j x - \omega_j t)} + c.c \tag{2.17}$$

where $j = 1, 2, 3$ represent the three interacting fields, ω is the frequency, and k is the wave number given by

$$k = \frac{n(\omega)\omega}{c} \tag{2.18}$$

with refractive index $n(\omega)$ at frequency ω represented as

$$n(\omega) = \sqrt{\frac{\varepsilon(\omega)}{\varepsilon_0}} \tag{2.19}$$

and c is the speed of light in vacuum. In writing equations 2.16 and 2.17, we have used the complex function description of the optical field. Also, since the waves at the three different frequencies are exchanging energy through $\chi^{(2)}$processes as they propagate through the medium, the respective amplitudes will, in general, vary with position. Hence, the complex field amplitudes are expressed as a function of x. Further, we also assume that the amplitudes of the fields vary only slowly over a distance comparable to a wavelength, known as *slowly varying amplitude approximation* [45], which simplifies our wave equations from a second-order differential equations to first order differential equations.

$$\left|\frac{\partial^2 E_j}{\partial x^2}\right| \ll \left|k_j \frac{\partial E_j}{\partial x}\right| \tag{2.20}$$

Therefore, using equations. 2.3, 2.16, 2.17 and 2.20, we arrive at

$$\frac{\partial E_1}{\partial x} = \frac{i\omega_1^2 d_{eff}}{k_1 c^2} E_3 E_2^* e^{i\Delta k x} \tag{2.21}$$

$$\frac{\partial E_2}{\partial x} = \frac{i\omega_2^2 d_{eff}}{k_2 c^2} E_3 E_1^* e^{i\Delta k x} \tag{2.22}$$

$$\frac{\partial E_3}{\partial x} = \frac{i\omega_3^2 d_{eff}}{k_3 c^2} E_1 E_2 e^{-i\Delta k x} \tag{2.23}$$

where d_{eff} is the effective nonlinear coefficient, and $\Delta k = k_3 - k_2 - k_1$, where both additionally depend on the direction of propagation of the interacting waves in the nonlinear medium. These equations are commonly refered to as *coupled amplitude equations*. Physically, the three-wave mixing processes can be viewed as a distortion in the electric fields at frequencies ω_1, ω_2 and ω_3. These distortions lead to oscillating polarization at any combination of the frequencies, which in turn radiates optical waves at the corresponding frequencies.

2.5 Phase-matching

In writing the *coupled amplitude equations*, we defined the wave vector mismatch, $\Delta k = k_3 - k_2 - k_1$. Efficient realization of any nonlinear optical effect requires that $\Delta k = 0$. Only those interactions for which $\Delta k = 0$ will undergo macroscopic amplification as they propagate through the medium. This condition, which is know as "phase-matching" will be discussed in this section. Physically, the quantity Δk represents the mismatch in phase between the optical fields as they propagate through the nonlinear medium. In general, because of the dispersion in the medium, the optical waves at different frequencies propagate with different phase velocities, so that $\Delta k \neq 0$. Under this condition, the interacting fields periodically step out of phase and interfere constructively an destructively as they travel through the nonlinear medium. Therefore, they exchange energy back and forth, with the net result that the intensities of the generated fields undergo oscillations along the propagation direction, as shown in Fig. 2.2. In the figure, L_c is the coherence length, defined as the distance in the nonlinear crystal over which the interacting fields are in phase,

$$L_c = \frac{2\pi}{\Delta k} \tag{2.24}$$

This is the maximum useful crystal length in the presence of phase-mismatch. Phase-matching is vital to any nonlinear interaction, but we will discuss it here in the context of SHG. A similar concept holds for any other nonlinear optical process. There are two important techniques to achieve phase-matching, *birefringent phase-matching* (BPM) and *quasi-phase-matching* (QPM).

2.5.1 Birefringent phase-matching

The practical technique for satisfying the phase-matching condition, $\Delta k = 0$, was first suggested, independently by Giordmaine [11] and Maker et al., [12]. The problem of phase-mismatch arises due to the fact that the fundamental and the generated

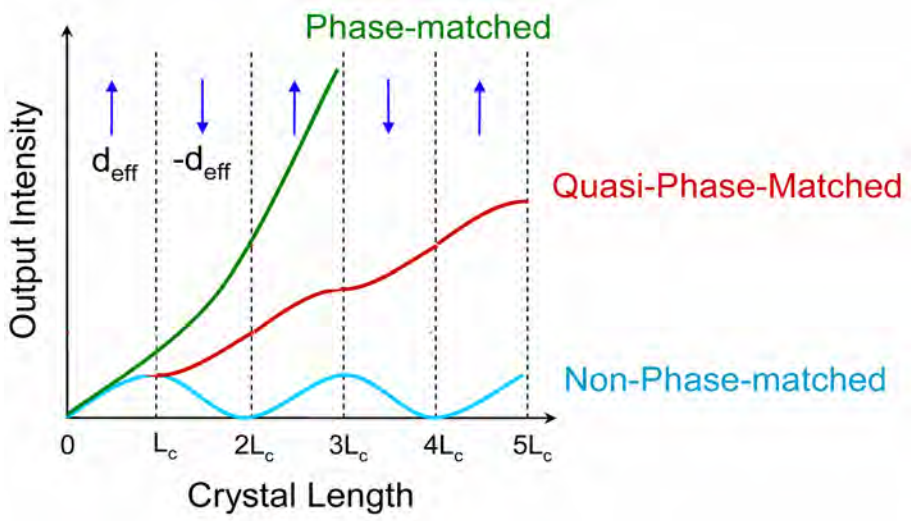

Figure 2.2: Illustration of perfectly birefringent phase-matched ($\Delta k = 0$), quasi-phase-matched, and non-phase-matched ($\Delta k \neq 0$) conditions in a second-order nonlinear optical process.

second harmonic travel with different phase velocities inside the nonlinear crystal due to the different refractive indices they experience. There are two factors that can cause the waves to experience different refractive indices. Firstly, they are of different wavelengths. In case of SHG, the generated wavelength is half that of the fundamental wavelength. So, dispersion will cause the two waves to experience different refractive indices. Secondly, it is the property of certain optical materials to have two different refractive indices depending on the polarization, known as birefringence, which can also cause the waves to experience different refractive indices. Now these two factors can be made to exactly balance each other, making the index difference due to dispersion to be exactly opposite to the index difference due to birefringence. This technique is known as *birefringent phase-matching* (BPM). The result is that both the fundamental and the second harmonic waves experience the same refractive index and the SHG output grows as in the case of perfect birefringent phase-matching as shown in Fig. 2.2.

With regard to optical properties, birefringent crystals may be classified into two distinct categories. Optically uniaxial crystals, in which $n_x = n_y \neq n_z$ and optically

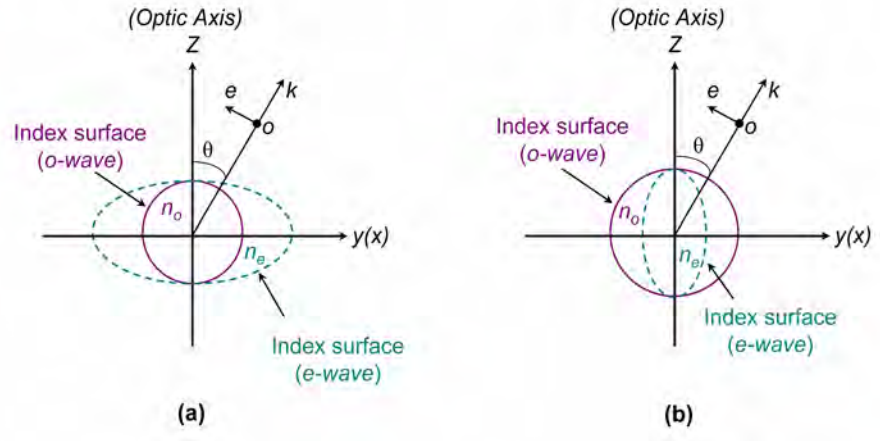

Figure 2.3: Refractive index surfaces for (a) positive and (b) negative uniaxial crystals.

biaxial crystals in which $n_x \neq n_y \neq n_z$. A discussion of uniaxial crystals is presented here. In a uniaxial crystal, out of the two orthogonal polarizations, one experiences the same refractive index regardless of the direction of propagation in the medium. This is known as the *ordinary polarization* (o-polarization). If we define θ as the angle between the normal direction and the optic axis (z-axis), the the refractive index of the o-polarized wave is given by $n_o(\theta) = n_o$. The wave with orthogonal polarization to o-polarized wave however, experiences a refractive index that varies with the propagation angle. This is refered to as *extraordinary polarization* (e-polarization). The index of refraction, $n_e(\theta)$, of the e-polarized wave at an angle θ to the optic axis is given by [50]

$$\frac{1}{n_e^2(\theta)} = \frac{cos^2(\theta)}{n_o^2} + \frac{sin^2(\theta)}{n_e^2} \tag{2.25}$$

where n_o and n_e are the principal refractive indices of the uniaxial crystal.

BPM can be realized in two types: Type-I, where the driving fields have the same polarization and the generated field is orthogonally polarized compared to the driving field, and Type-II, where the driving fields are orthogonally polarized. Further, uniaxial crystals are classified to two types, positive uniaxial crystals for

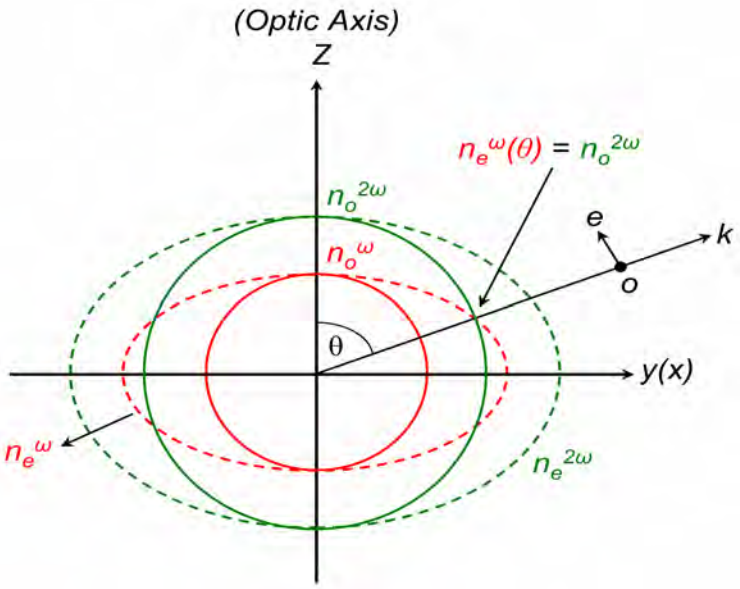

Figure 2.4: Illustration of perfect (Type-I) phase-matching in case of extraordinary fundamental wave to generate ordinary second harmonic wave.

which $n_e > n_o$, and negative uniaxial crystals for which $n_o > n_e$. The normal index surfaces of a positive and negative uniaxial crystals are illustrated in Fig. 2.3. In either cases, it is often possible to find a phase-matching direction along which suitably polarized waves satisfy energy conservation as well as momentum conservation conditions. Figure. 2.4 shows the propagation direction at an angle θ of a positive uniaxial crystal, where the extraordinary index for the fundamental wave of frequency ω is equal to the ordinary index for second harmonic wave of frequency 2ω, thus birefringence compensating the dispersion and resulting in perfect Type-I phase-matching.

In a birefringent anisotropic medium, the direction of the wave-normal is generally different from the direction of energy flow or ray direction. This phenomenon is known as double-refraction, spatial walk-off, or Poynting vector walk-off. The walk-off reduces the spatial overlap between the interacting ordinary and extraordinary polarized waves in the nonlinear crystal, thus limiting the interaction length of the nonlinear material. An effective crystal length in the presence of walk-off is defined

as

$$l_a = \frac{\pi^{\frac{1}{2}} w_0}{\rho} \tag{2.26}$$

where w_0 is the waist radius of the input beam, ρ is the spatial walk-off angle, l_a is also known as the aperture length and is linearly proportional to the beam waist radius, so that for long interaction lengths large spot sizes should be used. But, unfortunately, nonlinear optical processes require high intensity, and hence small beam radii. Therefore, a good balance between the crystal length and beam radii must be maintained to achieve practical efficiencies. The spatial walk-off angle in case of a uniaxial crystal is expressed as

$$tan(\rho) = -\frac{1}{2} |n_e(\theta)|^2 \left(\frac{1}{n_e^2} - \frac{1}{n_o^2} \right) sin(2\theta) \tag{2.27}$$

The deleterious effect of double refraction and spatial walk-off can, however, be overcome if the nonlinear interaction occurs at an angle $\theta = 90^{\text{o}}$ relative to principal axes of the nonlinear crystal. This is referred to as *noncritical phase-matching* (NCPM). If $\theta \neq 90^{\text{o}}$, it is called *critical phase-matching* (CPM). In NCPM configuration, the spatial walk-off vanishes and the nonlinear crystal length becomes the effective interaction length of the nonlinear optical process.

2.5.2 Quasi-phase-matching

An alternative technique to achieve BPM is *quasi-phase-matching* (QPM), first suggested by Armstrong et al. [60]. QPM involves repeated inversion of relative phase by changing the sign of the nonlinear coefficient of the material, as shown Fig. 2.5. QPM is the most widely used phase-matching configuration. A common means for implementing the QPM requires sign reversal of nonlinear coefficient through periodic poling of a ferroelectric medium such as lithium niobate [28, 56]. A schematic of the sign reversal is shown in Fig. 2.5. In case of SHG, by reversing the sign of the nonlinear polarization every L_c, we minimize the destructive interference among

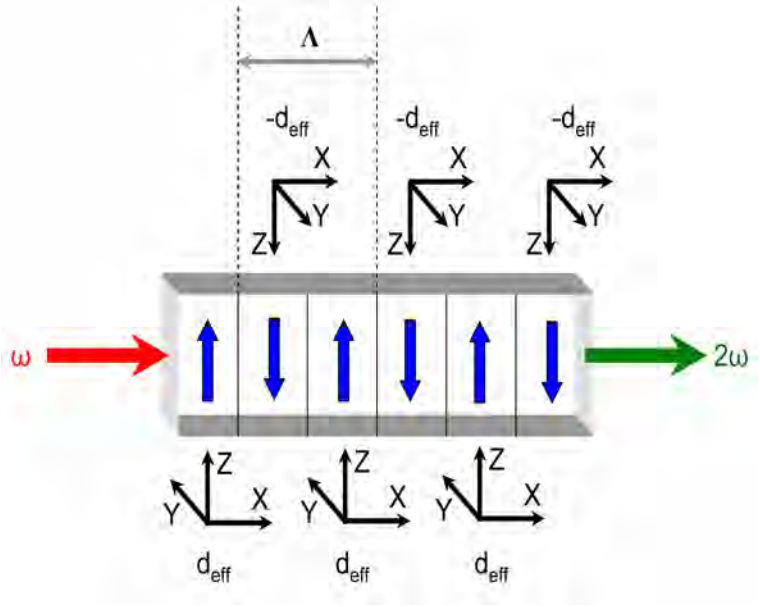

Figure 2.5: Periodic inversion of the sign of the nonlinear coefficient by periodic poling in a QPM nonlinear material.

second-harmonic wave components generated at different positions along the propagation direction, and hence keep power flowing from the fundamental to the second harmonic.

Since we can not actually achieved true phase-velocity-matching between the fundamental and second-harmonic wave, this technique is termed "*quasi-phase-matching*". As evident from Fig. 2.2, the build-up of output intensity is less rapid than that in case of perfect phase-matching. Since in QPM, the nonlinear coefficient of the material is modulated with the period $\Lambda = 2L_c$, for optimum duty factor of 50%, the effective nonlinearity is represented as

$$d_{eff} = \frac{2}{\pi m} d_{ij} \tag{2.28}$$

where m is the order of grating period. Hence, for a first order grating the effective nonlinearity is reduced by $2/\pi$.

Although in principle, QPM results in the reduction of the nonlinear coefficient for the frequency conversion processes, in practice this is compensated by the possibility

of having all the intracavity waves polarized in the same direction. This provides access to the largest nonlinear tensor element of the material, which often is an element with both the indices equal, $d_{ij}, (i = j)$. For example, d_{33} is the largest tensor element for lithium niobate ($LiNbO_3$), lithium tantalate ($LiTaO_3$), and potassium titanyl phosphate ($KTiOPO_4$). In addition to accessing the highest nonlinear coefficients, the greatest advantage of QPM is that it can be employed when BPM is impossible in materials with low birefringence, and can provide NCPM for any nonlinear interaction permitted with in the transparency range of the material. Further, the possibility of using NCPM configuration avoids the poynting vector walk-off between the interacting fields, since all the fields can be polarized parallel to one of the principal optical axes of the nonlinear crystal. Additionally the well-established periodical poling technology allows the fabrication of multiple grating crystals, which extends the phase-matching achievability over the entire transparency range of the nonlinear material. In devices such as OPO, this means that the device can be tuned over a wide spectral range with a fixed pump wavelength.

2.6 Second harmonic generation

Second harmonic generation (SHG) is a process in which two photons, at a frequency ω_1=ω_2=ω, interact to generate output at a frequency, 2ω. There are various parameters that are important for efficient SHG. These include choice of a crystal with high nonlinear optical coefficient, optimum length of the nonlinear crystal, spectral and temperature acceptance bandwidth. Although QPM allows the use of long crystals, enabling the possibility of utilizing increased interaction length and thereby achieving high efficiency, the optimum choice of the nonlinear crystal length should ensure wide spectral and temperature acceptance bandwidths, which help in the efficient conversion of the fundamental to SHG [56]. The spectral acceptance bandwidth is

given by

$$\Delta\lambda = \frac{0.4429\lambda_\omega}{L}\left|\frac{n_{2\omega}-n_\omega}{\lambda_\omega}+\frac{\partial n_\omega}{\partial\lambda_\omega}-\frac{1}{2}\frac{\partial n_{2\omega}}{\partial\lambda_\omega}\right|^{-1} \tag{2.29}$$

where L is the length of the nonlinear crystal, n_ω and $n_{2\omega}$ are the refractive indices at the fundamental (λ_ω) and second harmonic wavelengths, respectively. The temperature acceptance bandwidth is given by

$$\Delta T = \frac{0.4429\lambda_\omega}{L}\left|\frac{\partial n_{2\omega}}{\partial T}-\frac{\partial n_\omega}{\partial T}-\alpha(n_{2\omega}-n_{1\omega})\right|^{-1} \tag{2.30}$$

where α is the linear thermal expansion coefficient of the crystal.

For example, the acceptance bandwidths for a 30-mm-long MgO-doped stoichiometric periodically poled lithium tantalate (MgO:sPPLT) crystal are shown in Fig. 2.6. Using the Sellmeier equations of [57], the spectral and temperature acceptance bandwidths are calculated to be $\Delta\lambda$=0.082 nm and ΔT=0.96 °C, respectively [41].

The generated second harmonic power is a quantity of more practical importance, and SHG conversion efficiency in plane-wave approximation, with no depletion of the fundamental wave, is given by [58]

$$\eta = \frac{P_{2\omega}(L)}{P_\omega(0)} = \eta_{norm}\left[\frac{P_\omega L^2}{A}\right] sinc^2(\frac{\Delta kL}{2}) \tag{2.31}$$

$$\eta_{norm} = \frac{8\pi^2 d_{eff}^2}{n_\omega^2 n_{2\omega} c\varepsilon_0 \lambda_\omega^2}$$

In case of focused Gaussian beams, this expression needs to be modified, and the SHG efficiency is given by [58]

$$\eta = \frac{16\pi^2 d_{eff}^2 h}{n_\omega n_{2\omega} c\varepsilon_0 \lambda_\omega^3} LP_\omega \tag{2.32}$$

$$\triangle k = k_{2\omega} - k_\omega - \frac{2\pi}{\Lambda} \tag{2.33}$$

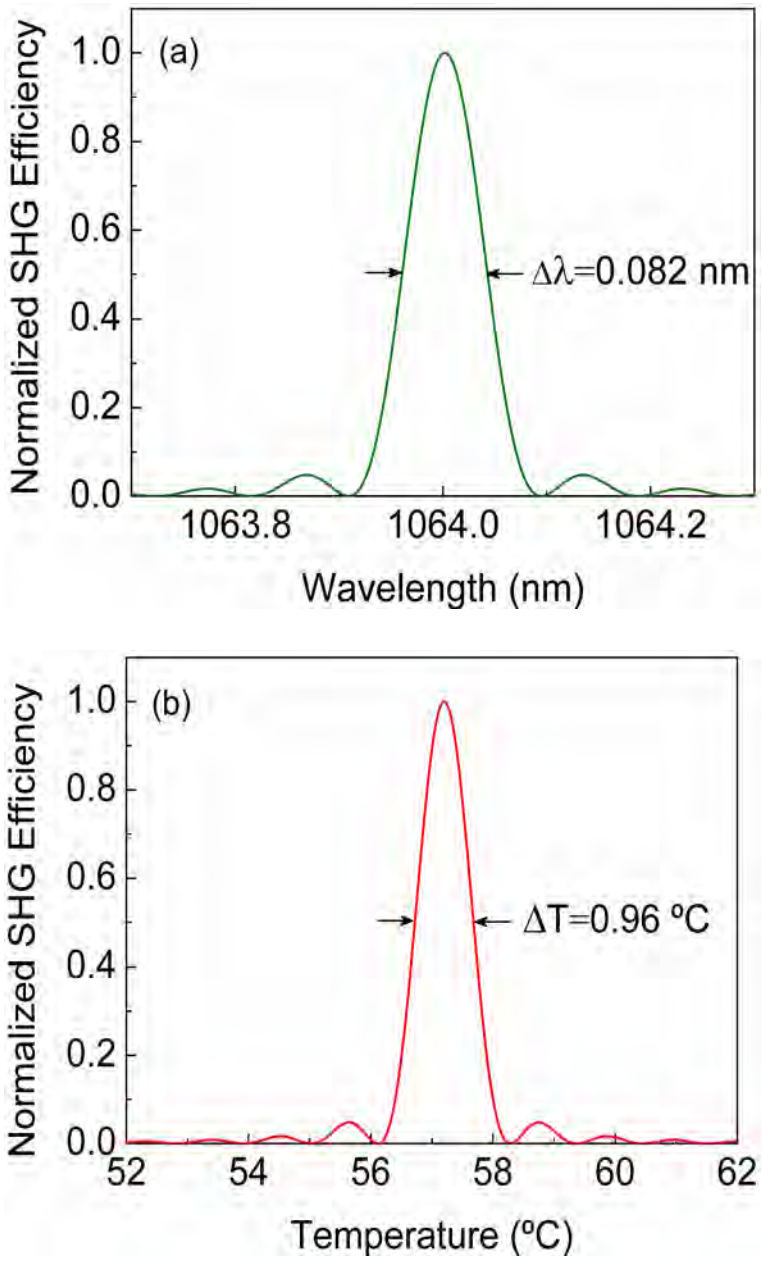

Figure 2.6: (a) Spectral and (b) temperature acceptance bandwidths of 30 mm long MgO:sPPLT nonlinear crystal.

where η_{norm} is the normalized SHG conversion efficiency, $P_{2\omega}$ is the SHG power, P_{ω} is the fundamental power, d_{eff} is the effective nonlinear coefficient, h is the Boyd and Kleinman focusing parameter [59], n_{ω} and $n_{2\omega}$ are the refractive indices at the fundamental and SHG wavelengths, respectively, c is the velocity of light, ε_0 is the permittivity of free space, λ_{ω} is the fundamental wavelength, L is the length of the nonlinear crystal, Δk is the QPM wave-vector mismatch, and Λ is the QPM grating period.

The SHG of a monochromatic plane wave can be understood by solving the coupled amplitude equations 2.21, 2.22 and 2.23. Armstrong et al. [19] have derived and solved these equations for SHG. The exact solution of the coupled-wave equations with zero input at the SH wavelength is given by [19]

$$\eta = V_b^2 sn^2\left(\frac{\Gamma L}{V_b} \mid V_b^4\right) \tag{2.34}$$

$$V_b = \left[\frac{\Delta S}{4} + \sqrt{1 + \left(\frac{\Delta S}{4}\right)^2}\right]^{-1}$$

$$\Delta S = \frac{\Delta k}{\Gamma}$$

$$\Gamma = \sqrt{\eta_{norm} I_{\omega}}$$

where sn is a Jacobi elliptic function [63, 61]. In the limit of no fundamental wave depletion, equation 2.34 simplifies to 2.35, while in case of perfect phase-matching with fundamental wave depletion, equation 2.34 becomes [19, 62]

$$\eta = tanh^2(\Gamma L) \tag{2.35}$$

All above expressions have been derived by assuming no SHG signal at the input

to the nonlinear crystal. However, in the experiments described in this work, where multiple nonlinear crystals are deployed to enhance the SHG efficiency in single-pass configuration, the nonlinear crystals after the first have non-zero input at the second harmonic wavelength. The SHG efficiency in such a case, with optimum relative phase of $\phi_{2\omega} - \phi_{\omega} = \pm\frac{\pi}{2}$ between the fundamental and SHG wave at the input, and under perfect phase-matching, becomes [19]

$$\eta = tanh^2(\Gamma(l_0 + L)) \tag{2.36}$$

The effect of non-zero input at the second harmonic wavelength can thus be considered as an increase in the length of the nonlinear crystal by a value, l_0. Hence, for example, two individual 30-mm-long crystals can be considered as a single crystal of 60-mm length. This is used in chapter. 9 of this thesis. Fig. 2.7 shows the SHG efficiency as a function of incident fundamental power for MgO:sPPLT nonlinear crystals of length 30 mm, 60 mm and 90 mm, as calculated from equation 2.36. It is to be noted that thermal dephasing effects and back-conversion are not considered in this calculation. The estimated fundamental power required to achieve a SHG efficiency of 55% in single-pass configuration is 17.8 W and 12 W in MgO:sPPLT crystals of length 60 mm and 90 mm, respectively, while a fundamental power greater than 30 W is needed to achieve a similar SHG efficiency using a 30 mm-long crystal.

2.7 Optical parametric oscillator

An optical parametric oscillator (OPO) essentially consists of an optical oscillator and a nonlinear crystal. It is a device based on $\chi^{(2)}$ nonlinear mixing process in a dielectric crystal involving three optical fields, input pump (ω_p), generated signal (ω_s) and idler (ω_i), with the frequencies satisfying energy conservation [46, 47, 48],

$$\omega_p = \omega_s + \omega_i \tag{2.37}$$

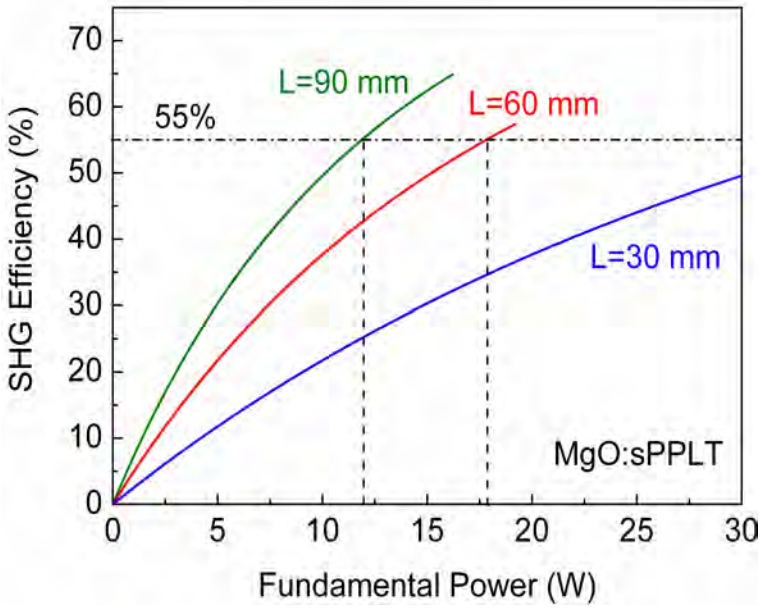

Figure 2.7: Theoretically calculated SHG efficiency for different lengths of the MgO:sPPLT nonlinear crystal as a function of fundamental power.

As long as the sum is conserved, ω_s or ω_i can each have basically any value from zero to ω_p. The specific pair of frequencies resulting from each ω_p is ultimately determined by the phase-matching condition,

$$k_p = k_s + k_i \tag{2.38}$$

where $k_j = (n_j\omega_j/c), (j = p, s, i)$ are the wave vectors of the pump, signal and idler fields. In perfect phase-matching condition, where $\Delta k = k_p - k_s - k_i = 0$, then equations 2.37 and 2.38 can be written as

$$\omega_i = \frac{n_p - n_s}{n_i - n_s}\omega_p \tag{2.39}$$

Here n_p, n_s, n_i are the refractive indices of the pump, signal and idler, respectively. Equation 2.39 shows that changing the refractive indices at pump, signal and idler wavelengths will enable idler wavelength to be varied for a fixed pump, thereby providing a means to tune the OPO [2, 48].

In practice, the process of optical parametric oscillation is initiated by a single intense, high-frequency pump field at the input to a nonlinear crystal. The corresponding nonlinear process is spontaneous optical parametric generation through which the intense pump field produces the low-frequency, signal and idler fields. In the next step, the pump field mixes with the signal field to give rise to idler field and, similarly, the idler field mixes with the pump field to produce more signal field. This corresponds to amplification of the signal and idler fields through optical parametric amplification process. Given the amplification process, an OPO essentially requires an optical oscillator to provide feedback, as in a laser. An OPO is similar to laser, but the main difference between the two is that the optical gain in OPOs is a result of parametric amplification in a nonlinear crystal, unlike stimulated emission in lasers. The optical gain in an OPO is instantaneous, meaning that the gain is only available in the presence of pump.

2.7.1 Gain and amplification in parametric interactions

When the parametric process is phase-matched, signal and idler fields are generated from parametric noise, and are subsequently amplified during their propagation through the nonlinear material, the single-pass parametric gain in the nonlinear crystal is represented as [48]

$$G_s(L) = \frac{I_s(L)}{I_s(0)} - 1 = \Gamma^2 L^2 \frac{sinh^2(\sqrt{\Gamma^2 - (\frac{\Delta kL}{2})^2})}{(\Gamma^2 L^2 - (\frac{\Delta kL}{2})^2)} \tag{2.40}$$

where L is the interaction length, I is the signal field intensity, Δk is the phase-mismatch, and Γ is the gain factor defined as

$$\Gamma_s = \frac{8\pi^2 d_{eff}^2}{c\varepsilon_0 n_p n_s n_i \lambda_s \lambda_i} I_p(0) \tag{2.41}$$

Here, λ_s and λ_i are the signal and the idler wavelengths. Under perfect phase-matching condition, when $\Delta k = 0$, equation 2.40 reduces to

$$G_s(L) = sinh^2(\Gamma L) \tag{2.42}$$

which, for low gains ($\Gamma L \leq 1$), approximates to

$$G_s(L) = \Gamma^2 L^2 \tag{2.43}$$

and for high gains ($\Gamma L >> 1$), reduces to

$$G_s(L) = \frac{1}{4} e^{2\Gamma L} \tag{2.44}$$

Therefore, under phase-matched condition, the single-pass gain has a quadratic dependence on ΓL in the low-gain limit, whereas it increases exponentially with $2\Gamma L$ in the high-gain limit.

2.7.2 Oscillator configurations

Efficient operation of an OPO necessitates the attainment of sufficient gain at the parametric waves for a given pump power to overcome the losses in the cavity. This can be achieved by providing feedback at the generated waves using various configurations of the optical cavity. The losses in the OPO cavity originate from the scattering, parasitic reflection and absorption in the crystal. More important are the losses due to the finite reflection of the cavity mirrors. Unlike in the case of a conventional laser, OPO involves three-wave interaction. Hence, any or all of the three waves can be resonated in the cavity, while partially extracting the desired wave. Depending on the number of waves resonated in the optical cavity, there are four major configuration, which are illustrated in Fig. 2.8. If we consider the incident pump wave to be at a frequency ω_3, then a *singly resonant oscillator* (SRO)

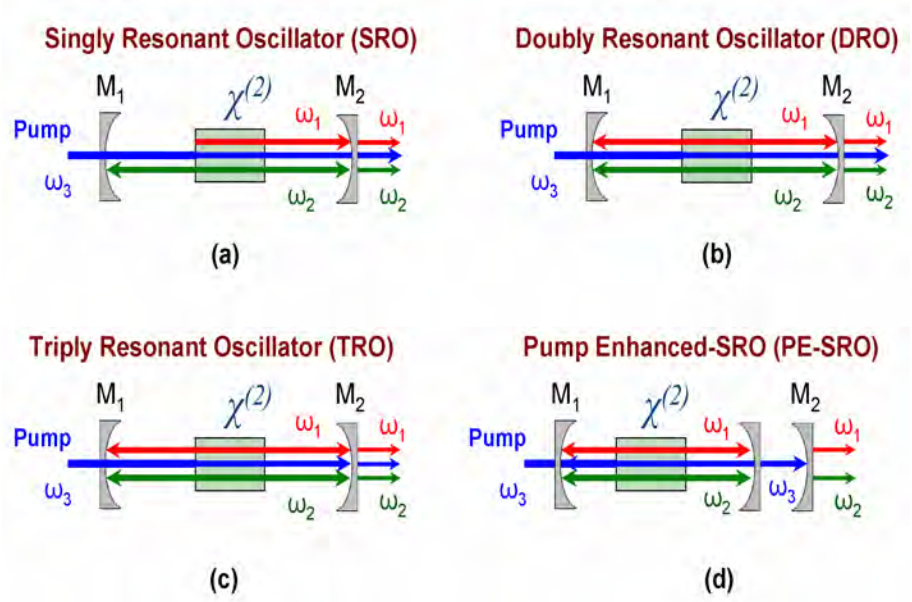

Figure 2.8: Various OPO resonance configurations: (a) singly resonant oscillator (SRO), (b) doubly resonant oscillator (DRO), (c) triply resonant oscillator (TRO), (d) pump enhanced-SRO (PE-SRO).

is a configuration in which one of the generated waves, either the signal (ω_2) or the idler (ω_1) is resonated while the other generated wave is completely extracted from the cavity along with the leftover or undepleted pump, as shown in Fig. 2.8(a). With sufficiently high pump power, it is also possible to extract significant amount of power from the resonant wave in an SRO. In a *doubly resonant oscillator* (DRO) configuration, both signal (ω_2) and idler (ω_1) waves are resonated inside the cavity, with one or both of the resonant waves partially extracted out of the cavity along with the undepleted pump, as depicted in Fig. 2.8(b). A *triply resonant oscillator* (TRO) is resonant at all the three interacting waves, pump (ω_3), signal (ω_2) and the idler (ω_1) is shown in Fig. 2.8(c). Another configuration, which is used to enhance the pump in the cavity, is known as *pump enhanced-SRO* (PE-SRO), in which the pump as well as one of the generated waves is resonated in the cavity, as shown in Fig. 2.8(d).

The advantage of DRO and TRO is that the threshold pump power can be as low as

few milliWatts. This is particularly interesting for continuous-wave (cw) operation, where the threshold pump power could be of the order of few Watts, due to low parametric gain. However, stable operation in case of DRO and TRO is challenging, because they require the simultaneous fulfillment of cavity resonant condition for two or three different wavelengths. On the other hand, in spite of the high operation threshold of SROs, they provide single-frequency output with stable performance. The work presented in this thesis is focused on the SRO configuration.

2.7.3 Steady-state SRO threshold

In the SRO configuration, only one of the generated waves is resonant in the nonlinear medium. Let the resonant wave be the signal wave. Further, the idler wave leaves the nonlinear medium after a single pass. Because the pump is propagating only in the forward direction through the medium, parametric gain occurs for propagation of the signal in this direction only. The fractional round-trip power loss in a SRO for the signal wave, α_s, expressed in terms of the pump intensity required to reach oscillation threshold I_{th}, is given by [48]

$$\frac{8\pi^2 d_{eff}^2 I_{th}}{c\varepsilon_0 n_p n_s n_i \lambda_s \lambda_i} = \alpha_s \tag{2.45}$$

A more useful form of the SRO threshold in terms of pump power is given by [64],

$$P_{th} = \frac{\alpha_s}{T_p} \frac{\varepsilon_0 c n_s n \lambda_p \lambda_s \lambda_i}{64\pi^2 d_{eff}^2} \frac{1+K}{L h_{sm}} \tag{2.46}$$

where Tp is the transmission of the pump through the input mirror and crystal surface, and $K = k_p/k_s$, h_{sm} is the focusing factor. Hence, the threshold pump power of an SRO is crucially dependent on the losses, requiring very high reflection coatings, typically R>99.9%, for the resonant wave, and high transmission T>95% for the pump and idler waves.

2.7.4 Material requirements

The quest for optimum nonlinear materials for different parametric processes, including OPOs has resulted in the development of numerous nonlinear crystals. But, there are several important parameters that have to be taken into consideration when selecting the nonlinear crystal for an OPO. The material of choice should have

- Non-centrosymmetry
- Optical anisotropy
- Wide transparency range at the operating wavelength
- Sufficient birefringence
- Large variation of refractive indices with temperature, angle, pressure or electric field.
- Large nonlinearity
- Low spatial walk-off
- Phase matchability, preferably NCPM
- High damage threshold
- Good mechanical, chemical and thermal properties
- Availability of large crystals in high optical quality with low transmission losses

However, the simultaneous requirement for majority of the above characteristics has restricted the number of potentially useful crystals to a few. Another important parameter determining the large nonlinearity is the nonlinear figure-of-merit defined as

$$FOM = \frac{d_{eff}}{\sqrt{n_p n_s n_i}} \tag{2.47}$$

which is an important parameter to a assess the nonlinearity of the material. The FOM is directly proportional to the d_{eff} and inversely proportional to the square root of the refractive indices of the pump, signal and idler, which are all the inherent properties of the nonlinear crystal. Hence, the larger the FOM, the better. It is also desirable to have large phase-matching bandwidth, defined by $\left|-\frac{\pi}{2} < \frac{\Delta kL}{2} < \frac{\pi}{2}\right|$, to efficiently transfer energy between the interacting waves. Once the nonlinear material is chosen, its dispersion properties govern various parameters such as spectral, angular and temperature acceptance bandwidths. The pump spectral acceptance bandwidth for an OPO, with a nonlinear crystal of length L, is given by [48, 25]

$$\Delta\lambda_p L = \lambda_p^2 \left[(n_p - n_i) + \lambda_i \left(\frac{\partial n_i}{\partial \lambda_i}\right) - \lambda_p \left(\frac{\partial n_p}{\partial \lambda_p}\right)\right]^{-1} \tag{2.48}$$

This indicates that for a given crystal length, a maximum pump bandwidth of $\Delta\lambda_p$ is efficiently converted into signal and idler. The corresponding generated signal bandwidth will be

$$\Delta\lambda_s L = \lambda_s^2 \left[(n_i - n_s) + \lambda_s \left(\frac{\partial n_s}{\partial \lambda_s}\right) - \lambda_i \left(\frac{\partial n_i}{\partial \lambda_i}\right)\right]^{-1} \tag{2.49}$$

Additionally, the signal bandwidth will be effected by pump bandwidth and pump beam divergence. Similarly, angular and temperature acceptance bandwidth can be defined, depending on the dispersion of the nonlinear material.

Dispersion properties of nonlinear crystals

Group velocity mismatch

Dispersion characteristics of optical crystal are of key importance in the context of ultrafast parametric processes. In frequency conversion processes, such as SHG, SFG, DFG, OPA or OPO, two or more waves interact with each other while propagating through the nonlinear medium. Due to dispersion of the material, different waves propagate at different group velocities. In case of interaction on the femtosecond

scale, the interacting pulses may get separated after propagating some distance in the medium, which means that there is a reduced effective interaction length. In order to evaluate this effect, an important temporal parameter is the group velocity mismatch (GVM) between the pump, signal, and idler. This can affect the temporal overlap between the pulses, thereby in influencing the parametric gain and temporal characteristics of the output pulses. The effects of temporal walk off can be estimated by evaluating the differences in the inverse group velocity between the pump, signal, and idler pulses. The group velocity of the laser pulses propagating in a nonlinear optical medium is defined as [50]

$$v_g = \frac{c}{n - \lambda\left(\frac{\partial n}{\partial \lambda}\right)} \tag{2.50}$$

where c is the velocity of light in vacuum, n is the refractive index of the nonlinear medium, λ is the center wavelength of the laser pulses. Then, GVM is defined as

$$\Delta v_g^{-1} = \left(\frac{1}{v_{g,i}} - \frac{1}{v_{g,j}}\right) \tag{2.51}$$

where $v_{g,i}$ and $v_{g,j}$ are the group velocities of the two interacting waves i and j. The effective interaction length L_{eff} for wave i and wave j can thus be calculated by the formula,

$$L_{eff} = \frac{\tau_p}{\left|\Delta v_g^{-1}\right|} \tag{2.52}$$

where τ_p is the incident pump pulse duration and it is assumed that i and j waves have similar pulse duration [51].

Group velocity dispersion

Group velocity dispersion (GVD) is another important temporal effect. Based on GVD, we can estimate degree of pulse broadening effects and design the compensation configuration, so that we can achieve ultrashort-pulsed operation. The GVD

can be calculated by evaluating the dispersion parameter, which is defined as

$$\beta'' = \frac{\partial^2 k}{\partial \omega^2} = \frac{\lambda^3}{2\pi c^2}\frac{\partial^2 n}{\partial \lambda^2} \tag{2.53}$$

The most important feature of the GVD values is the signal value, as this is the parameter governing whether or not the resonant wave will see a positive or negative GVD. The large positive GVD values encountered by the signal wave would imply that the signal pulses should be significantly chirped, with dispersion broadening generally becoming more prominent with shorter pump pulse durations and longer interaction lengths.

2.7.5 Wavelength tuning

One of the main advantages of OPOs compared to other laser systems is their wide wavelength tunability. An OPO can be tuned coarsely or continuously, depending on the requirements. Coarse tuning range is the total tuning range of the OPO, while continuous tuning range is the wavelength range in which the OPO can be tuned without mode hops. Many spectroscopic applications require continuous mode-hop-free tuning. The various wavelengths tuning methods in an OPO include,

- Angle tuning
- Grating tuning
- Temperature tuning
- Tuning by intracavity elements such as etalon
- Pump tuning
- Cavity length tuning

As discussed previously from equation 2.39, any parameter which can change the phase-matching, in particular the refractive index of the nonlinear crystal, can be

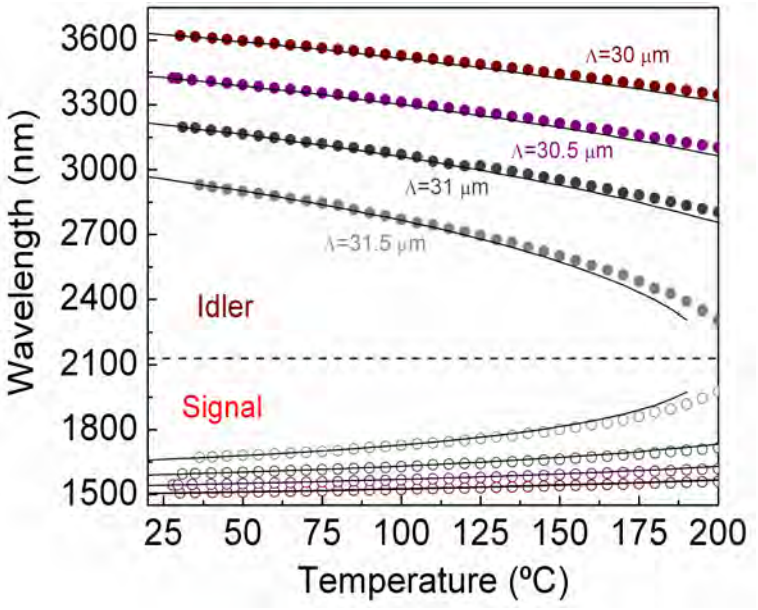

Figure 2.9: Tuning curves of a $1\mu m$ pumped MgO:PPLN OPO.

used to tune the OPO. In BPM nonlinear crystals, tuning is achieved by changing the angle of the nonlinear crystal, resulting in the change in the angle between the direction of propagation and optic axis. By doing so, the refractive index is influenced, and hence the phase-matching condition leads to tuning of the OPO. In QPM nonlinear crystals such as MgO:PPLN, coarse tuning is achieved by changing the grating period. A more common method of tuning in both BPM and QPM materials is temperature tuning in which the nonlinear crystal is mounted in an oven and its temperature is changed, thereby varying the refractive index and phase-matching condition. Continuous mode hop-free tuning is achieved by using an intracavity element such as etalon, or by continuously tuning the wavelength of the pump laser. Although cavity length tuning can be implemented to continuously tune an OPO by synchronously changing the cavity length of an SRO and angle tuning the etalon, it involves intricate design [66]. However, cavity length tuning is generally used in ultrafast OPOs. The work presented in this thesis uses grating tuning and temperature tuning. A typical tuning curves of a 1 μm pumped MgO:PPLN OPO using grating and temperature tuning techniques is shown in Fig. 2.9. The solid lines are

theoretically calculated from the relevent Sellmeier equations [65].

2.8 Cavity design

The successful operation of an OPO necessitates an optimum cavity design along with the perfect choice of nonlinear crystal and a pump source. The typical cavity configurations used in OPOs are shown in Fig. 2.10. The linear cavity is the simplest of all. The linear cavity, V-cavity and X-cavity are standing wave cavities, while the ring cavity is a travelling wave cavity. Hence, a unidirectional ring cavity is preferred in cw-SRO configuration to achieve stable single-frequency operation. On the other hand, V-cavity and X-cavity are commonly used in ultrafast OPOs. The ring cavity is the most difficult configuration among the designs shown in Fig. 2.10.

The relative advantages of the standing wave and travelling wave cavities are as follows:

In the context of ultrafast OPOs, it is easier to move the intracavity prisms used for dispersion compensation, in and out of the cavity without the need for realignment. Furthermore, with the standing wave cavity configurations, it is possible to couple back the residual pump beam for a second pass to provide additional pumping. The disadvantage is that for single pass pumping, the signal pulse sees gain only in one direction, but has Fresnel loss and experiences additional GVD while traversing the crystal in the unpumped direction. With the ring cavity for the OPO, no pump radiation is reflected back in to the laser, avoiding the need for an optical isolator and the signal pulse experiences gain each time it passes through the nonlinear crystal. Moreover, ultrafast OPOs are synchronously pumped. This means that the cavity length of the OPO has to be precisely synchronized with the pump laser laser cavity length, so that the signal pulses experience gain due to the presence of the pump pulse in each round-trip. Hence, the physical length of a standing wave cavity is half that of the round-trip cavity length and the physical length of a travelling wave ring cavity is equal to the round-trip cavity length. For example, for an 80 MHz

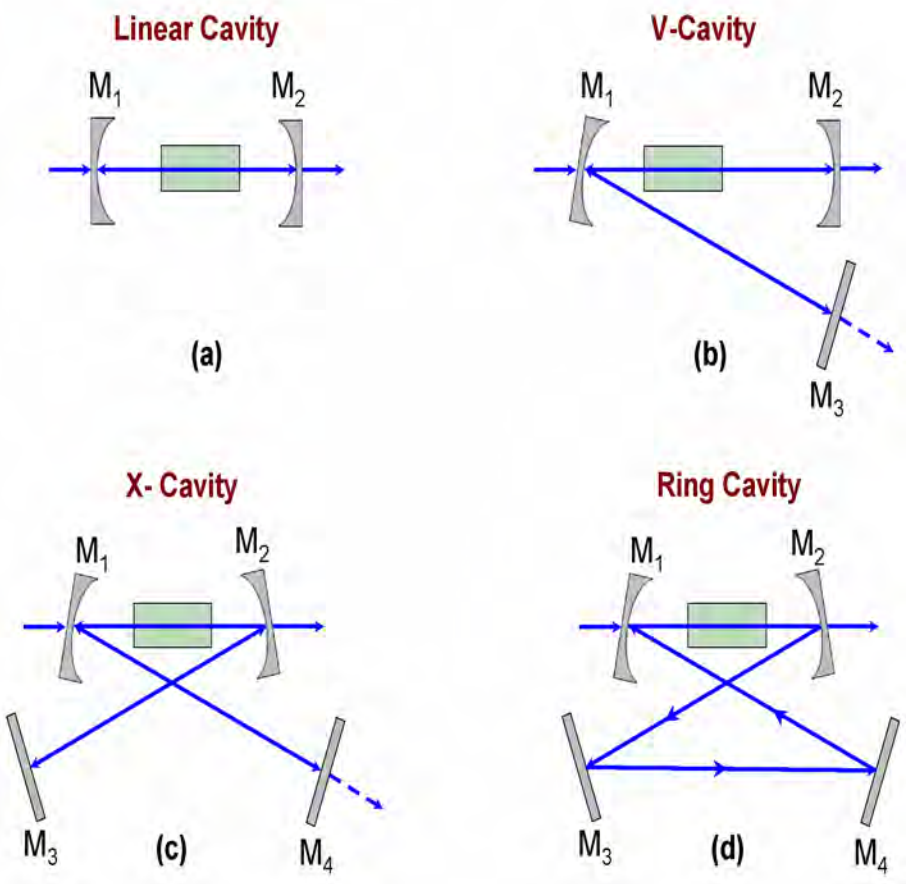

Figure 2.10: Various cavity designs: (a) Linear cavity, (b) V-cavity, (c) X-cavity, (d) Ring cavity.

repetition rate ultrafast OPO, the standing wave cavity length is given by

$$\frac{c}{(2 \times 80 \times 10^6)} = 1.875\, m$$

while, the travelling wave cavity length is given by,

$$\frac{c}{(80 \times 10^6)} = 3.75\, m$$

thus both necessitating very long cavities for ultrafast OPOs. In practice, the extra path length due to the nonlinear crystal should also be considered while calculating the synchronous cavity length.

In the context of cw OPOs, which are more sensitive to losses, the ring cavity has many advantages. The single-pass of the resonating wave through the nonlinear crystal reduces the loss due to inherent material absorption and crystal coating, hence reducing the threshold and minimizing the thermal effects in the nonlinear crystal. Additionally, it offers the possibility of introducing intracavity elements such as etalons for frequency selection, or additional nonlinear crystals for intracavity frequency conversion, at the second beam waist of the cavity. A typical 1 μm Yb-fiber laser pumped MgO:PPLN cw SRO in a ring cavity is shown in Fig. 2.11.

In order to design the above mentioned cavity configurations, we use ABCD matrix analysis. For the best performance of the OPO, we need optimum overlap of the pump beam and the resonant signal beam. This means that the confocal parameter of the pump beam must be equal to that of the signal beam. To achieve this, the focal point of the pump beam needs to be in the same position, at the center of the nonlinear crystal, as the focal point of the signal beam in the stable resonator. Using the Gaussian beam transformation matrices, the signal waist can be calculated at any position in the cavity.

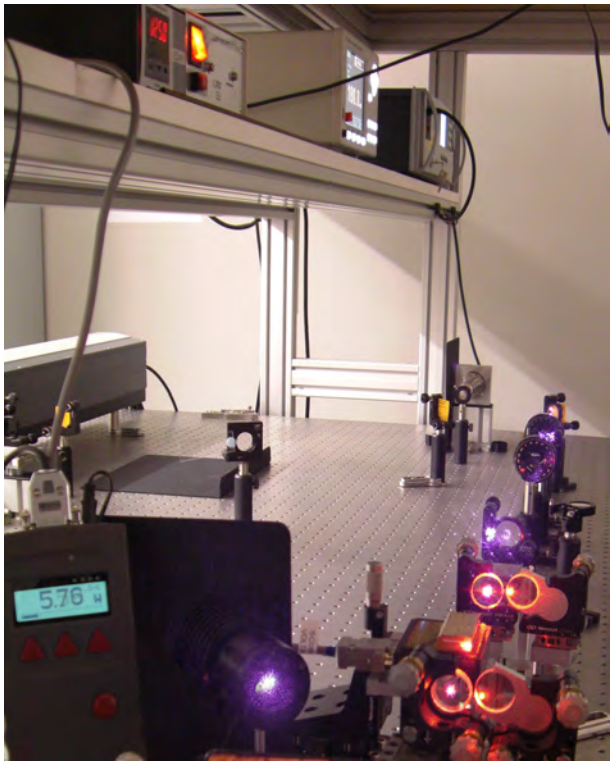

Figure 2.11: Yb-fiber laser pumped MgO:PPLN SRO in ring cavity.

2.8.1 Gaussian beam transformation matrices

Let us assume that a Gaussian beam is propagating in a straight line along z-direction with a minimum beam waist, w_0 at $z = 0$, i.e. $w(0) = w_0$. If the beam waist, $w(z)$, and radius of curvature, $R(z)$, of the wavefront is known at a specific location of the Gaussian beam, then the beam waist and radius of curvature of the beam at any position can be calculated using the following equations [67],

$$R(z) = z\left(1 + \frac{z_0^2}{z^2}\right) \tag{2.54}$$

$$w(z) = w_0^2\left(1 + \frac{z^2}{z_0^2}\right) \tag{2.55}$$

where $z_0 = \pi n w_0^2/\lambda$ is known as the Rayleigh range, $b = 2z_0$ is the confocal parameter, n is the refractive index, and λ is the wavelength of the Gaussian beam. The

Gaussian beam at a distance z can be expressed using the complex beam parameter

$$q(z) = z - iz_0 \tag{2.56}$$

The relationship of the complex beam parameter $q(z)$ with $R(z)$ and $w(z)$ is given by

$$\frac{1}{R(z)} = Re\left(\frac{1}{q(z)}\right) \tag{2.57}$$

$$\frac{1}{w^2(z)} = -\frac{\pi n}{\lambda} Im(\frac{1}{q(z)}) \tag{2.58}$$

The ray matrices, also known as ABCD matrices, relate the complex beam parameter q_1 at a plane 2 to the value q_0 at plane 1, as

$$q_1 = \frac{Aq_0 + B}{Cq_0 + D} \tag{2.59}$$

The general form of the ABCD matrix is $M = \begin{pmatrix} A & B \\ C & D \end{pmatrix}$, where A, B, C, D are the ray matrix elements. Ray matrix offers a convenient form of describing the propagation through various optical elements such as lenses, nonlinear crystals, and mirrors by using the corresponding transformation matrices. Some useful transformation matrices are listed in Table.2.2. The overall ABCD matrix can then be obtained by multiplication of the individual transformation matrices such that the order in which the matrices appear in the product is opposite to the order in which the corresponding optical elements are traversed by light.

Using these transformation matrices and the general condition for stability of the cavity, $-1 \leq (A + D)/2 \leq 1$, we can calculate the beam waist radius along the dimensions starting from center of the nonlinear crystal, to design a stable cavity. The typical cavity design plot for ring configuration is shown in Fig. 2.12, from which the various design parameters such as the distance between the cavity mirrors and optimum position of the crystal can be estimated.

Propagation over a distance d	$\begin{pmatrix} 1 & d \\ 0 & 1 \end{pmatrix}$
Refraction at a flat surface separated by two media of index n_1 and n_2	$\begin{pmatrix} 1 & 0 \\ 0 & \frac{n_1}{n_2} \end{pmatrix}$
Thin lens of focal length f	$\begin{pmatrix} 1 & 0 \\ \frac{-1}{f} & 0 \end{pmatrix}$

Table 2.2: Ray matrix operators.

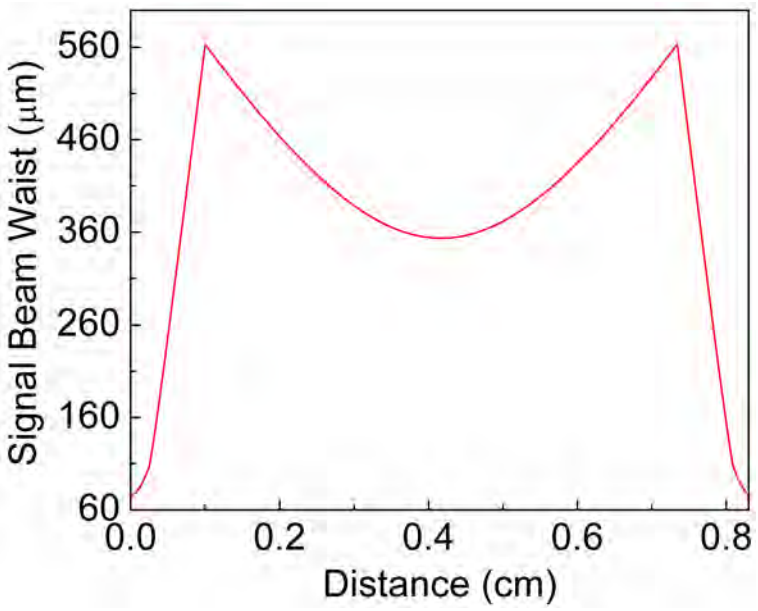

Figure 2.12: Signal beam waist in a ring cavity.

3 High-power MgO:PPLN cw OPO

This chapter constitutes the following publication:

1. *Optimally-output-coupled, 17.5 W, fiber-laser-pumped continuous-wave optical parametric oscillator*

   S. Chaitanya Kumar, R. Das, G. K. Samanta, and M. Ebrahim-Zadeh

   Applied Physics B-Lasers and optics **102**, 31–35 (2011).

3.1 Motivation

Continuous-wave (cw), singly-resonant optical parametric oscillators (SROs) are viable sources of high-power, widely tunable radiation in the near- to mid-infrared (mid-IR) for a variety of applications such as spectroscopy and trace gas sensing [68]. When combined with the recent advances in fiber laser technology, they offer a viable route to the realization of compact, portable, robust, and cost-effective sources, potentially capable of providing multiwatt output powers at high efficiency. Earlier efforts on the development of cw SROs have exploited the most widely established quasi-phase-matched nonlinear material, periodically poled $LiNbO_3$(PPLN) and MgO:PPLN [68, 69, 70, 72, 74]. However, attainment of high optical powers in the near- and mid-IR remains an experimentally challenging task, essentially due to heavy thermal loading of the nonlinear crystal resulting from the high intracavity signal power at increased pump powers. This can lead to effects such as thermally induced optical bistability [70], saturation, and subsequently a substantial drop in efficiency, thus limiting the available output power [71]. To date, a maximum of

10 W of idler at 3 μm from 50 W of pump at 20% efficiency has been achieved in a cw SRO [69]. In order to increase the extraction efficiency, various schemes such as signal output coupling [72, 77] and intracavity frequency doubling [78] have been employed to minimize thermal effects, hence retaining high output power. Implementation of output coupling has also extended the tuning range together with improved extraction efficiency up to 59%, resulting in a total power of 8.6 W (5.1 W signal, 3.5 W idler) for 15 W of pump power [72]. Hence, optimization of output coupling becomes a critical issue for power scaling of cw SROs to multiwatt levels, while maintaining output stability and extraction efficiency.

In this chapter, we describe a stable and high-power cw SRO for the near- to mid-IR based on MgO:PPLN, which can provide as much as 17.5 W of total power (9.8 W signal, 7.7 W idler) at an overall extraction efficiency of 61%, by deploying optimized signal output coupling. Wide tunability in the signal wavelength range over 1506-1945 nm and a corresponding idler tuning range across 2304-3615 nm is achieved. The cw SRO delivers an idler power with a peak-to-peak power stability of 5% over 14 hours in a TEM_{00} spatial profile. We also compare the performance of the output coupled SRO with the conventional SRO in the absence of signal output coupling. To the best of our knowledge, this is the highest total power and good long-term power stability, achieved to date from a cw OPO based on MgO:PPLN.

3.2 High-power cw SRO

3.2.1 Experimental set-up

A schematic of the experimental setup is shown in Fig. 3.1. The pump source is a cw, single-frequency Yb fiber laser (IPG Photonics, YLR-30-1064-LP-SF), delivering up to 30 W at 1064 nm in a linearly polarized beam of 4 mm diameter in TEM_{00} spatial mode ($M^2 < 1.01$), with a nominal linewidth of 89 kHz. In order to maintain stable output characteristics, the laser is operated at maximum power and a combination

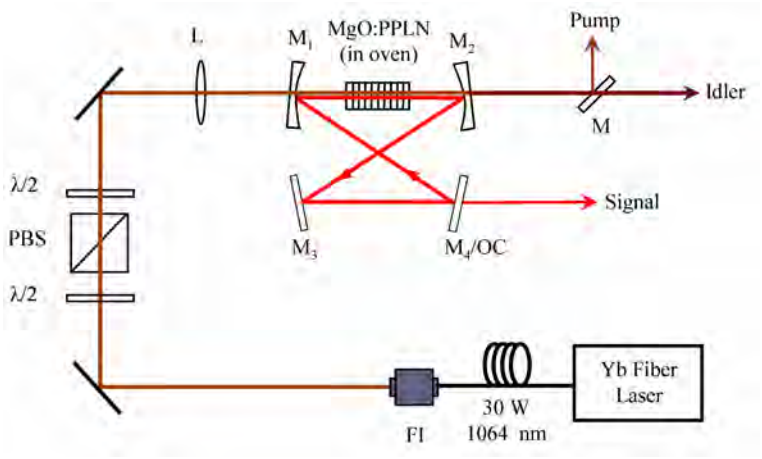

Figure 3.1: Experimental setup for Yb-fiber-laser-pumped, high-power cw OC-SRO based on MgO:PPLN crystal. FI: Faraday isolator, λ/2: half-wave plate, PBS: polarizing beamsplitter, M: dichroic mirror.

of a half-wave plate and polarizing beamsplitter is used as variable attenuator. A second half-wave plate controls the polarization for phase-matching in the nonlinear crystal. The nonlinear crystal is a 50-mm-long, 1-mm-thick, 5% MgO:PPLN with five grating periods, Λ=29.5 to 31.5 μm, in steps of 0.5 μm. The crystal is housed in an oven with a stability of ±0.1 °C, which can be tuned from room temperature to 200 °C. The SRO cavity is a symmetric ring, comprising two concave mirrors, M_1 and M_2 (r=150 mm), and two plane mirrors, M_3 and M_4. All mirrors have high reflectivity (R>99%) over 1.3-1.9 μm and high transmission (T>90%) over 2.2-4 μm, ensuring singly-resonant oscillation. Out-coupled SRO (OC-SRO) operation is achieved by replacing mirror M_4 by a suitable output coupler (OC) across 1.6-1.7 μm. A dichroic mirror, M, separates the generated idler from the pump.

3.2.2 Design and optimization of the cavity

A proper cavity design should ensure the optimum focusing condition at the center of the nonlinear crystal. In order to optimize the SRO, we used a focusing parameter [59],

$$\xi = \frac{l}{b_p} \tag{3.1}$$

where b_p is the confocal parameter of the pump defined as

$$b_p = \frac{k}{w_{op}} \tag{3.2}$$

with

$$k = \frac{2\pi n_p}{\lambda_p} \tag{3.3}$$

Here l=50 mm is the length of the nonlinear crystal, n_p, λ_p, w_{op} are the refractive index, wavelength and waist radius of the pump beam inside the nonlinear crystal, respectively. In this experiment, the pump beam is confocally focused to a beam waist radius of $w_{op} = 63\mu m$, corresponding to a focusing parameter of $\xi \sim 1$ at the centre of the nonlinear crystal. The cavity design ensures optimum overlap of pump and resonant signal at the center of the crystal ($b_p \sim b_s$), resulting a signal waist radius of $w_{os} \sim 76\ \mu m$.

3.3 Results and discussion

3.3.1 SRO power scaling

To study output power characteristics, the oscillator is initially configured as a SRO. The power scaling is performed at a constant temperature using different grating periods. The variation of the idler power as a function of the input pump power for grating period Λ=31.5, 30.5, 31 μm of the nonlinear crystal is shown in Fig. 3.3. At constant temperature of 120 °C, an output idler power of 8.6 W is generated for a pump power of 26.6 W, representing an idler efficiency of 32.3% at 2697 nm for the Λ=31.5 μm grating period. The threshold of the SRO is recorded to be 2.6 W. Similar measurements for gratings 30.5, 30 μm at fixed temperature of 100 °C has resulted in the generation of a maximum idler power 7.6 W, 6.9 W, corresponding to

an idler efficiency of 28.6%, 24.4% at 3301 nm, 3514 nm, respectively. The threshold pump power of the SRO is recorded to be 5 W at 3301 nm (30.5 μm) and 6 W at 3514 nm (30 μm). No saturation effect is observed in the idler power.

The power scaling measurement in case of 31 μm grating at a temperature of 100 °C is shown in Fig. 3.3. A maximum idler power of 8.6 W is generated for a pump power of 28.6 W at an idler efficiency of 30%. The corresponding idler wavelength is 3061 nm. The threshold pump power in this case is recorded to be 3.6 W. Also shown in Fig. 3.3 is the variation of the pump depletion as a function of the input pump power. Beyond a pump power of 12 W, pump depletion reaching >70% is recorded.

3.3.2 SRO tuning

In cw SROs, various wavelength tuning protocols have been implemented and are by now well-established. Coarse wavelength tuning can be obtained by changing the grating period [73] or varying the temperature of the nonlinear crystal [74], while continuous, mode-hop-free, fine tuning can be achieved by using an etalon in the cavity [73]. Tuning the pump laser results in rapid and continuous mode-hop-free tuning of up to several gigahertz [75]. Another tuning method based on the use of a diffraction grating has also been recently reported [76]. In this case, the SRO is tuned by changing the temperature of the nonlinear crystal, its temperature and also by translating the nonlinear crystal.

Temperature tuning and thermal effects

Temperature tuning is achieved by changing the temperature of the nonlinear crystal for a fixed grating period. For this purpose, the MgO:PPLN crystal is housed in an oven whose temperature can be controlled from room temperature to 200 °C. Further tuning is achieved by changing the grating period and for this purpose MgO:PPLN crystal is mounted on a translation stage to access the multiple grating periods of the

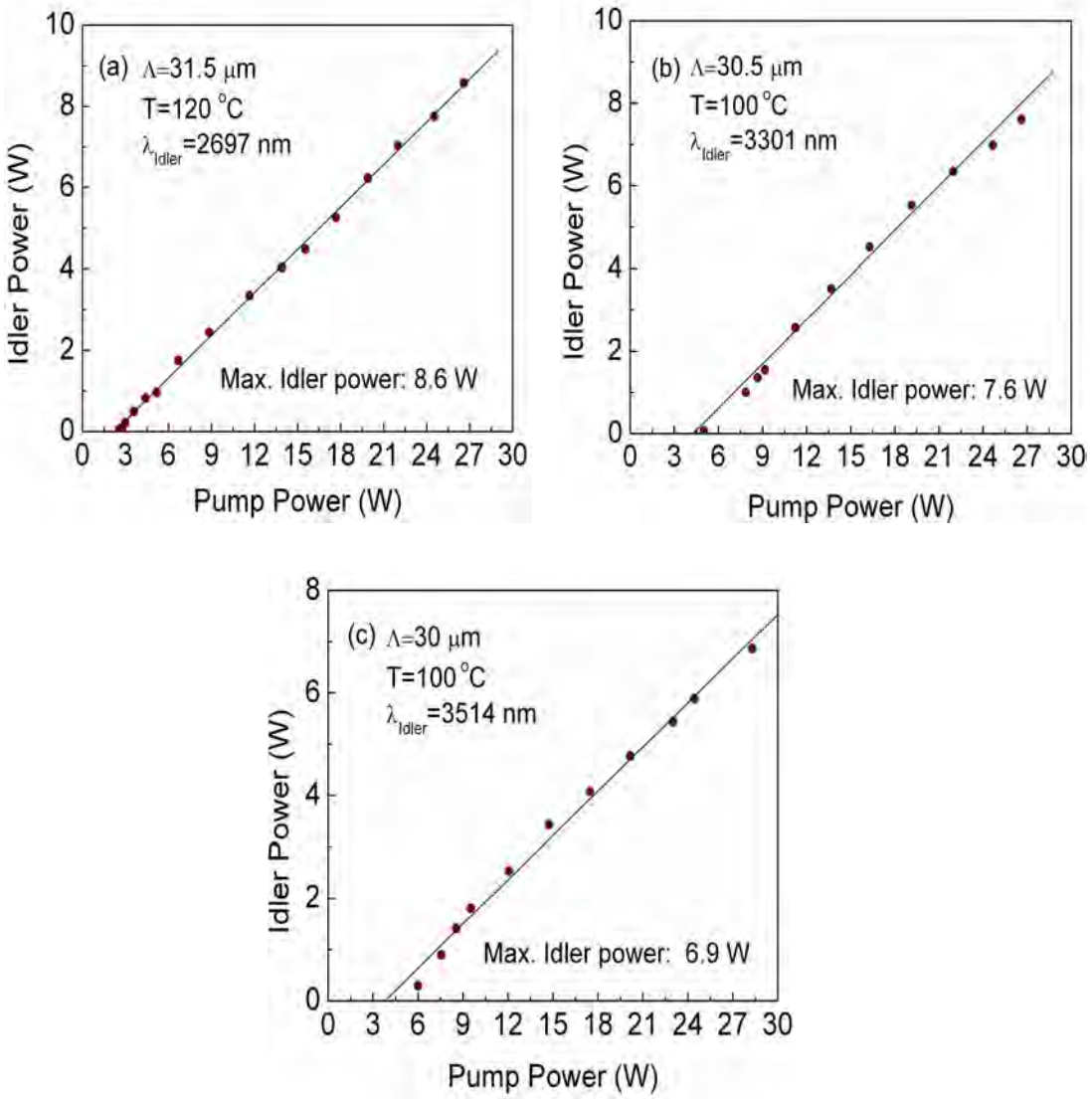

Figure 3.2: Variation of the idler power as a function of input pump power for a grating period of (a) 31.5 μm, (b) 30.5 μm, (c) 30 μm.

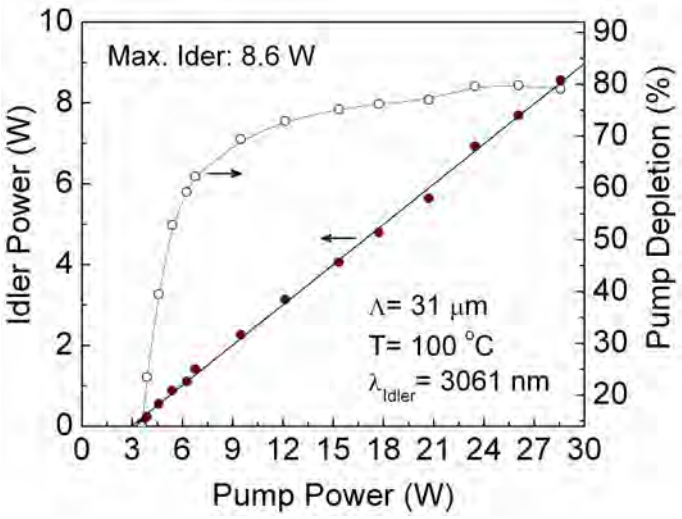

Figure 3.3: Variation of the idler power and pump depletion as a function of input pump power for a grating period of 31 μm.

nonlinear crystal. Fig. 3.4 shows the typical temperature tuning curve of MgO:PPLN cw SRO for Λ=31 μm. We measured the signal wavelength by monitoring a small amount of leakage from the plane mirror arm of the SRO using a spectrum analyzer, and the idler wavelength is monitored using a mid-IR wavemeter. The solid and open circles are the experimentally recorded data, while the solid line is theoretical calculation based on the Sellmeier equation [65].

In the SRO, by changing the temperature from 55 °C to 200 °C, we generated idler wavelengths across 3147–2787 nm, providing a total tuning of 360 nm. However, we were not able to tune the device down to room temperature, because of the heavy thermal load of the nonlinear crystal due to high intracavity signal power. In order to efficiently manage these thermal effects we implemented signal output coupling, thereby reducing the thermal load of the nonlinear crystal and enable further tuning of the SRO below 55 °C.

3.3.3 Signal output coupling and optimization

In order to implement the output coupling, one of the cavity mirrors, M_4, is replaced by an output coupler. Also, while implementing the OC-SRO, the choice

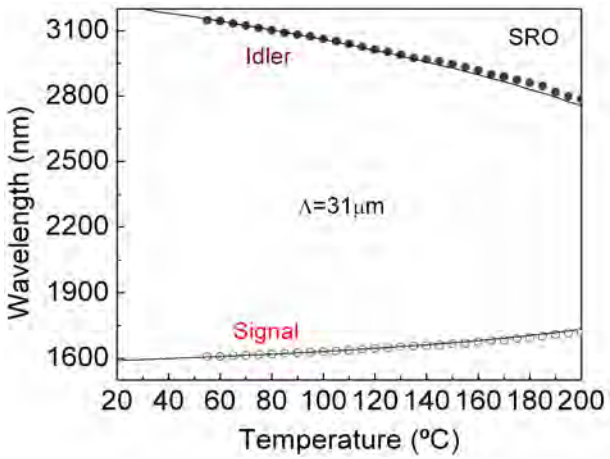

Figure 3.4: Signal and idler wavelength tuning of the cw SRO as function of temperature for a grating period of 31 μm.

of the output coupler is important. A proper choice of the output coupler enables efficient management of thermal effects by extracting substantial amount of signal power from the cavity without much compromise in the idler power. Hence, we performed the investigation of optimal out-coupling by employing different OCs. For the optimization of output coupling we choose the grating period of 31 μm and five different output couplers with signal transmissions from T∼3% to 6% are used. The OC-SRO is optimized for the maximum idler in all the cases. Figure 3.5 shows the simultaneously extracted idler and signal power from the OC-SRO for different OCs at a maximum available pump power of 28.6 W. The measurements were performed at the centre of the tuning range for Λ=31 μm at 100 °C.

As evident from the plot, an increase in OC transmission from 3% to 3.8% resulted in a rise in signal power from 7.8 W to 9.8 W, without significant compromise in idler power. Further increase in OC transmission results in the drop in signal and idler power to 7.7 W and 6 W, respectively, at 6% output coupling. As a consequence of increased output coupling, the OC-SRO threshold increases from 7.2 W at 3% to 15.4 W at 6% (inset, Fig. 3.5), and the intracavity signal power estimated from the OC transmission varies from 259 W (T∼3%) to 129 W (T∼6%). For optimal output coupling of ∼3.8%, a maximum signal power of 9.8 W at 1627 nm, together

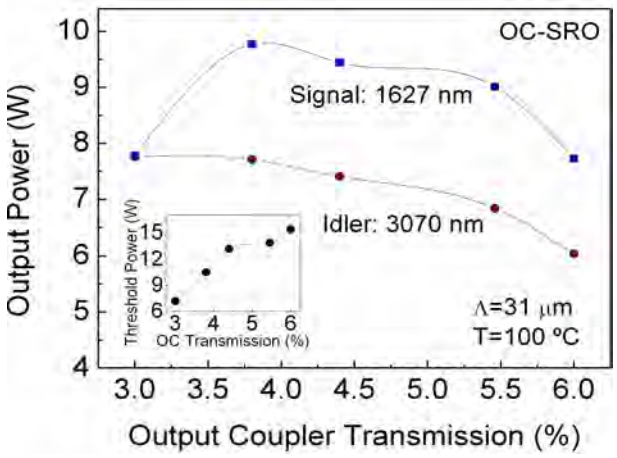

Figure 3.5: Variation of extracted signal (1627 nm) and idler (3070 nm) power with OC transmission. Inset: Variation of threshold pump power with OC transmission.

with 7.7 W of idler at 3070 nm, is extracted for 28.6 W of input power at a pump depletion of 69.4%. Under this condition, the OC-SRO threshold is 10.5 W. So, the available pump power enables OC-SRO operation at ∼2.74 times threshold, where a maximum pump depletion is theoretically predicted [79], confirming that this is the optimum output coupling for our device.

3.3.4 OC-SRO power scaling

We investigated power scaling of the optimal OC-SRO (T∼3.8%) compared with the SRO, for the same grating period (Λ=31 μm, 100 °C), as shown in Fig. 3.6. For the SRO, an idler power up to 8.6 W was obtained at 3061 nm for 28.6 W of pump at 30% extraction efficiency, with a threshold of 3.6 W and a pump depletion of 79%. No saturation of idler power was observed at this power level.

On the other hand, with the optimal OC-SRO, we were able to generate a total power of 17.5 W (9.8 W signal at 1627 nm, 7.7 W idler at 3070 nm) at an overall extraction efficiency of 61%. Also, we recorded a pump depletion of 69.4% for an optimally out-coupled SRO. This means that 88% of the down-converted pump is successfully extracted as output. Figure 3.7 shows the simultaneous power scaling

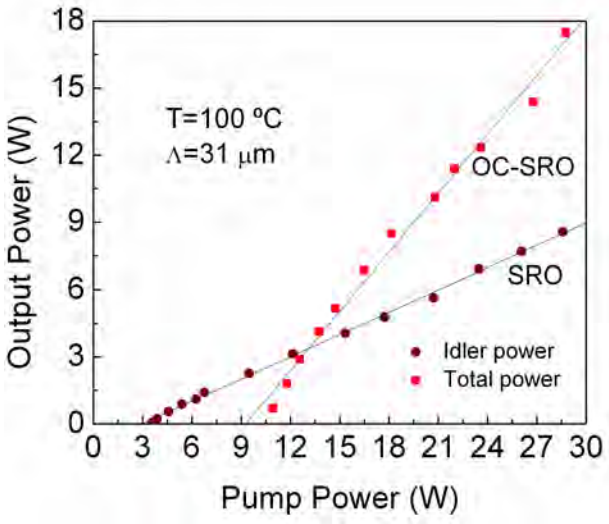

Figure 3.6: Total extracted output power as a function of pump power from SRO and OC-SRO.

of signal and idler in the OC-SRO for the optimal output coupling of 3.8%.

3.3.5 OC-SRO tuning

The temperature tuning curves of the OC-SRO for different grating periods are shown in Fig. 3.8. Unlike in case of the SRO, here we are able to tune the OC-SRO below 55 °C and down to 30 °C. The solid and open circles are the experimentally recorded data, while the solid lines are theoretically calculated from the relevant Sellmeier equations [65]. In order to cover the wide signal wavelength range, we used different output couplers. It is to be noted that the output coupling is only optimized at the single wavelength.

3.3.6 Power across the tuning range

We have also characterized the output power of the OC-SRO across the full tuning range by translating and varying the temperature of the MgO:PPLN crystal. Figure 3.9 shows the simultaneously measured signal and idler power across the tuning range of the OC-SRO based on multi-grating MgO:PPLN crystal, using different output

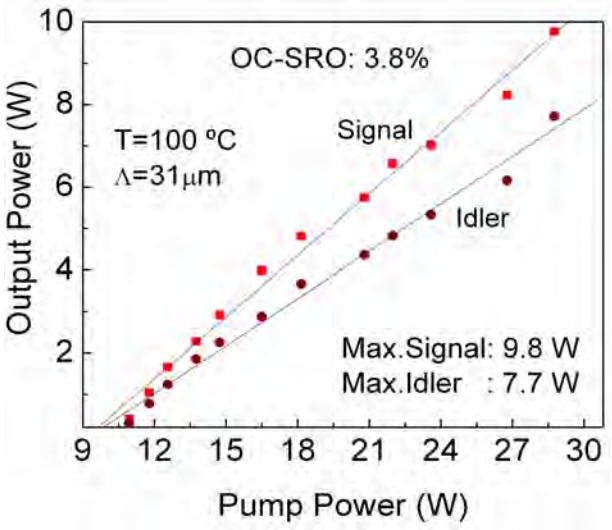

Figure 3.7: Power scaling of signal and idler in OC-SRO at a temperature of 100 °C, Λ=31 μm.

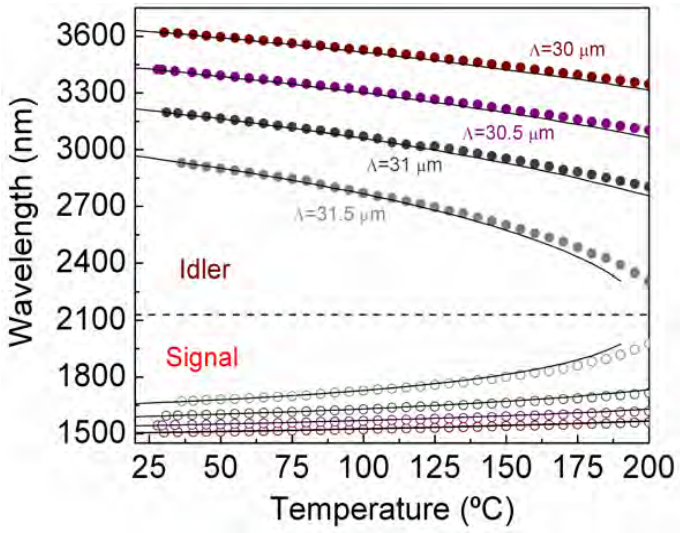

Figure 3.8: Signal and idler wavelength tuning of an OC-SRO based on multi-grating MgO:PPLN as a function of temperature.

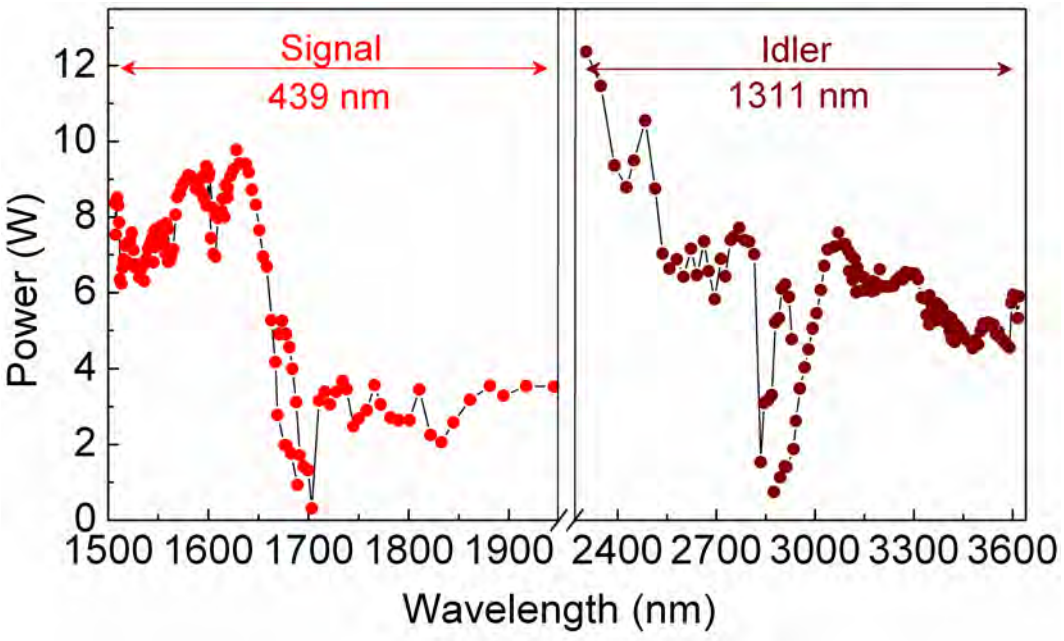

Figure 3.9: Power across the full tuning range of the OC-SRO based on multi-grating MgO:PPLN.

couplers to cover the wide signal wavelength range. Signal wavelength tuning of 439 nm, ranging from 1506-1945 nm, with a maximum signal power of 10 W at 1628 nm is achieved. The corresponding idler wavelength tuning of 1311 nm, covers 2304-3615 nm, with a maximum idler power up to 12 W at 2305 nm. Hence, a total signal and idler tunability of 1750 nm is achieved from the OC-SRO.

Figure 4.2 shows the characterization of the output power from SRO and OC-SRO across the tuning range, for a grating period of 31 μm, by varying the temperature of the MgO:PPLN crystal. In the SRO, by changing the temperature from 55 °C to 200 °C, we generated idler wavelengths across 3147–2787 nm, providing a total tuning of 360 nm, as shown in Fig. 4.2(a). For a pump power of 28.6 W, idler powers >7 W and pump depletion >65% were recorded over almost the entire tuning range, except for a drop in the idler power around 2.8 μm, corresponding to the OH^- absorption in MgO:PPLN. However, we were not able to tune the device down to room temperature, because of heavy thermal loading of the crystal. In the OC-SRO, by employing an OC of T∼3–5% in 1.6–1.7 μm range, idler tuning over 3196–2803

nm together with signal tuning across 1594–1714 nm was obtained, enabling room-temperature operation of OC-SRO at 31 °C with a total power of 15.7 W (9.1 W of signal at 1594 nm, 6.6 W of idler at 3196 nm), as shown in Fig. 4.2(b,c). Thus, the use of output coupling extended the idler wavelength range by 33 nm compared to SRO. Using the OC-SRO, we were also able to extract signal powers from 9.1 W at 1594 nm (31 °C) to 7.3 W at 1714 nm (200 °C), with the corresponding idler power varying from 6.6 W at 3196 nm to 5.6 W at 2803 nm. The OC values were not optimized at each wavelength, so still higher powers across the tuning range are expected. The drop in signal and idler power at higher temperatures is due to the lower OC transmission for the corresponding wavelengths and the dip around 2.8 μm is again due to the OH^- absorption in MgO:PPLN.

Due to the lack of a suitable interferometer in our laboratory, we were unable to measure the linewidth of the signal and idler. Given the single-frequency nature of the fiber laser pump source with typical linewidth of 100 kHz, we expect the generated signal and idler waves from the OC-SRO to also be single-mode, which is an essential requirement for spectroscopy and trace gas sensing. However, further confirmation of the single-frequency nature of the OC-SRO output requires a suitable high-resolution scanning Fabry-Perot interferometer.

Thermal effects

We also observed a significant shift in idler wavelength generated in the OC-SRO compared to that at a similar temperature in SRO due to thermal load, which confirms the effect of crystal heating in the SRO and its efficient management by optimal output coupling in the OC-SRO. For example, near 100 °C, the idler wavelength is measured as 3061 nm and 3070 nm in the SRO and OC-SRO, respectively, indicating an increase of 9 nm in the idler wavelength in the optimal OC-SRO (T∼3.8%) compared to SRO. This corresponds to a temperature drop of ∼5 °C in MgO:PPLN, as calculated from the Sellmeier equations [65]. Hence, output coupling not only

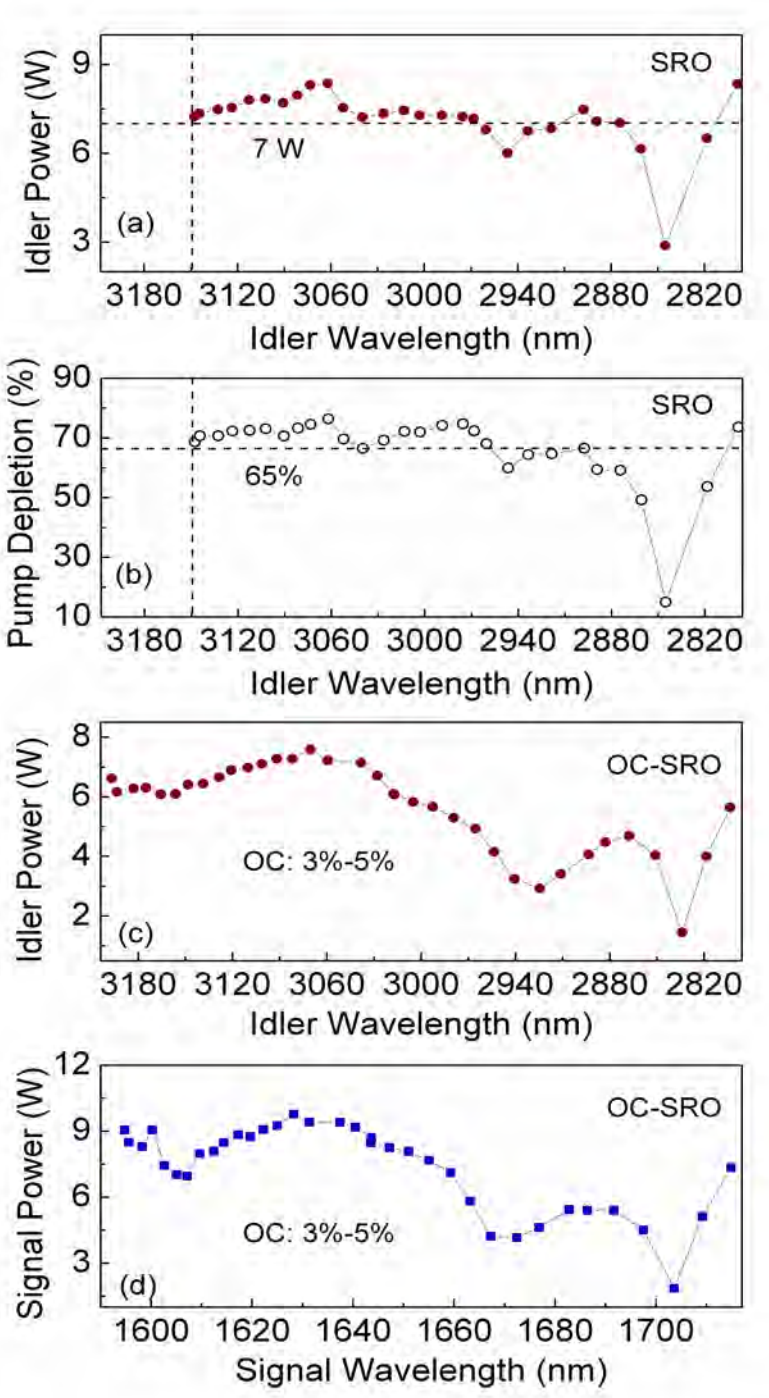

Figure 3.10: (a) Idler power and (b)pump depletion of an SRO and (c) Idler power, (d) signal power of an OC-SRO across the tuning range for grating period of 31 μm.

increases the overall extraction efficiency and helps manage thermal effects, but also extends the tunability of the device.

Cascaded and Raman processes

In SRO operation at higher pump power level, in addition to the peak at the expected signal wavelength, we also observed additional spectral components red-shifted towards the longer wavelength by nearly 12 nm, but we did not observe any blue-shifted peaks. For example, when pumping at the maximum power of 28.6 W, a signal wavelength of 1631 nm and an additional peak at 1643 nm were observed at 100 °C for a grating period of 31 μm. The observed additional spectral components are attributed to Raman lasing [72] or cascaded nonlinear processes [81]. On the other hand, when operating in the OC-SRO configuration, no such additional spectral components were observed, due to the significantly reduced intracavity signal intensity suppressing Raman lasing and cascaded nonlinear effects below threshold. For example, the estimated intracavity power reduces from >600 W at 100 °C, corresponding to a signal wavelength of 1631 nm in the SRO, to 257 W in the OC-SRO for 3.8% OC at the same temperature, corresponding to a signal wavelength of 1627 nm. Hence, no additional spectral components were observed in the OC-SRO configuration.

3.4 Power stability and beam quality

We also investigated the power stability of the device in the two configurations at the maximum generated idler power. For the SRO, at a temperature of 100 °C (idler at 3061 nm), we measured a stability of 17.4% over 1 hour. For the OC-SRO, at a temperature 100 °C (idler at 3070 nm), we recorded a peak-to-peak stability of 13.6% over 1 hour. However, in the OC-SRO, at a temperature of 44 °C (idler at 3174 nm), we measured a long-term peak-to-peak stability of 5% over 14 hours at 7 W of idler power, as shown in Fig. 3.11. The corresponding stability in the fiber pump laser was measured to be 0.5% over 10 hours. We attribute the improved stability of the

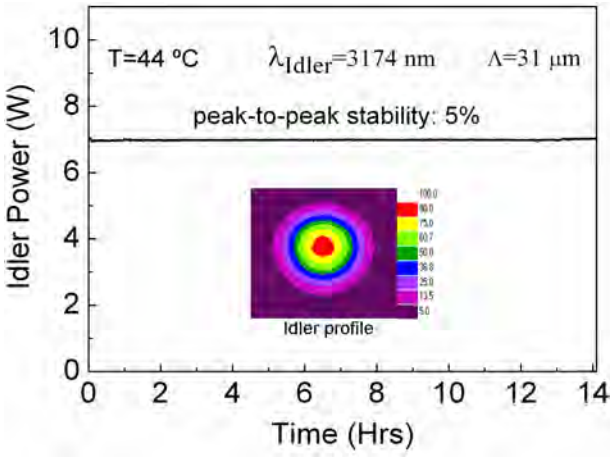

Figure 3.11: Long-term power stability and far-field spatial profile of the idler beam from OC-SRO at 44 °C corresponding to 3174 nm.

OC-SRO at 44 °C to the better temperature control of the nonlinear crystal. It was observed that the smaller the difference between the set oven temperature and the ambient temperature, the better the stability of the oven. Therefore, maintaining a constant oven temperature at a high temperature is more difficult than that close to room temperature. We believe this is the main reason for improved power stability close to room temperature. We did not observe any degradation in power stability or output beam quality over the measurement period, thus confirming the absence of photorefractive damage in the crystal even at such high power levels. We can thus conclude that the improvement in power stability is due to better control of crystal temperature close to room temperature, confirming another important advantage of the OC-SRO. It has been shown that, by careful thermal control of the nonlinear crystal, long-term power stability can be achieved without the need for an intracavity etalon or actively stabilizing the OPO with an external reference cavity [71]. Hence, similar improvement in the power stability is also to be expected by employing a temperature controller with stability better than ±0.1 °C or by using a thermo-electric cooler. In the SRO configuration, the minimum operating temperature could not be reduced below 55 °C due to the heavy thermal loading of the crystal in the absence of signal output coupling.

We measured the quality factors of the output beam from the OC-SRO, where we obtained M_x^2∼1.28 and M_y^2∼1.22 for the idler at 3070 nm and M_x^2∼1.29 and M_{y}^2∼1.37 for the signal at 1627 nm. For the SRO, we obtained M_{x}^2∼1.3 and M_{y}^2∼1.22 for idler at 3061 nm. We attribute the larger M^2 value for the signal to the stronger impact of the thermal lens on the signal beam quality than that of the idler. The thermal lens itself is caused primarily by the absorption of the high intracavity signal field, although absorption at pump and idler wavelengths cannot be completely ruled out. Since the signal is a resonant mode of the SRO cavity, it is expected to be highly sensitive to small changes in mode-matching with the pump, as well as changes in the cavity stability conditions caused by the intracavity thermal lens formed in the crystal. On the other hand, the idler is generated in a single pass through the crystal as a result of mixing between the single-pass pump and the resonant signal beam. As such, the effect of the thermal lens is expected to be less detrimental to the quality of the idler beam than that of the signal, and so the impact on the M^2 value of idler is not as severe as that on the M^2 value of the signal beam. Also shown in the inset of Fig. 3.11 is the spatial profile of the idler beam from the OC-SRO at 44 °C and at 7 W, measured at a distance of 1 m away from the output, using a pyroelectric beam profiler. The measurement confirms a TEM_{00} spatial mode.

3.5 Conclusions

In this chapter, we have demonstrated a stable, high-power, fiber-laser-pumped, cw optical parametric oscillator in the OC-SRO configuration. The OC-SRO is widely tunable from 1506-1945 nm in the signal wavelength range with a maximum signal power of 1628 nm. In the idler wavelength range, the OC-SRO is tunable from 2304-3615 nm with a maximum idler power of 12 W at 2305 nm. This corresponds to a total tuning range of 1750 nm. The output coupling optimization and thermal effects have been studied. Using 31μm grating, the OC-SRO provides 17.5 W of power in the near- to mid-IR infrared at an external efficiency of 61%, with nearly 90% of

down-converted pump power extracted as useful output. This compares with a total output power of 8.6 W at 30% extraction efficiency in the SRO configuration. The OC-SRO can operate down to 44 °C, delivers TEM_{00} beam quality, and exhibits long-term power stability of 5% over 14 hours. Further improvements in power and stability are possible by optimizing output coupling across the tuning range and providing better isolation from mechanical vibrations.

4 High-power MgO:sPPLT cw SRO

This chapter constitutes the following publication:

1. *High-power, continuous-wave, mid-infrared optical parametric oscillator based on MgO:sPPLT*

   S. Chaitanya Kumar and M. Ebrahim-Zadeh

   Optics Letters **36**, 2578–2580 (2011).

4.1 Motivation

High-power, continuous-wave (cw) optical parametric oscillators (OPOs) are attractive sources of widely tunable coherent radiation spanning the visible to mid-infrared (mid-IR) [4], addressing a variety of applications from quantum optics [82] to environmental monitoring [68]. Such sources in the mid-IR are also of interest as first-stage pumps for cw OPOs in tandem, to extend the spectral coverage of these devices beyond the current practical limit of $\sim$4 μm imposed by the onset of absorption in oxide-based nonlinear crystals. To date, practical development of high-power mid-IR cw OPOs has relied mainly on the widely established quasi-phase-matched (QPM) nonlinear material, periodically-poled $LiNbO_3$ (PPLN), providing multiwatt and widely tunable radiation across 1.3-4 μm in the mid-IR [33, 34], with as much as 17.5 W of total power at 61% overall extraction efficiency recently achieved in a signal-output-coupled cw OPO based on MgO:PPLN, and described in chapter 3 [34]. However, overcoming detrimental thermal effects due to the resonant signal, as well as the non-resonant idler at mid-IR wavelengths in PPLN is still a challenge

[33, 34]. The emergence of new QPM ferroelectric materials, particularly MgO-doped stoichiometric periodically-poled $LiTaO_3$ (MgO:sPPLT), with improved optical and thermal properties [41], has lead to important new advances in nonlinear frequency conversion techniques, including single-pass SHG of infrared fiber lasers into the green at unprecedented efficiencies [41, 43, 44] and visible-pumped, near-IR OPOs [83]. In spite of a lower effective nonlinear coefficient (d_{eff}∼9 pm/V) than PPLN (d_{eff}∼16 pm/V), increased resistance to photorefractive damage and higher thermal conductivity along with increased optical damage threshold [84] make MgO:sPPLT an attractive new alternative to overcome performance limitations of cw PPLN-based OPOs due to thermal effects. Progress in poling technology has also enabled the fabrication of bulk MgO:sPPLT crystals with improved optical quality over longer interaction lengths up to 30-40 mm and in wide apertures [85], opening up new possibilities for the development of practical cw OPOs from visible to the mid-IR in high-power singly-resonant oscillator (SRO) configuration. Moreover, $LiTaO_3$ is considered to exhibit lower absorption in the 3-4 μm spectral range than $LiNbO_3$, making it a potential candidate for high-power mid-IR generation.

Earlier work on mid-IR OPOs based on $LiTaO_3$ pumped at 1064 nm have been in the pulsed regime, including a nanosecond OPO based on PPsLT [85] and a high energy OPO based on large-aperture MgO:sPPLT pumped by Q-switched Nd:YAG laser [86]. In these reports, mid-IR idler power scaling has not been studied. To our knowledge, cw OPOs based on MgO:sPPLT pumped at 1064 nm, for mid-IR generation, have not been previously investigated. It would thus be of great interest to explore the feasibility of using MgO:sPPLT in cw OPOs pumped at 1064 nm, for the generation of high-power mid-IR radiation.

In this chapter, we present a cw OPO based on MgO:sPPLT pumped at 1064 nm, providing high optical powers with wide tuning in the mid-IR. The SRO is tunable over 430 nm with an idler power >4 W over more than 60% of the tuning range and a peak-to-peak power stability of 12.8% over 5 hours at 3299 nm. We also

investigate mid-IR power scaling of the device and compare its performance with the well-established MgO:PPLN cw SRO pumped at 1064 nm.

4.2 Experimental setup

The configuration of the cw SRO based on MgO:sPPLT is similar to that in our earlier work [34]. The pump source is a cw, single-frequency Yb fiber laser (IPG Photonics, YLR-30-1064-LP-SF), delivering up to 30 W at 1064 nm in a linearly polarized beam of 4 mm diameter in TEM_{00} spatial mode (M^2<1.01), with a linewidth of 89 kHz. The MgO:sPPLT crystal (HC Photonics, Taiwan) is a 30-mm-long, 1-mm-thick sample with six grating periods from Λ=29.15 μm to 30.65 μm. It is housed in an oven with a temperature stability of ±0.1 °C. The SRO cavity is a symmetric ring, formed by two concave (r=100 mm) and two plane mirrors. All mirrors (LaserOptik, Germany) have high reflectivity (R>99%) over 1.3-1.9 μm and high transmission (T>90%) over 2.2-4 μm, ensuring SRO operation. For frequency control, a 500-μm-thick uncoated fused silica etalon (free spectral range, FSR∼205 GHz) is used at the second cavity waist between the plane mirrors. The pump beam is confocally focused to a beam radius of 48 μm (ξ∼1) at the centre of the crystal. The cavity design ensures optimum overlap of pump and resonant signal at the center of the crystal (b_p∼b_s), with a signal waist radius of 58 μm, where b_p, b_s are the confocal parameters of the pump and signal beam, respectively. A dichroic mirror separates the generated output idler from the pump. The total optical length of the cavity including the crystal and the etalon is 575 mm, corresponding to a FSR∼522 MHz.

4.3 SRO tuning

In order to characterize the cw SRO with regard to tunability, we varied the temperature of the MgO:sPPLT crystal from 40 °C to 200 °C. The temperature tuning curves for two grating periods, Λ=30.65 μm and 30.15 μm, are shown in Fig. 4.1 .

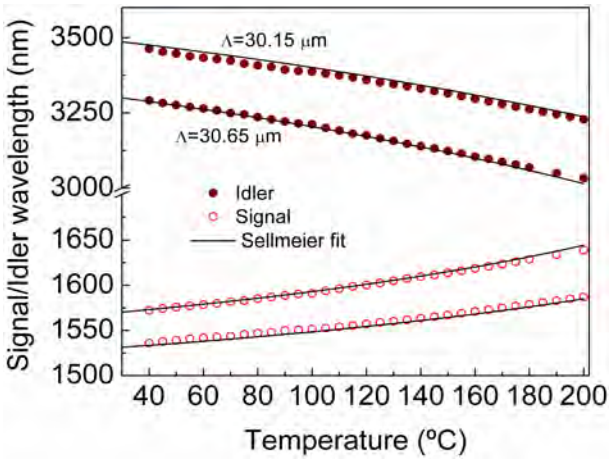

Figure 4.1: Temperature tuning curves of 1064 nm-pumped MgO:sPPLT-based cw SRO.

The signal wavelength was monitored using a near-IR spectrum analyzer, while the idler wavelength was measured using a wavelength meter. The solid lines are the theoretical tuning curves calculated from the relevant Sellmeier equations [57]. From Fig. 4.1, it can be seen that the experimental measurements are in good agreement with the calculated tuning curves.

Figure 4.2(a) shows the idler power extracted from the MgO:sPPLT cw SRO across the mid-IR tuning range. The data were obtained at an available pump power of 28.5 W at the input to the MgO:sPPLT crystal. Using the two grating periods (Λ=30.65, 30.15 μm), temperature tuning the SRO from room temperature to 200 °C resulted in the generation of idler wavelengths from 3032 to 3462 nm, corresponding to a total tuning range of 430 nm, with a maximum idler power of 5.5 W at 3221 nm and >4 W over more than 60% of the tuning range. The corresponding pump depletion across the tuning range is shown in Fig. 4.2(b), where it can be seen that pump depletion>50% is achieved over more than 40% of the tuning range. In addition to the idler, a small amount of signal power (few tens of milliwatts) is also obtained as leakage through the plane mirrors of the ring cavity over the entire tuning range. It is interesting to note that although the thermal load in the nonlinear crystal due to pump , idler and the high intracavity signal cannot be completely ignored, unlike

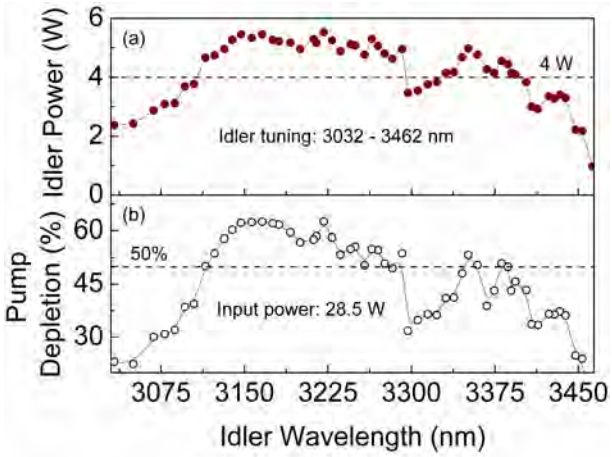

Figure 4.2: (a) Idler power and (b) Pump depletion across the tuning range of MgO:sPPLT cw SRO.

in MgO:PPLN cw SRO [34], high-power operation of the MgO:sPPLT cw SRO can be easily achieved at lower temperatures down to ∼35 °C. In contrast, operation of MgO:PPLN cw SRO at high-power is not attainable below ∼45 °C due to increased thermal effects [34]. The reduced thermal effects in MgO:sPPLT cw SRO can be attributed to intrinsic material properties including higher thermal conductivity (8.4 W/m-K), better transmission, and lower circulating intracavity signal power due to lower d_{eff} as compared to MgO:PPLN. Also, the shorter interaction length (30 mm) of the nonlinear crystal results in reduced absorption at pump, signal and particularly the idler, which become significant at longer wavelengths.

4.4 SRO power scaling

We performed the idler power scaling measurements at different wavelengths across the mid-IR tuning range. Fig. 4.3(a) shows the results obtained at 40 °C for a grating period of Λ=30.65 μm (idler wavelength of 3291 nm). Also included for comparison is the power scaling results for a cw SRO based on a 50-mm-long MgO:PPLN at a similar wavelength and operating under the same conditions, as described in chapter 3. Owing to the lower d_{eff} and shorter crystal length (30 mm), the threshold pump

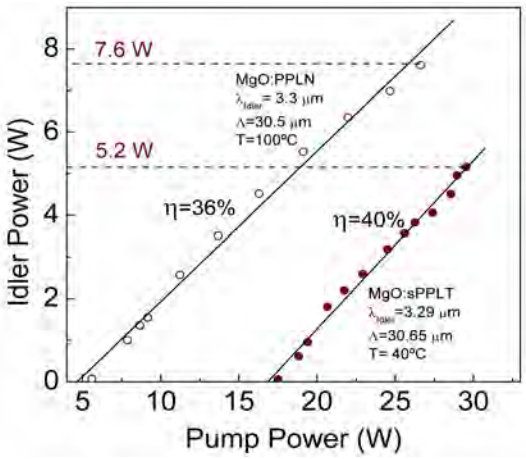

Figure 4.3: Idler power scaling comparison of MgO:PPLN and MgO:sPPLT cw SROs at ∼3.3 μm.

power of the MgO:sPPLT cw SRO is recorded to be 17.5 W, while that of the MgO:PPLN cw SRO is only 5.6 W. However, a maximum idler power of 5.2 W is generated for a pump power of 28.1 W at an idler efficiency of 18.5%, with no saturation in the idler power observed. The corresponding maximum idler power generated in MgO:PPLN cw SRO is 7.6 W for 26.6 W of pump power at an idler efficiency of 28.6%. On the other hand, we also characterized the SRO at a higher temperature of 100 °C using the same grating period, corresponding to an idler wavelength of 3212 nm, where we obtained a reduced pump power threshold of 13.2 W and generated as much as 5 W of idler for 29.8 W of pump power, as shown in Fig. 4.4. Also shown in Fig. 4.4 is the power scaling at an idler wavelength of 3403 nm, generating 3.8 W of idler for a pump power of 29 W, at temperature of 40 °C using a grating period of Λ=30.15 μm. These measurements confirm that despite the lower d_{eff} of the material resulting in higher pump threshold, multiwatt idler output powers in the mid-IR can be generated in cw SROs using MgO:sPPLT.

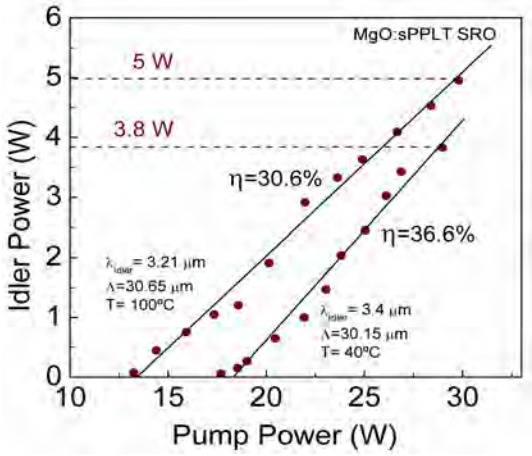

Figure 4.4: Idler power scaling of MgO:sPPLT cw SRO at 3.21 μm and 3.4 μm.

4.5 Idler power and frequency stability

Further, we recorded the idler power stability of the MgO:sPPLT cw SRO close to room temperature at ∼35 °C (with the oven switched off), corresponding to an idler wavelength of 3299 nm. We obtained a peak-to-peak power stability better than 12.8% over 5 hours at an idler power >4.5 W, as shown in Fig. 4.5. The corresponding signal spectrum at 1570 nm, obtained with the intracavity etalon, and recorded using a scanning Fabry-Perot interferometer (FSR=1 GHz, finesse=400), is also shown in the inset of Fig. 4.5, confirming single-frequency operation with an instantaneous linewidth of ∼21 MHz. Under similar conditions, we also recorded the idler wavelength stability using a wavelength meter (Bristol 721B-IR) with an absolute accuracy of 1 ppm and a measurement rate of ∼0.7 Hz. Fig. 4.6 shows the idler frequency stability recorded over a period of 1 hour, confirming a peak-to-peak stability ∼1 GHz without any active stabilization. With better thermal isolation and active control, further improvement in the SRO stability is expected. Also shown in the inset of Fig. 4.6 is the measured idler spectrum centered at 3299 nm with a FWHM linewidth ∼0.2 nm, limited by the resolution of the wavelength meter. Similar linewidths have been measured at other signal and idler wavelengths across the tuning range. Given the single-frequency nature of the Yb fiber laser pump

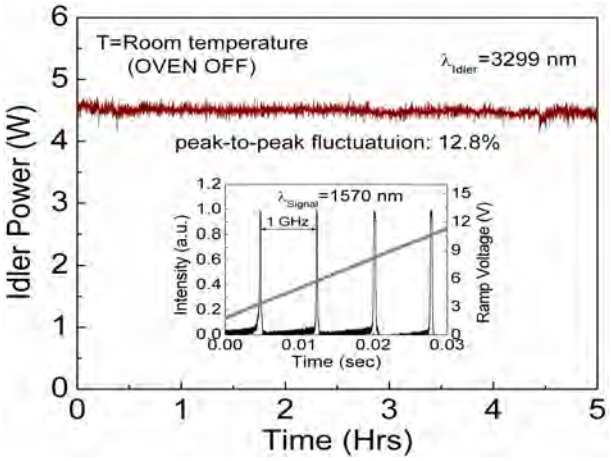

Figure 4.5: Idler power stability over 5 hours at room temperature and corresponding signal single-frequency spectrum.

source with a typical linewidth of 89 kHz, we expect the generated idler wave from the SRO, also to be in a single axial mode. However, accurate measurement of idler linewidth requires other methods such as beat frequency techniques.

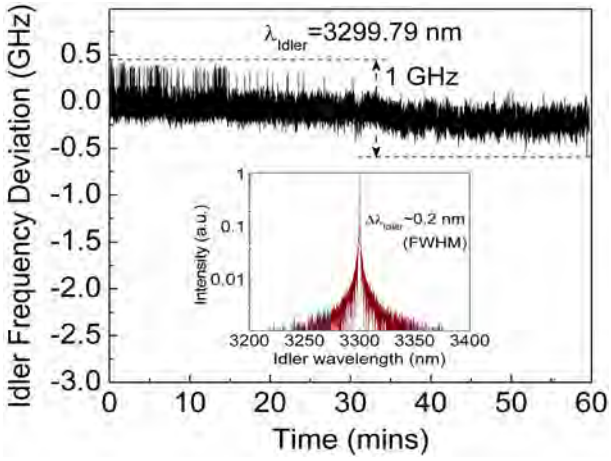

Figure 4.6: Idler frequency stability over 1 hours at room temperature, and corresponding idler spectrum (inset).

4.6 Conclusions

In this chapter, we have demonstrated the first cw SRO based on MgO:sPPLT pumped at 1064 nm, using an Yb fiber laser. The SRO is tunable over 430 nm,

generating up to 5.5 W of mid-IR power, with >4 W over 60% of the tuning range, and can be operated close to room temperature, where the signal and the idler linewidth are measured to be ∼21 MHz and ∼0.2 nm (limited by the resolution of the wavemeter), respectively. The high output power, low thermal effects, long-term power and wavelength stability of this cw SRO, and the potential for further power scaling, confirm that MgO:sPPLT is an attractive nonlinear material for multiwatt cw mid-IR generation.

5 Broadband, continuous-wave, mid-infrared OPO

This chapter constitutes the following publication:

1. *Broadband, high-power, continuous-wave, mid-infrared source using extended phase-matching bandwidth in MgO:PPLN*
   R. Das, **S. Chaitanya Kumar**, G. K. Samanta, and M. Ebrahim-Zadeh
   Optics Letters **34**, 3836–3838 (2009).

5.1 Motivation

High-power sources of broadband mid-infrared (mid-IR) radiation are of interest for a variety of applications including quantum optics [87], multi-component trace gas detection and analysis [88], single-shot spectroscopy of molecules [89], speckle-free imaging [90], and as potential seeds for high-energy ultrafast lasers and amplifiers. The widely established technique for broadband mid-IR generation is parametric down-conversion of femtosecond laser sources, in amplifier or oscillator configurations, using second-order nonlinear crystals [91, 92]. By relying on the broad bandwidth and high intensity of femtosecond pulses, the use of short interaction lengths in nonlinear crystals can permit exploitation of large phase-matching bandwidths, allowing efficient generation of broadband output under logarithmic gains. In the near- to mid-IR, the use of femtosecond Ti:sapphire lasers and amplifiers in combination with optical parametric generators (OPGs) and amplifiers (OPAs) [91], or

optical parametric oscillators (OPOs) [92], has permitted the generation of broadband radiation for the realization of optical frequency combs [93].

In the cw regime, however, the generation of high-power broadband radiation using parametric down-conversion is generally difficult. The low pumping intensities necessitate long interaction lengths for non-negligible gain, thereby limiting the available phase-matching bandwidth for parametric interaction, and thus preventing the use of broadband pump radiation. The low nonlinear gains also preclude the exploitation of single-pass OPG/OPA schemes, making the deployment of an OPO in resonant cavities imperative. As such, successful operation of cw OPOs has traditionally relied on the deployment of single-mode or narrow-linewidth pump sources in combination with long nonlinear interaction lengths, consequently resulting in the generation of single-frequency or narrowband output [83]. Given these limitations, the generation of broadband radiation using cw OPOs has not been extensively explored previously.

In this chapter, we demonstrate a cw OPO that can provide broadband radiation in the mid-IR at multiwatt power level, with excellent beam quality, and in a compact and practical design using a fiber laser pump source. We demonstrate that despite the limitations of low nonlinear gain in the cw regime, by suitably exploiting the extended phase-matching bandwidth in MgO-doped periodically-poled $LiNbO_3$ (MgO:PPLN), long interaction lengths can be deployed in the presence of a broadband pump to provide broadband mid-IR output at multiwatt power level and with high extraction efficiency from cw OPOs.

For the generation of broadband output, we deploy a singly-resonant oscillator (SRO), with only the signal wave resonant in the optical cavity and a single-pass idler. This is the optimum configuration for delivering the highest output power from cw OPOs [94]. More importantly, in the context of the present work, since the signal frequency in a SRO is constrained to an axial mode of the optical cavity, any frequency spread in the pump will be directly transferred to the non-resonant idler in order to maintain energy conservation, so that the use of broadband pump can

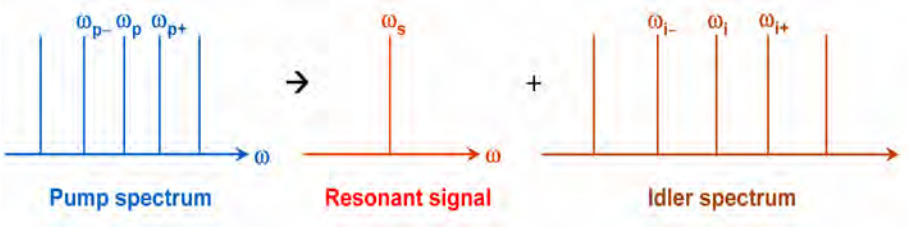

Figure 5.1: Broadband pumping of a cw SRO generating broadband idler.

lead to broadband idler output, as depicted in Fig. 5.1.

5.2 Extended phasematching bandwidth in MgO:PPLN

The practical generation of broadband output will require the attainment of appreciable gains, which can only be achieved by overcoming the limitations of narrow phase-matching bandwidths imposed by the need for long interaction lengths under cw pumping. The generation of broadband radiation in a SRO, under conditions of energy conservation, also requires phase-matching of individual spectral components of a broadband pump to the corresponding component in the idler spectrum for the resonant single-frequency signal. This condition would be satisfied if the phase-mismatch,

$$\triangle k = k_p - k_s - k_i \tag{5.1}$$

where k_p, k_s, k_i are propagation constants at pump, signal and idler, respectively, exhibits a negligible variation with changes in the pump wavelength [47, 91]. The phase-mismatch can be further expanded around the central pump wavelength, λ_0, as

$$\triangle k = [\triangle k]_{\lambda=\lambda_0} + \left[\frac{\partial(\triangle k)}{\partial\lambda}\right]_{\lambda=\lambda_0} + \frac{1}{2}\left[\frac{\partial^2(\triangle k)}{\partial\lambda^2}\right]_{\lambda=\lambda_0} (\triangle k)^2 + ... \tag{5.2}$$

The first-term on the right hand side of equation 5.2 can be made zero by choosing an appropriate poling period for the grating, Λ, so as to achieve quasi-phase-matching at λ_0 [94]. In this situation, the spectral width of the pump (around λ_0) that could contribute to efficient generation of signal and idler, also known as the pump

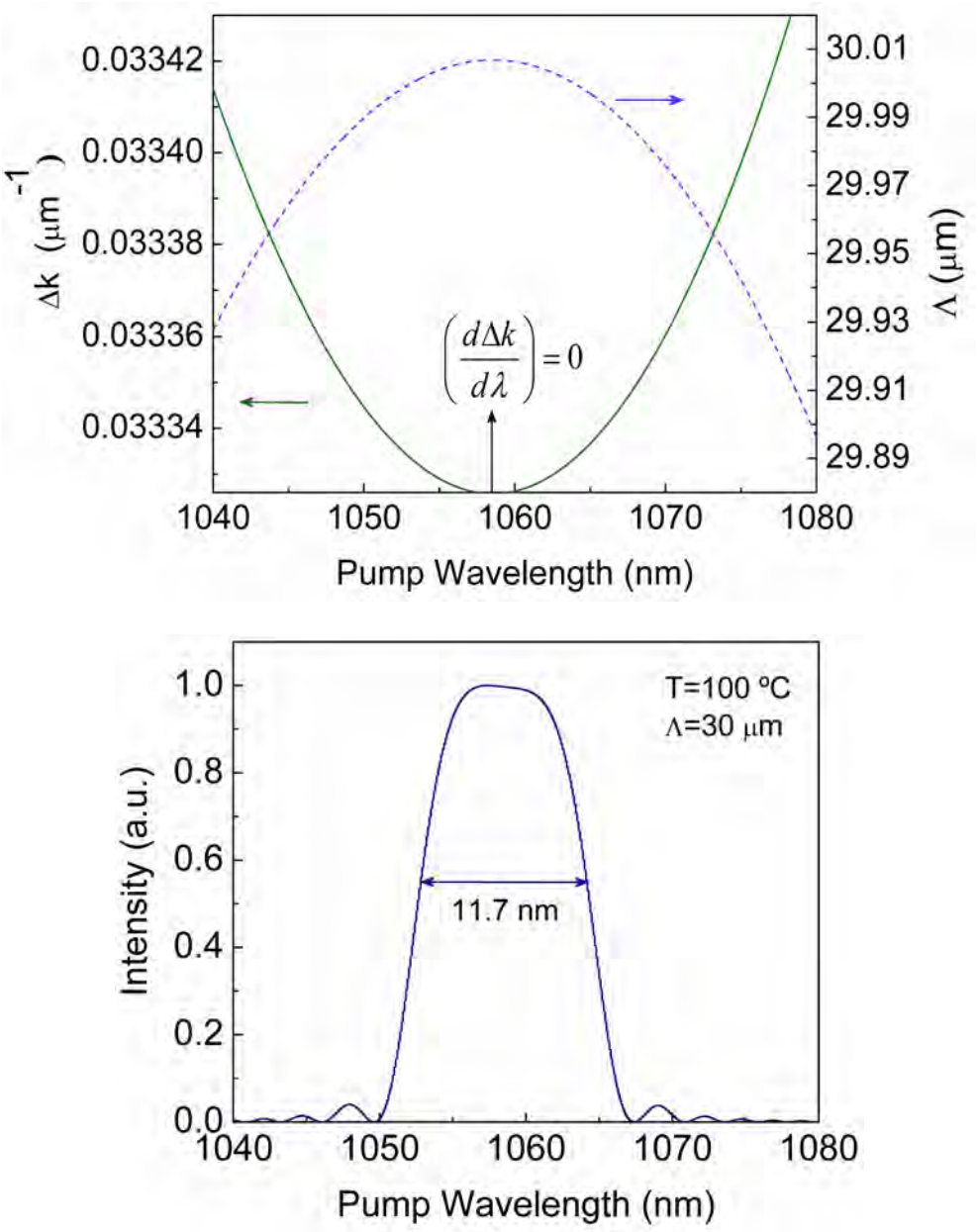

Figure 5.2: (a) Variation of phase-mismatch and corresponding grating period (Λ) required as a function of pump wavelength at T=100 °C. (b) Normalized parametric gain as a function of pump wavelength for a 50-mm-long MgO:PPLN crystal (Λ= 30 μm).

acceptance bandwidth, is limited by the second term, also referred to as the group-velocity-mismatch (GVM) term. Typically, the pump acceptance bandwidth for near- and mid-IR parametric generation in commonly used nonlinear materials is <1 nm for interaction lengths of l∼1 cm. However, in some crystals, due to strong interplay between the dispersion properties of interacting waves, the GVM term vanishes in certain spectral regions [91]. Under this condition, the pump acceptance bandwidth ($\triangle\lambda_p$) is essentially determined by the much smaller third term in the expansion of $\triangle k$ (equation 5.2), namely

$$\triangle k = 2(5.57/l)^{\frac{1}{2}} \left[\frac{\partial^2(\triangle k)}{\partial \lambda^2} \mid_{\lambda=\lambda_0} \right]^{-\frac{1}{2}} \tag{5.3}$$

Moreover, in this case, the pump acceptance bandwidth exhibits a weaker dependence on interaction length ($\triangle\lambda_p \propto l^{-\frac{1}{2}}$) compared to when the second term in equation 5.2 is finite ($\triangle\lambda_p \propto l^{-1}$). In MgO:PPLN, one can also identify such a condition. Figure 5.2(a) shows the variation of phase-mismatch, $\triangle k$, in MgO:PPLN with pump wavelength near the technologically important wavelength of 1064 nm.

The calculation is performed by directly evaluating $\triangle k$ (equation 5.1) in terms of pump wavelength for a fixed signal frequency and varying pump and idler, at T=100 °C, with all waves polarized along the optical z-axis ($e \rightarrow ee$) and propagating along the x-axis, using the relevant Sellmeier equations [65]. It is evident that close to a pump wavelength of 1059 nm, MgO:PPLN exhibits negligible variation in $\triangle k$ with wavelength. Also shown in Fig. 5.2(a) is the corresponding poling period ($\Lambda = 2\pi/\triangle k$), from which the required grating period for achieving $\triangle k = 0$ and $(\partial(\triangle k)/\partial\lambda) = 0$ is found to be ∼30 μm. Thus, if we choose a 50 mm crystal with Λ=30 μm at T=100 °C, the parametric gain curve centered at a pump wavelength of 1059 nm, calculated from the variation of $\triangle k$ in Fig. 5.2(a), results in a pump acceptance bandwidth (for low pump powers) of 104.3 cm-1 (11.7 nm FWHM), as shown in Fig. 5.2(b). This can be further verified by using equation 5.3, from which

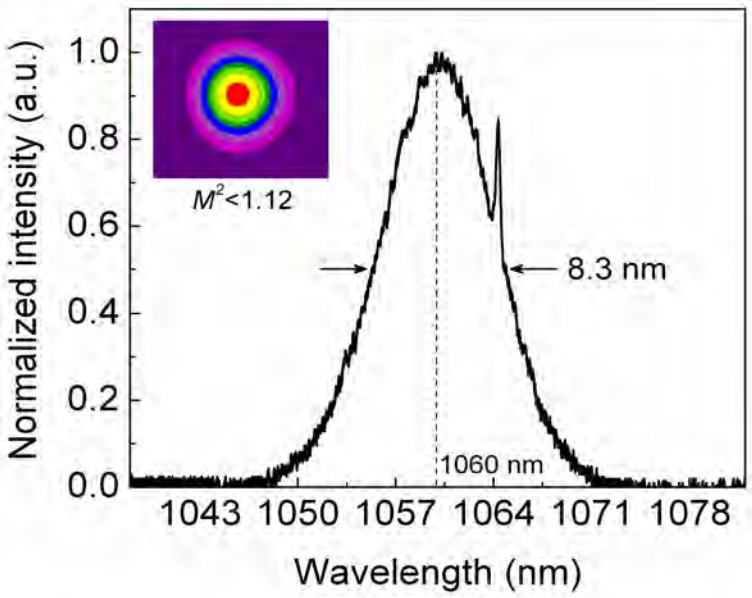

Figure 5.3: Broadband pump laser spectrum. Inset: Beam profile of the pump laser .

the pump acceptance bandwidth is calculated to be 103.9 cm^{-1} (11.65 nm FWHM), consistent with the value of 104.3 cm^{-1} (11.7 nm) obtained from the parametric gain curve in Fig. 5.2(b), calculated from equation 5.1.

5.3 Experimental setup

For the implementation of broadband cw SRO, we deploy a cw Yb fiber laser (IPG Photonics, centre wavelength ∼1060 nm), providing broadband radiation of $\triangle\nu = 73.9cm^{-1}$($\triangle\lambda$=8.3 nm), as shown in Fig. 5.3, with a maximum power of 28 W in a linearly polarized beam with good spatial quality (M^2<1.12).

The experimental setup is similar to our earlier reports [34], except for the use of a broadband pump, and is shown in Fig. 5.4. In order to exploit the extended phase-matching bandwidth of MgO:PPLN, we choose a 50 mm crystal with a grating period of 30 μm at an operating temperature of T=100±0.1 °C. The crystal is anti-reflection coated for the pump, signal and idler. The SRO cavity is a ring, comprising two concave mirrors (r=150 mm) and two plane reflectors. All mirrors have high

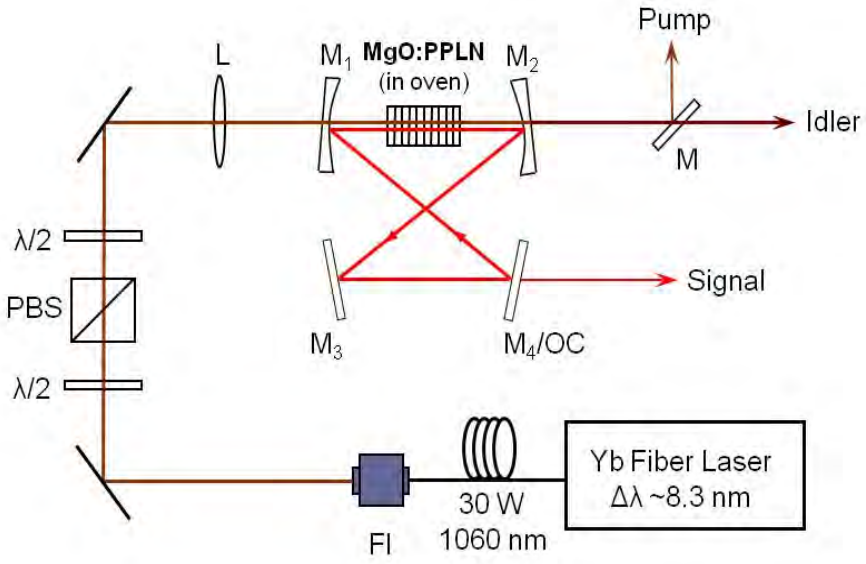

Figure 5.4: Experimental setup of the broadband pumped cw SRO.

reflectivity (>99.95%) over 1.3–2.0 μm and high transmission at pump (>90%) and idler (>85%). The pump is focused to a beam waist of ∼63 μm (l/b∼1) and the ring cavity provides a signal beam waist of ∼76 μm at 1523 nm in the crystal. The total optical length of the cavity is 941 mm.

5.4 Results and discussion

In Fig. 5.5(a), we show the measured spectrum of the fiber pump laser at the maximum available power relative to the parametric gain curve for the 50 mm MgO:PPLN crystal (T=100 °C, Λ=30 μm). The laser exhibits a bandwidth of ∼73.9 cm^{-1}(8.3 nm) at a centre wavelength of 1060 nm, with a large fraction of the spectrum lying within the pump acceptance bandwidth of the crystal. It is thus to be expected that a substantial portion of the pump spectrum could be utilized for efficient conversion to broadband mid-IR idler output. This is confirmed by the measured spectrum of the depleted pump, shown in Fig. 5.5(b), where it can be seen that about ∼63.5 cm^{-1}(7 nm) of the input pump bandwidth undergoes discernable depletion in the

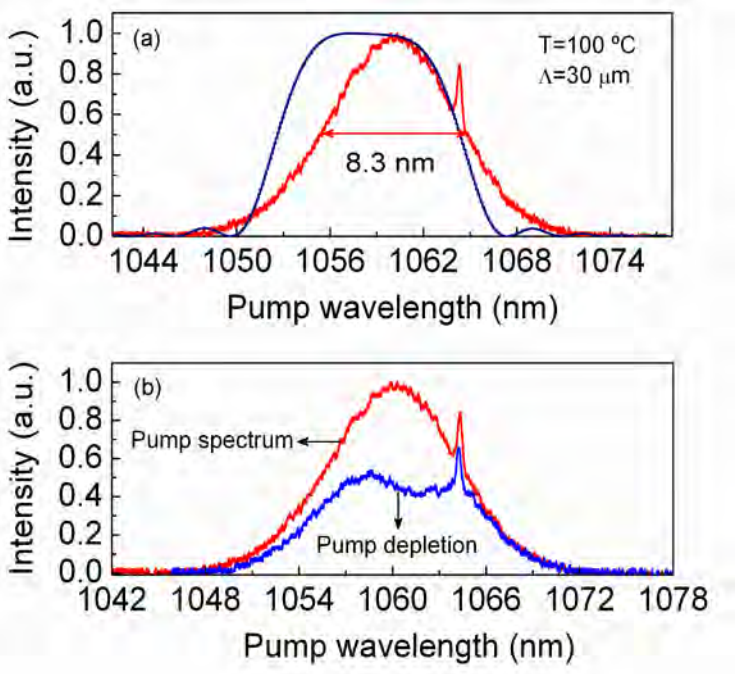

Figure 5.5: (a) Input pump spectrum and the calculated pump acceptance bandwidth for the 50 mm MgO:PPLN crystal, (b) Input and depleted pump spectra for the SRO.

SRO cavity.

It is to be noted that the resonant signal (λ_s∼1523 nm) exhibits a narrow linewidth due to high finesse of the SRO cavity ($\triangle\nu$∼6 MHz). Using the depleted pump spectrum, Fig. 5.5(b), and single-frequency signal, the reconstructed idler spectrum exhibits a bandwidth of ∼ 63.7 cm^{-1} (∼76 nm) FWHM at the central idler wavelength of λ_i∼3454 nm, as shown in Fig. 5.6.

Figure 5.7 shows the measured output power in the broadband idler as a function of pump power. We found the threshold for broadband SRO to be ∼5.8 W, and for a pump power of 25.5 W at the input to the crystal, the SRO generated 5.3 W of broadband mid-IR power at 20.8% extraction efficiency. The pump depletion was 80.6% at the maximum pump power. In order to maximize the total power extraction and reduce thermal load on the crystal, we also employed partial outcoupling of the resonant signal [77] by replacing one of the SRO plane mirrors with

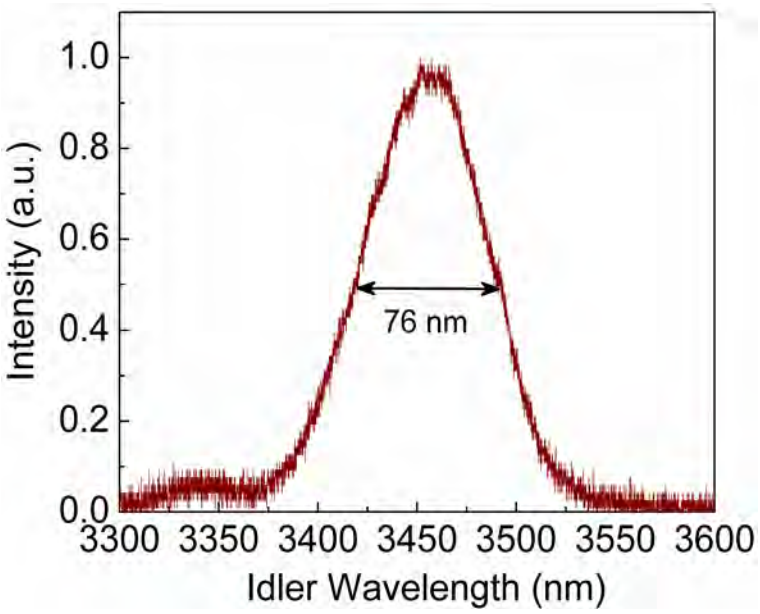

Figure 5.6: Reconstructed idler output spectrum.

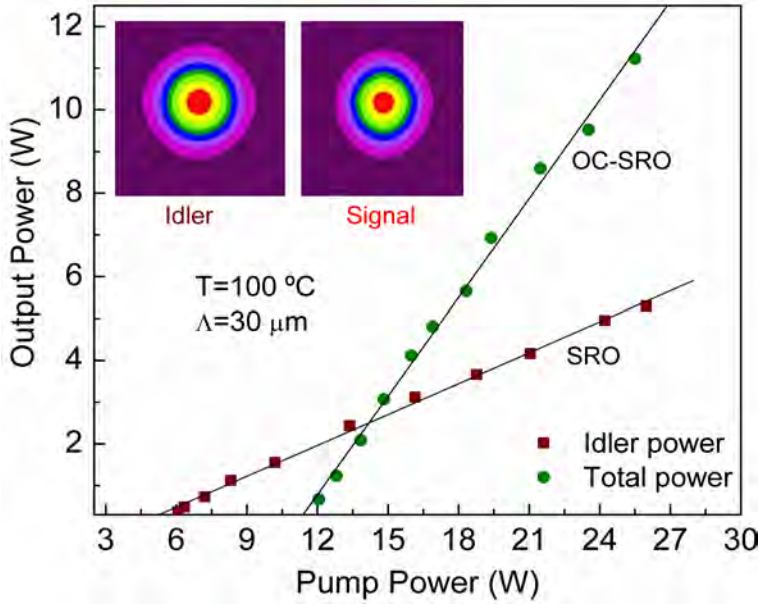

Figure 5.7: Variation of total extracted power as a function of pump power for MgO:PPLN SRO and OC-SRO. Inset: Spatial beam profile of the extracted signal and idler from the OC-SRO.

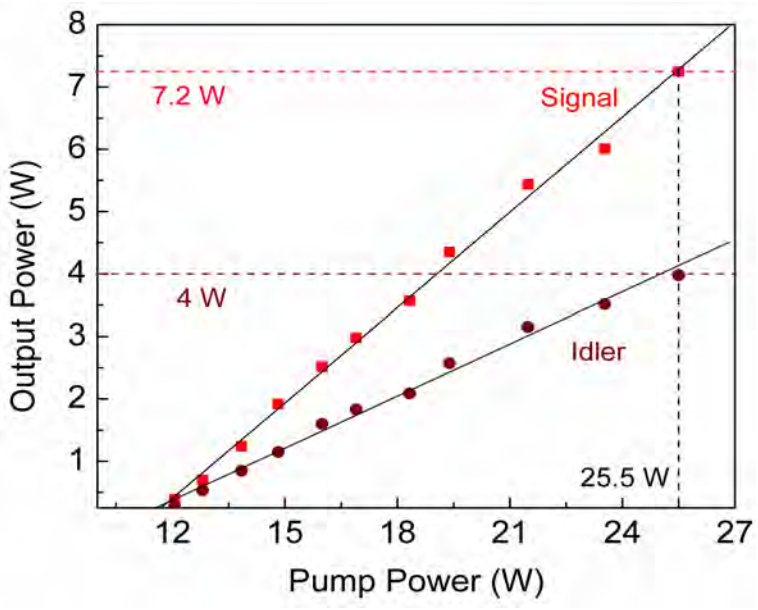

Figure 5.8: Variation of extracted signal and idler power as a function of pump power from MgO:PPLN OC-SRO.

an output coupler (OC) of ∼3.5% transmission (un-optimized) at λ_s∼1523 nm. From Fig. 5.7, it is evident that the OC-SRO threshold increases to 12.1 W. However, the maximum total extracted power (signal plus idler) is now 11.2 W for 25.5 W of pump power, representing an extraction efficiency of 44%. The variation of the extracted signal and idler power in the OC-SRO configuration is shown Fig. 5.8. Under this condition, the pump depletion was 73.3%. The far-field energy distribution of the signal and idler beams at the maximum pump power, measured at a distance >1 m from the OC-SRO output, is shown in the inset of Fig. 5.7. We also measured the M^2 factors, resulting in values of M_x^2∼1.16 and M_y^2∼1.10 for the signal andM_x^2∼1.50 and M_y^2∼1.47 for the idler, confirming Gaussian nature of the output beams.

5.5 Conclusions

In this chapter, we have demonstrated efficient generation of broadband, multiwatt mid-IR radiation from a cw-SRO using a broadband cw fiber laser by exploiting the extended phase-matching characteristics of MgO:PPLN. Further, our investigations

reveal that a 50 mm crystal with $\Lambda = 29\ \mu m$ at room temperature (T=25 °C) exhibits a pump acceptance bandwidth of 10.6 nm centered at 1030 nm, that could result in the generation of idler radiation across 120 nm band centered close to 3560 nm. Our calculations based on equation 5.3 also confirm that the use of longer MgO:PPLN crystals (up to 80 mm) will permit the generation of higher broadband mid-IR powers without significant reduction in pump acceptance bandwidth, due to the weak dependence of the phase-matching bandwidth on interaction length.

6 Interferometric variable output coupling of Optical Oscillators

This chapter constitutes the following publication:

1. *Interferometric output coupling of ring optical oscillators*
   S. Chaitanya Kumar, A. Esteban-Martin, and M. Ebrahim-Zadeh
   Optics Letters **36**, 1068–1070 (2011).

6.1 Motivation

Since the invention of the laser in 1960, the conventional technique for maximizing output power from laser oscillators has relied on the use of a partially transmitting mirror as an output coupler. While this technique has been effective and universally deployed in all optical oscillators, absolute maximization of output power is generally impossible, because of the discrete value of mirror transmission. Moreover, optimization of output power requires trial of various output couplers with different transmission values – an empirical approach, which can be time consuming and costly [34]. Furthermore, new mirrors of different transmission values are required when variations in operating conditions, such as pumping level, alter the optimum value of output coupling.

Recently, a new method for absolute optimization of output power from optical oscillators based on the use of an antiresonant ring (ARR) interferometer as an output coupler was demonstrated in the context of a synchronously pumped femtosecond

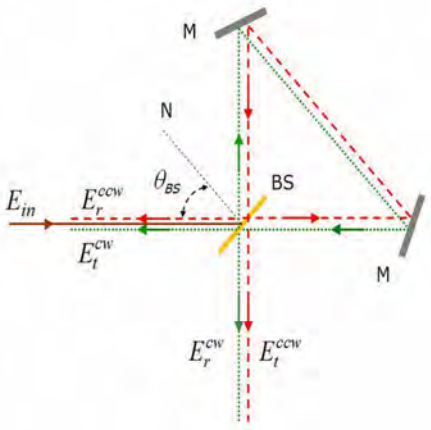

Figure 6.1: Antiresonant ring interferometer.

optical parametric oscillator (OPO) [95]. Basically, the ARR consists of a beamsplitter (BS) with a transmittance, T, and reflectance, R, and a pair of high-reflectivity mirrors, which form the ring, as shown in Fig. 6.1. The input optical field, E_{in}, incident at angle θ_{BS} on the beamsplitter is separated into the clockwise (dotted line) and counterclockwise (dashed line) beams. After propagation inside the ring and transmission or reflection by the beam splitter again, the new pairs of fields, (E_r^{ccw}, E_t^{cw}) and (E_t^{ccw}, E_r^{cw}), interfere, giving rise to the reflected, $E_r = E_r^{ccw} + E_t^{cw}$, and transmitted, $E_t = E_t^{ccw} + E_r^{cw}$, output fields. Given the transmittance, T, and reflectance, R, the power reflected back is given by $R_{ARR} = 4RT$, while the power transmitted out of the ring is given by $T_{ARR} = |R - T|^2$, implying that the reflected fields interfere in phase, whereas the transmitted fields are of opposite phase. This simple, yet powerful, technique operates over a wide wavelength range, is inherently stable, and permits arbitrary adjustment of output coupling with a simple setup by simply varying the $T : R$ ratio of the beamsplitter in the interferometer through changes in the angle of incidence, θ_{BS}. Moreover, the ARR can be re-adjusted when variations in operating conditions, such as pumping level, alter the optimum value of output coupling. We reported the first realization of this concept in a femtosecond OPO [95]. However, the technique was proposed only for standing-wave cavities by

operating the ARR interferometer as a retro-mirror with variable transmission, thus precluding the use of the concept in unidirectional ring oscillators. As such, the exploitation of this concept in ring oscillators could not be considered a clear possibility. On the other hand, the deployment of ring resonators can offer many advantages, for example in the attainment of single-frequency operation in laser oscillators, in nonlinear resonators including OPOs, where the round-trip cavity loss can be reduced by half while maintaining the same single-pass gain, or in internal nonlinear frequency conversion experiments when unidirectional output is desired. Moreover, the implementation of the ARR in ring cavities may well extend all applications suggested in the laser context [96, 97], including cavity dumping, Q-switching, mode-locking, nonlinear spectroscopy, and fiber-optics.

In this chapter, we demonstrate, for the first time, the use of this novel concept in a ring resonator by integrating an ARR interferometer inside a picosecond OPO based on MgO:PPLN to optimize the output coupling at different pumping levels, resulting in maximum output power for an optimum output coupling of ∼42.8% (θ_{BS}=35°), generating more than 5 W of signal power at 1529 nm for a pump power of 14 W. There are two key factors in the realization of the ARR concept in a ring cavity. On one hand, the use of a folded ring cavity [98] provides an almost-linear cavity arm inside the main ring. On the other hand, the flexibility of the ARR to slightly misalign its feedback in a controlled manner enables us to close the folded ring.

6.2 Experimental setup

A schematic of the experimental setup is shown in Fig. 6.2. The pump laser is a Yb fiber laser (Fianium, FP1060-20) delivering ∼20.8 ps pulses at 81.1 MHz repetition-rate at 1064 nm with a double-peak spectral bandwidth of 1.38 nm (FWHM). The nonlinear crystal is a 50-mm-long, 8.2-mm-wide, 1-mm-thick 5%-doped MgO:PPLN crystal, which contains seven equally spaced grating periods ranging from Λ=28.5 to

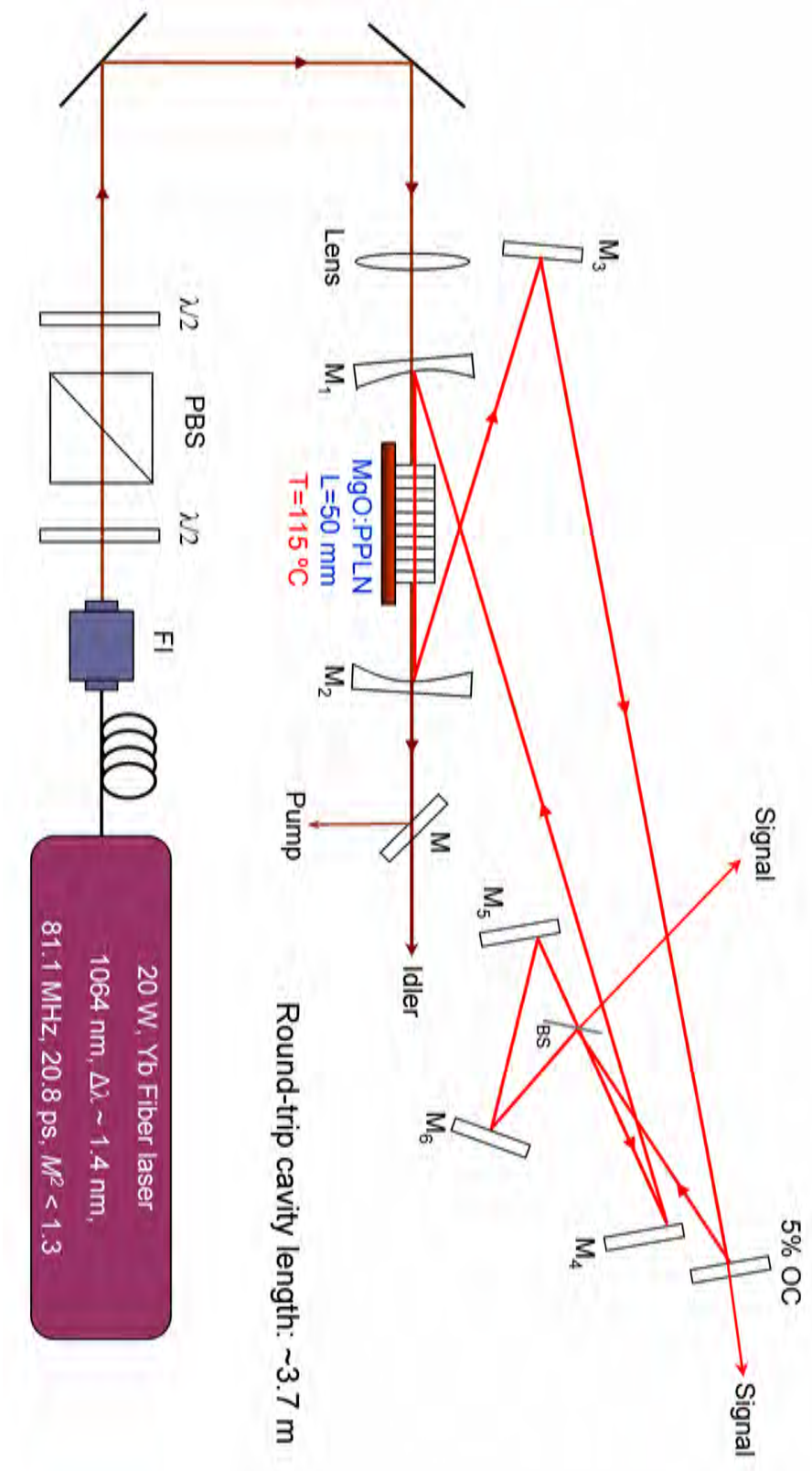

Figure 6.2: Configuration of ARR output-coupled synchronously-pumped picosecond OPO in a ring cavity.

31.5 μm, and is housed in an oven with a temperature stability of $\pm$0.1 °C, as used previously in standing-wave cavity [99]. The pump beam is focused to a waist radius of $w_0 \sim$45 μm at the center of the MgO:PPLN crystal, corresponding to a confocal focusing parameter $\xi \sim$1.94. In this work, the OPO is configured in a folded ring cavity, incorporating an ARR in the folded arm. The OPO consists of two curved mirrors, M_1 and M_2 (r=200 mm, CaF_2 substrate), and four plane mirrors, M_3- M_6. All mirrors are highly reflecting (R>99%) for the signal over 1.3-2.2 μm and highly transmitting for the pump (T>90%) at 1064 nm and idler (T>87%) over 2.2-4 μm, thus ensuring singly resonant oscillation. A conventional plane output coupler (OC) with partial transmission (T$\sim$5%) over the signal wavelength range is used to extract the signal power from the OPO and a dichroic mirror, M, separates the generated idler from the pump. A beamsplitter and the two plane mirrors M_5, M_6 constitute the ARR interferometric output coupler. The total optical length of the OPO ring cavity, including the 29-cm-long ARR, is $\sim$370 cm, corresponding to a repetition rate of 81.1 MHz, ensuring synchronization with the pump laser.

6.3 Variable output coupling

In order to characterize the OPO, we tuned the signal to 1529 nm by changing the temperature of the crystal to 115 °C for a grating period of 30 μm. The corresponding idler wavelength is 3498 nm. Initially, we characterized the ARR interferometer outside the folded ring-cavity OPO at 1529 nm to estimate the output coupling from ARR as a function of the beamsplitter angle, θ_{BS}, using the conventional 5% OC, as shown in Fig. 6.3. As can be seen from Fig. 6.3, the transmission from the ARR can be continuously varied from 20% to very high values up to >70% by simply changing the angle of the beamsplitter from 15° to 55°. After the external characterization of the ARR interferometer, we deployed it inside the folded ring cavity and performed the characterization of the OPO at a signal wavelength of 1529 nm, corresponding to an idler wavelength of 3498 nm. The signal output is extracted from both the

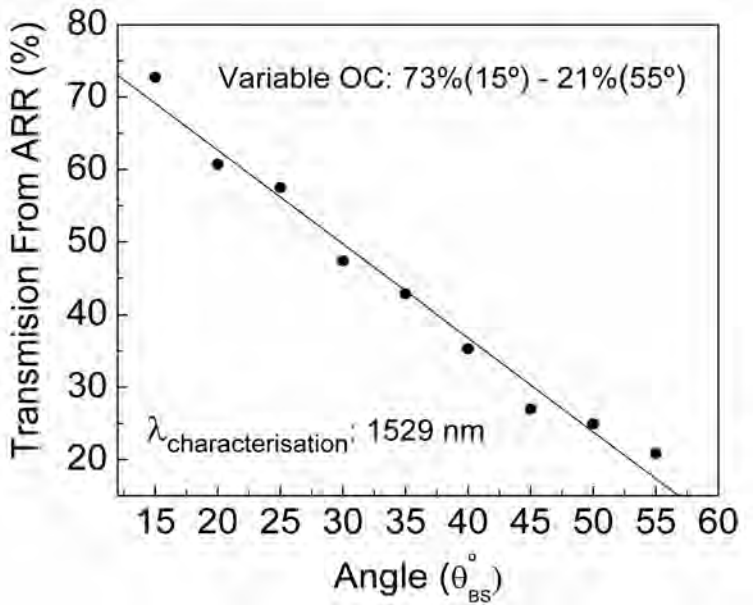

Figure 6.3: Transmission of the ARR as function of the beam splitter angle.

conventional OC and from the ARR. Signal output from the 5% OC is used as a reference, whereas ARR provides the variable output coupling to be studied.

6.3.1 Output coupling optimization at different pumping levels

We performed optimization of signal output power at two different pump powers. Figure 6.4(a) shows the signal output power optimization as a function of output coupling from the ARR at a pump power of 3.5 W. For a fixed pump power, the signal power from ARR as well as the conventional OC is recorded by changing the angle of the beamsplitter. As the output coupling is varied from 20.8% to 72.7%, the extracted signal power increases sharply from 1.28 W up to 1.67 W at an optimum coupling of 27%, above which it drops down to 1.05 W at 72.7% output coupling. On the other hand, the signal power from the conventional 5% output coupler constantly decreases from 121 mW to 49 mW, validating the improvement in the extracted signal power from ARR is due to output coupling optimization. The corresponding idler power varies from 0.68 W at 20.8% output coupling to 0.45 W at 72.7%, with a maximum power of 0.82 W at 27% output coupling, as shown in Fig. 6.4(b). It

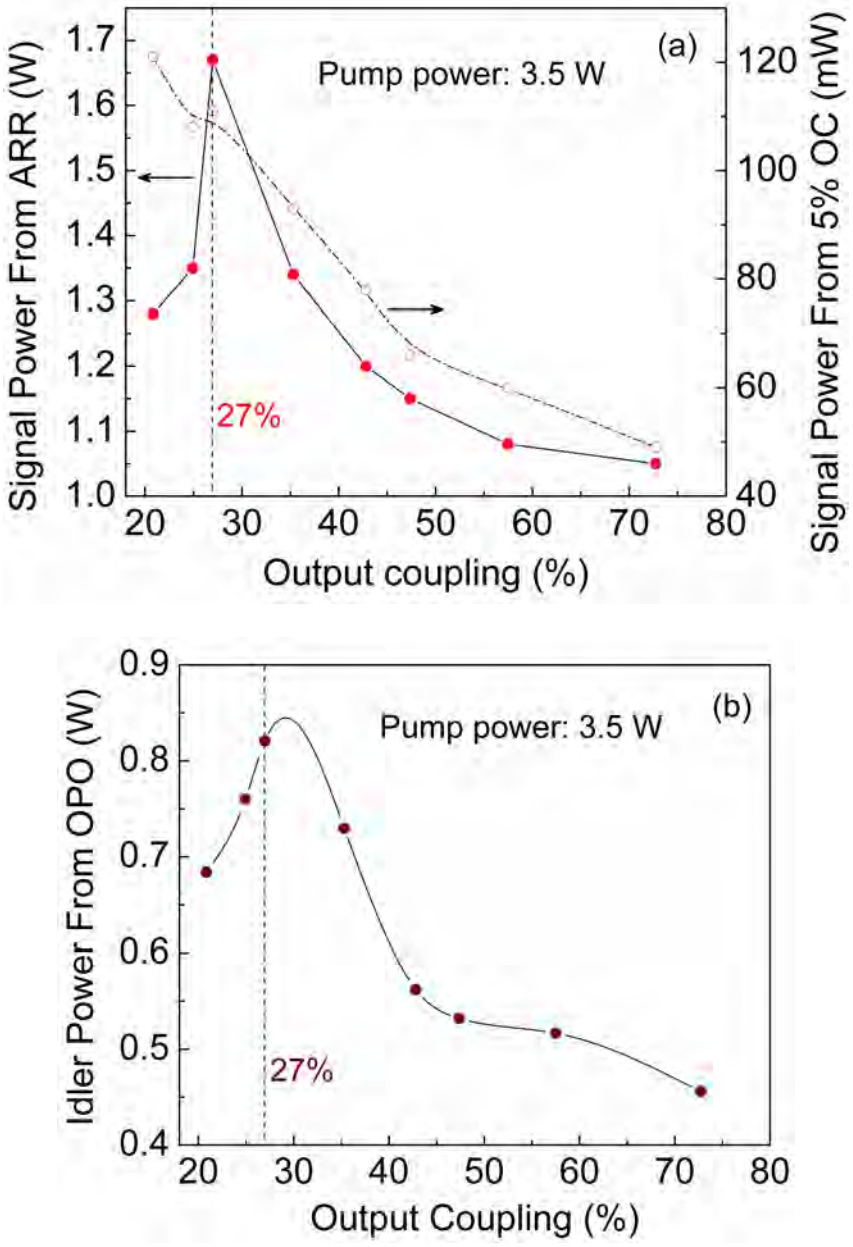

Figure 6.4: Variation of the (a) signal and (b) idler output power from the ARR as a function of output coupling at 3.5 W of pump power.

is interesting to note that at lower pump power, the optimum output coupling to maximize both the signal and idler is the same. Also, the sharp rise and fall in the signal output power with the output coupling shows that the OPO is more sensitive to losses at low pump power.

Similar measurements at a higher pump power of 13.5 W resulted in the variation of the signal power from 4.23 W at 20.8% to a maximum of 5.1 W at an optimum signal output coupling of 42.8%, above which it decreases to 4.76 W at 72.7 %, while the signal power from the conventional 5% output coupler constantly decreases from 344 mW at 20.8% output coupling to 228 mW at 72.7%, as shown in Fig. 6.5(a). The corresponding idler power, shown in Fig. 6.5(b), varies from 1.6W to 1.86 W with a maximum at 2.25 W for a signal output coupling value of 57.5%. It is to be noted that, unlike at low pump power, the OPO is less sensitive to losses at higher pump power, resulting in a broad bandwidth of output coupling.

The variation of the optimum output coupling with the pumping level is shown in Fig. 6.6. Although both signal and idler power are maximized at the same value of 27% output coupling for low pump power, it differs significantly for high pump power. The signal power is maximized at 42.8% and the idler power is maximized at 57.5% output coupling for the same pump power of 13.5%. Hence, ARR interferometer is a powerful tool to optimize the output coupling at different pumping levels.

6.4 Power scaling and stability

We have also studied power scaling of the ARR output-coupled OPO at the optimum output coupling of ∼42.8% (θ_{BS}=35°) for high pump powers. Figure 6.7 depicts the variation of the signal power extracted through the conventional 5% OC, and the ARR output coupler, as a function of input pump power. Also shown is the variation of the total power (signal plus idler) versus pump power at the optimum ARR output coupling. Owing to the high output coupling (∼48%), the OPO threshold is 814 mW, while the threshold with conventional 5% OC is 90 mW. However, a total signal power

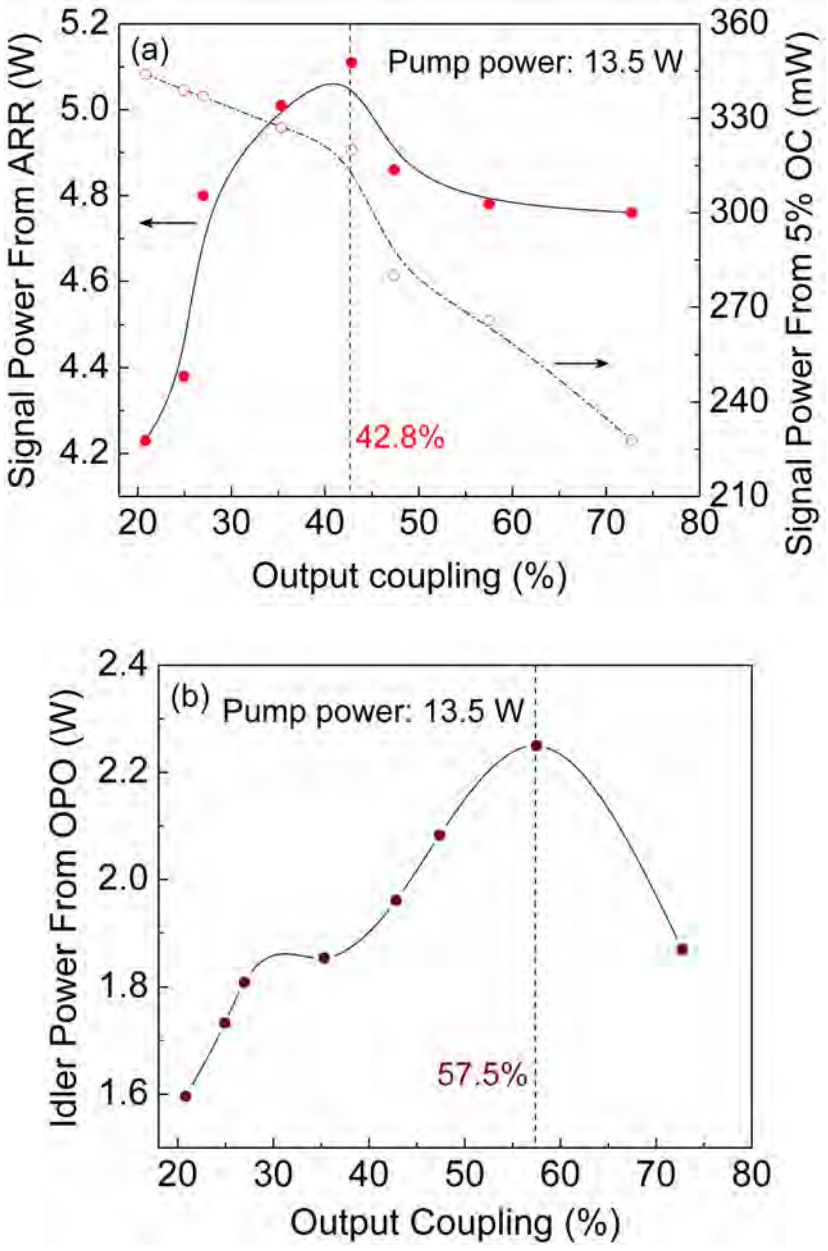

Figure 6.5: Variation of the (a) signal and (b) idler output power from the ARR as a function of output coupling at 13.5 W of pump power.

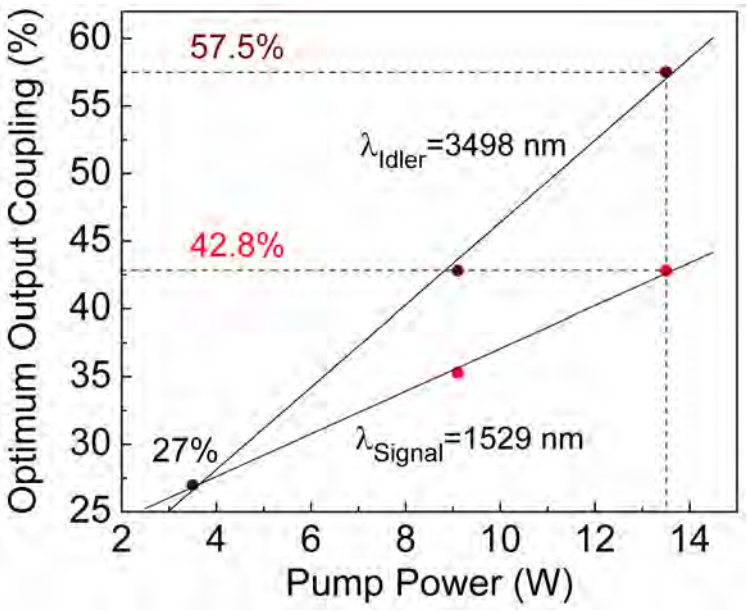

Figure 6.6: Variation of optimum output coupling as a function of pump power.

of 5.5 W (5.18 W from the ARR and 0.32 W from the OC) at 1529 nm, together with an idler power of 2.4 W at 3498 nm, resulting in a total power (signal plus idler) of ∼8 W, is extracted from the OPO for 14 W of pump power using optimum ARR output coupling. This is while using the conventional 5% OC results in a total extracted power of only 3.45 W (2.08 W signal and 1.37 W idler) for a similar pump power. Hence, the optimization of the output coupling by incorporating ARR in our OPO has resulted in >55% improvement in the total extracted power. We have also recorded a pump depletion of >60% at the optimum ARR output coupling for 14 W of pump power.

Further, we have recorded the long-term signal power stability at the optimum ARR output coupling at an extracted signal power of ∼5 W, resulting in a peak-to-peak power fluctuation of 6.1% over 16 hours, as shown in Fig. 6.8, implying a very good performance. Also shown in Fig. 6.8 is the idler long-term power stability, showing a peak-to-peak power fluctuation of 15.8% recorded at the corresponding idler wavelength of 3498 nm. Using a focusing lens and a scanning beam profiler, we measured the quality factor of the output beam from the ARR output-coupled OPO

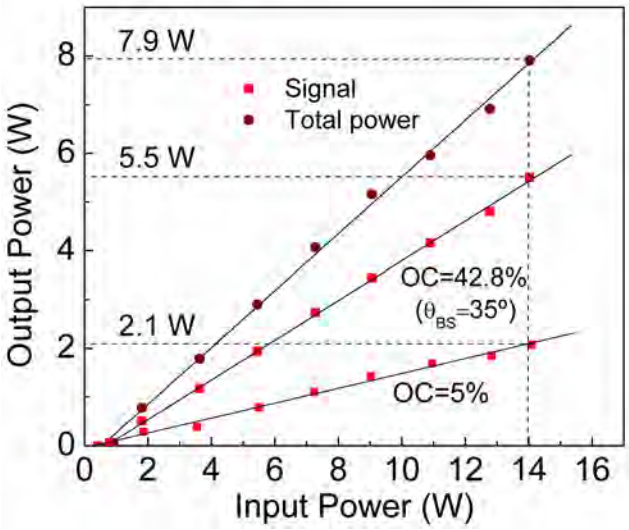

Figure 6.7: Variation of extracted signal power from the OPO using, 5% conventional OC, optimum ARR output coupling along with total power from ARR as a function of the input pump power.

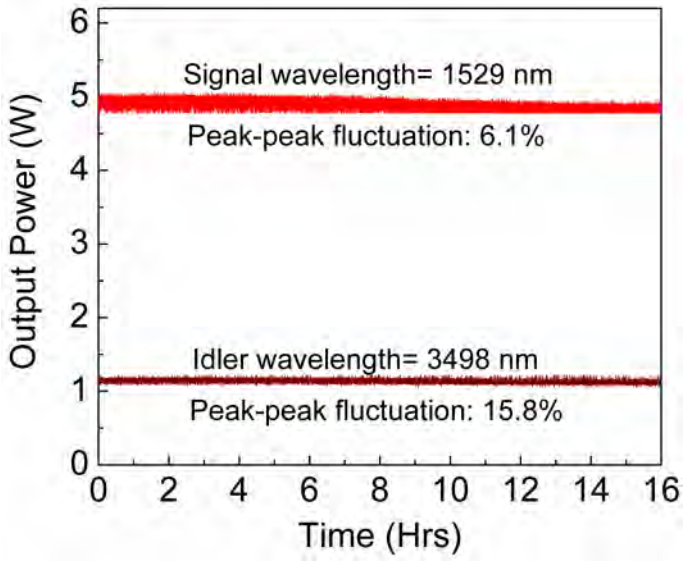

Figure 6.8: Long-term power stability of OPO signal and idler pulses extracted through the ARR output coupler.

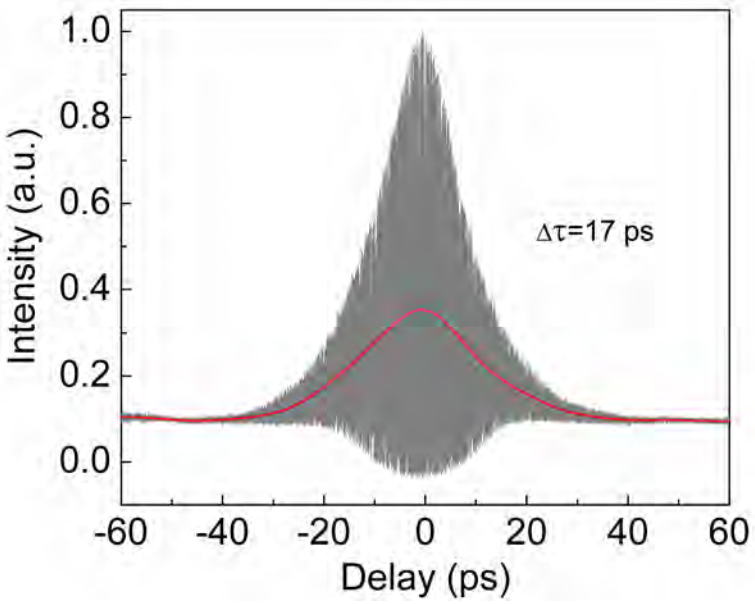

Figure 6.9: Interferometric autocorrelation of OPO signal pulses extracted trough the ARR.

to be M_x^2∼2.3 and M_y^2∼1.6 for the signal (1529 nm) and M_x^2∼1.5 and M_y^2∼1.4 for the idler (3498 nm) at full output power.

6.5 Spectral and temporal characteristics

Finally, we have also performed spectral and temporal characterization of signal pulses from the ARR output-coupled OPO. Figure 6.9 shows the typical interferometric autocorrelation, with signal pulse duration of $\Delta\tau$∼17 ps. These measurements of the signal pulses correspond to a time-bandwidth product $\Delta\upsilon\Delta\tau$∼3.05, which is ∼2.5 times lower than that of the pump pulses, indicating no degradation in the output pulse characteristics. The corresponding signal spectrum with a FWHM bandwidth of 1.4 nm, centered at 1529 nm, is shown in Fig. 6.10. These measurements are also similar to the results obtained with the same OPO in a standing-wave cavity using conventional OC [99], further validating the excellent performance of the ARR output coupling technique.

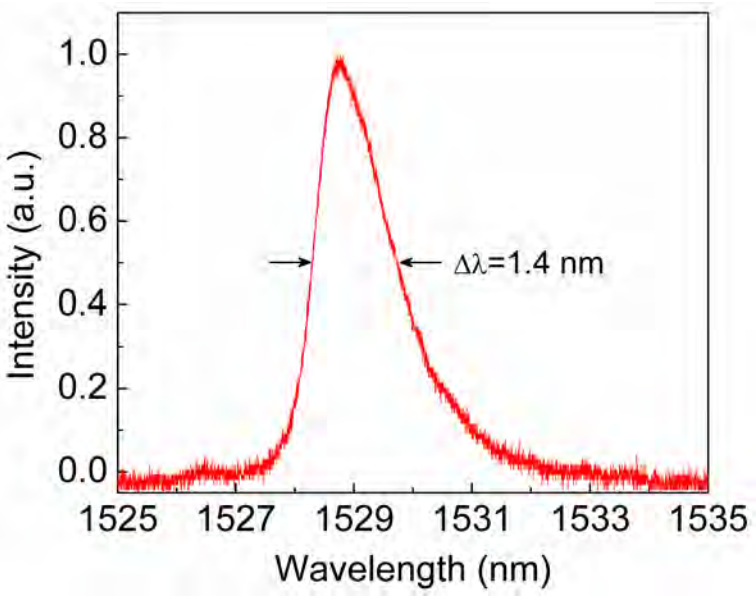

Figure 6.10: ARR output coupled OPO signal spectrum centered at 1529 nm.

6.6 Conclusions

In this chapter, we have demonstrated, for the first time, a powerful and universal, yet simple and practical technique for absolute optimization of output power from ring optical oscillators, providing broad bandwidth variable output coupling without any spatial, temporal, and spectral degradation of the output beam. The OPO generated as much as 8 W of total (signal plus idler) power at θ_{BS}=35°, corresponding to an optimum output coupling of ∼48%. The signal output has pulse duration of ∼17 ps with a spectral width of 1.4 nm centered at 1529 nm. Further, this generic technique is wavelength independent and can be implemented in any type of oscillator, opening up new avenues in the context of OPOs, as well as the wider field of laser technology.

7 High-energy, high-repetition-rate, $CdSiP_2$ OPO

This chapter constitutes the following publication:

1. *Compact, 1.5 mJ, 450 MHz, CdSiP2 picosecond optical parametric oscillator near 6.3 μm*

   S. Chaitanya Kumar, A. Agnesi, P. Dallocchio, F. Pirzio, G. Reali, K. T. Zawilski, P. G. Schunemann, and M. Ebrahim-Zadeh

   Optics Letters **36**, 3236–3238 (2011).

7.1 Motivation

The mid-infrared (mid-IR) window of the optical spectrum has a wealth of information pertaining to many molecules of importance involved in a variety of applications, from surgery [100] to explosive detection [101]. In particular, mid-IR radiation in 5900-6600 nm wavelength range, constituting the absorption bands of amide I (6000 nm), water (6100 nm) and amide II (6450 nm) are of interest for human surgery, because of the simultaneous absorption by both proteins and water. Research in the past has shown that the choice of these wavelengths minimizes the collateral damage, while maintaining an effective ablation rate of the tissue, enabling minimally invasive human surgery [1]. In the absence of conventional lasers at these wavelengths, the free electron laser has been shown to be the only source capable of delivering sufficient energy for such applications [102]. But high complexity, large size, and

high cost preclude its use in practical applications. Optical parametric oscillators (OPOs) are now well recognized as powerful and viable solid-state sources of coherent radiation, providing access to mid-IR spectral region with wide tunability. However, mid-IR OPOs, pumped at 1 μm have relied mainly on the well-established oxide-based nonlinear materials such as $LiNbO_3$, practically limiting the spectral coverage of these devices to $\sim$4 μm, imposed by the onset of absorption [1]. Alternatively, OPOs based on chalcopyrite crystals such as $AgGaSe$ and the most developed $ZnGeP_2$(ZGP) can generate mid-IR radiation up to $\sim$10 μm, but must be pumped above 1 μm to avoid two-photon and residual absorption. As a result, they are often pumped in tandem, typically by another OPO, resulting in complex architectures [1]. Hence, it is imperative to explore viable alternative materials for generation of mid-IR radiation beyond 4 μm pumped by the well-established Nd-based lasers at 1064 nm. The quest for such a nonlinear material recently led to the development of $CdSiP_2$ (CSP) [103]. Its large band gap, high optical quality, improved thermal and optical properties with high effective nonlinear coefficient ($d_{eff}$$\sim$84.5 pm/V), and noncritical phase-matching (NCPM) make it an attractive nonlinear material candidate for generating mid-IR wavelengths in the 6-6.5 μm range [104].

Earlier reports on mid-IR OPOs based on CSP pumped at 1064 nm include a low-repetition-rate (10 Hz) nanosecond oscillator with idler energies up to 0.47 mJ at 6.2 μm [105], and a 0.24 mJ, 1 kHz, sub-nanosecond OPO with idler tuning around 6.1 μm [106]. Also, mid-IR picosecond pulses near 6.4 μm with an output energy of 0.56 mJ were generated by synchronous pumping an OPO with a nonlinear mirror mode-locked Nd:YAG laser in non-collinear geometry [107]. Recently, single-pass parametric generation in CSP was also reported, pumped at 1064 nm, providing picosecond pulses with energy of 1.54 μJ at 6.2 μm at a repetition rate of 100 kHz [108].

In this chapter, we describe a compact, 450 MHz repetition rate OPO based on CSP, synchronously pumped by a master oscillator power amplifier (MOPA) system

at 1064.1 nm, generating an idler energy as high as 1.5 mJ at 6246 nm with a photon conversion efficiency of 29.5%. The OPO is tunable over 486 nm, with more than 1.2 mJ over >68% of the tuning range in good beam quality. To our knowledge, this is the first high-repetition-rate picosecond OPO based on CSP, synchronously pumped at 1064 nm in collinear geometry.

7.2 Properties of CSP

The new nonlinear crystal, CSP, for the mid-IR, was discovered only recently. CSP is a chalcopyrite semiconductor belonging to the space group $\overline{4}2m$. Its practical transparency extends from 1 to 6.5 μm. Various optical, thermal and mechanical properties in the CSP crystal are tabulated in Table 7.2. CSP is a very interesting nonlinear material because it possesses most of the attractive properties as ZGP, a crystal which is relatively matured for mid-IR generation. However, CSP is a uniaxial crystal with negative birefringence, unlike ZGP which shows positive birefringence. This feature enables noncritical phase-matching for mid-IR generation at 6 μm with maximized effective nonlinearity while pumping at 1064 nm. The possibility of pumping CSP at the well-established Nd:YAG wavelength of 1064 nm to generate mid-IR radiation as far as 6 μm is one of the most important feature of this new nonlinear material.

Phase-matching in CSP can be achieved by choosing the correct phase-matching angle. The ordinary and extraordinary refractive indices of CSP are given by the Sellmeier equations,

$$n_e^2 = 3.0811 + \frac{6.2791 \times \lambda^2}{\lambda^2 - 0.10452} - 0.0034888 \times \lambda^2 \tag{7.1}$$

$$n_o^2 = 3.4343 + \frac{5.6137 \times \lambda^2}{\lambda^2 - 0.11609} - 0.0034264 \times \lambda^2 \tag{7.2}$$

These equations were used to calculate the phase-matching conditions for Type-I

Transparency	1 – 6.5 μm
Birefringence ($n_e - n_o$)	-0.051 @ 4 μm
Bandgap	2.2 - 2.45 eV (564 – 506 nm)
Nonlinear coefficient	d_{14}=53 pm/V, d_{36}= 84.5 pm/V @ 4.56 μm
Thermal conductivity	13.6 $W/m/K$
Specific heat	446 $J/Kg/K$
Melting point	1133 ^{o}C
Thermal diffusivity	7.69 mm^2/s
Thermal expansion	-2.8 x 10-6 K^{-1} (perpendicular to c-axis) 10.2 x 10-6 K^{-1} (parallel to c-axis)
Knoop´s hardness	930 Kg/mm^2
Micro-hardness	9.3 GPa

Table 7.2: Properties of Cadmium Silicon Phosphide (CSP) nonlinear crystal.

($e \rightarrow oo$) OPO pumped at 1064 nm. The results are shown in Fig. 7.1(a) , indicating that CSP can be pumped by 1.064 μm solid state lasers to generate output beyond 6 μm in a single OPO stage without the need for any tandem OPO stages. Further, CSP also has a small, but finite thermal dependence of the refractive indices, enabling temperature tuning. Thermal sensitivity of refractive indices of CSP is given by the temperature dependent Sellmeier equation,

$$n^2 = A + \frac{B \times \lambda^2}{\lambda^2 - D} - C \times \lambda^2 \tag{7.3}$$

where

	n_o	n_e
A	$3.0449 + 1.214 \times 10^{-4} T(K)$	$3.3978 + 1.224 \times 10^{-4} T(K)$
B	$6.1164 + 5.459 \times 10^{-4} T(K)$	$5.4297 + 6.174 \times 10^{-4} T(K)$
C	0.0034888	0.0034888
B	0.10452	0.11609

Figure 7.1(b) shows the theoretical temperature tuning curves of a 1064 nm pumped CSP OPO calculated using the temperature dependent Sellmeier equation 7.3. Changing the temperature of the nonlinear crystal from 20 °C to 130 °C enables signal tuning from 1284 nm to 1270 nm, while the idler can be tuned from 6200 nm to 6551 nm. Although the calculations presented in this chapter are based on equations 7.1,7.2,7.3, investigations for accurate dispersion properties of this new nonlinear material resulted in variants of sellmeier equations which are compiled in reference [109].

7.3 Experimental design and setup

The schematic of the experimental setup is shown in Fig. 7.2. The high-energy MOPA pump laser system is seeded by a 450 MHz passively mode-locked oscillator providing 5.4 ps micro-pulses. An acousto-optic modulator selects a train of micro-pulses with 1 μs duration (macro-pulse) at a repetition rate of 20 Hz and the successive amplifier stages increase the macro-pulse energy up to 50 mJ, corresponding to an average power of 1 W. This represents a single micro-pulse energy of 0.1 mJ with a measured pulse width of 8.6 ps at a central wavelength of 1064 nm.

A number of important temporal effects have to be considered while designing an ultrafast OPO. One such effect is group velocity walkoff between the pump, signal, and idler. This can affect the temporal overlap between the pulses, thereby influencing the parametric gain and temporal characteristics of the output pulses. The effects of temporal walkoff can be estimated by evaluating the differences in the inverse group velocity between the pump, signal, and idler pulses, given by equation 2.50 and 2.51. The results of these calculations are shown in Fig. 7.3, where the magnitude of the inverse group velocity mismatch, Δv_g^{-1}, between the pump, signal, and idler in a CSP OPO is plotted as a function of the signal wavelength. The calculations are based on the Sellmeier equations 7.1 and 7.2. It is seen that the temporal walkoff between the resonated signal and pump is about 183±43 fs/mm across the tuning range with the corresponding signal-idler and pump-idler walkoff amounting

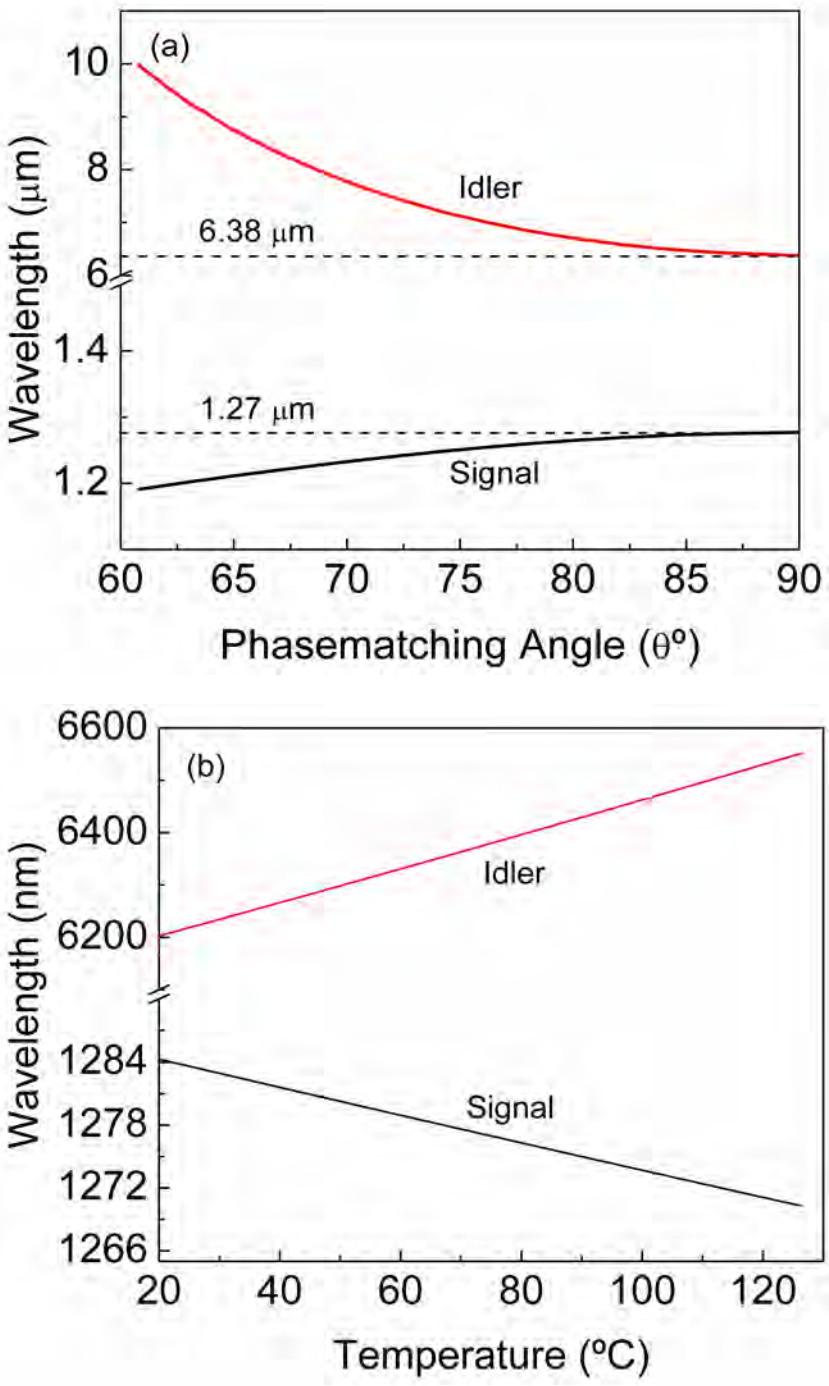

Figure 7.1: (a) Angle tuning and (b) temperature tuning curves of a 1064 nm pumped CSP OPO.

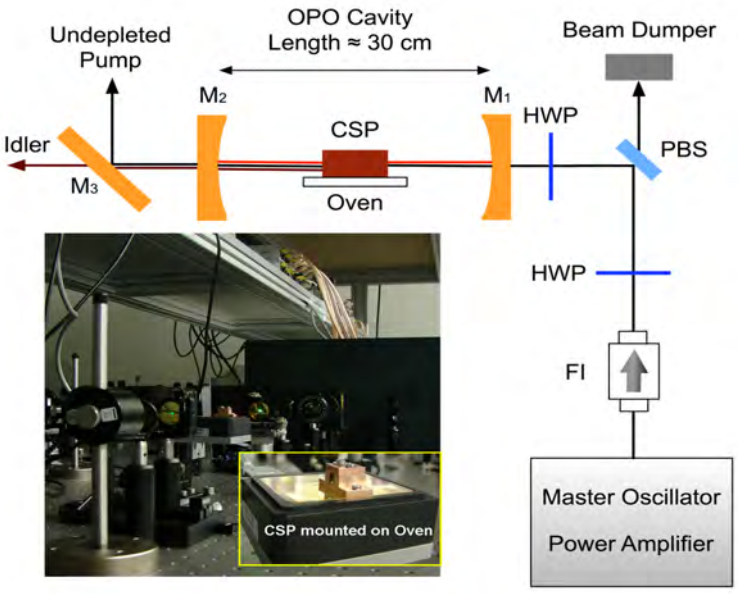

Figure 7.2: Experimental setup of synchronously pumped high energy CSP picosecond OPO Inset: Laboratory setup and CSP crystal mounted on an oven.

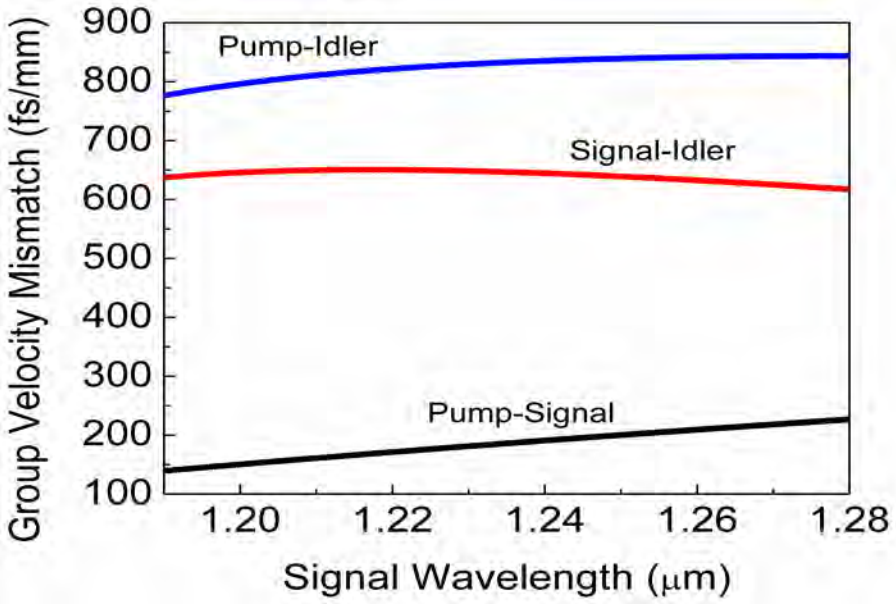

Figure 7.3: Theoretical calculations of GVM for 1064 nm pumped CSP OPO.

to 627±10 fs/mm and 810±33 fs/mm, respectively. The temporal walkoff between the pump and resonated signal is the most important parameter in determining the maximum useful interaction length. The larger value of pump-signal walkoff limit the usable crystal lengths in CSP. In the present experiment pump pulses as short as 8.6 ps can support crystal lengths upto 47 mm. This substantially long effective length in CSP is due the NCPM used in the present experiment. Moreover, the effect of group velocity walkoff is offset by larger nonlinearity of CSP, which allows higher OPO conversion efficiencies to be achieved, despite finite losses at the operating wavelengths, particularly for the pump and idler.

Another important parameter is the spectral acceptance bandwidth of the CSP crystal for the pump. The pump laser operates at a central wavelength of 1064.1 nm and has an FWHM spectral bandwidth of 0.16 nm. This is shown in Fig. 7.4, relative to the parametric gain bandwidth of 0.33 nm for 12.1-mm-long CSP crystal, estimated using the relevant Sellmeier equations [103]. The output beam from pump laser has a diameter of 2 mm and a beam quality factor of M^2∼1.1. The CSP crystal is a 12.1-mm-long, 4-mm-wide (along the c-axis), 5-mm-thick sample grown from stoichiometric melt by the horizontal gradient freeze technique [103]. It is cut at θ=90°, ϕ=45° for Type-I ($e \rightarrow oo$) interaction under NCPM and housed in an oven with temperature stability of ±0.1°C. Both crystal faces are antireflection coated with a single layer sapphire coating, providing high transmission (T>98.7%) for the pump and signal over 1064-1300 nm and T>76% for the idler over 6000-6500 nm. The residual loss at 1064.1 nm is estimated from the measured transmission of the crystal. As depicted in Fig. 7.5, we observed a drop in the transmission of CSP crystal with increasing pump intensity, showing a nonlinear behavior. Using a simple two-photon absorption model, we fitted the measured data for linear (α) and two photon (β) absorption coefficients, resulting in a value of α=0.075 cm^{-1}, β=2.4 cm/GW for extraordinary (e) and α=0.15 cm^{-1}, β=2.6 cm/GW for ordinary (o) polarizations. These values indicate the improved quality of this crystal as compared to the earlier

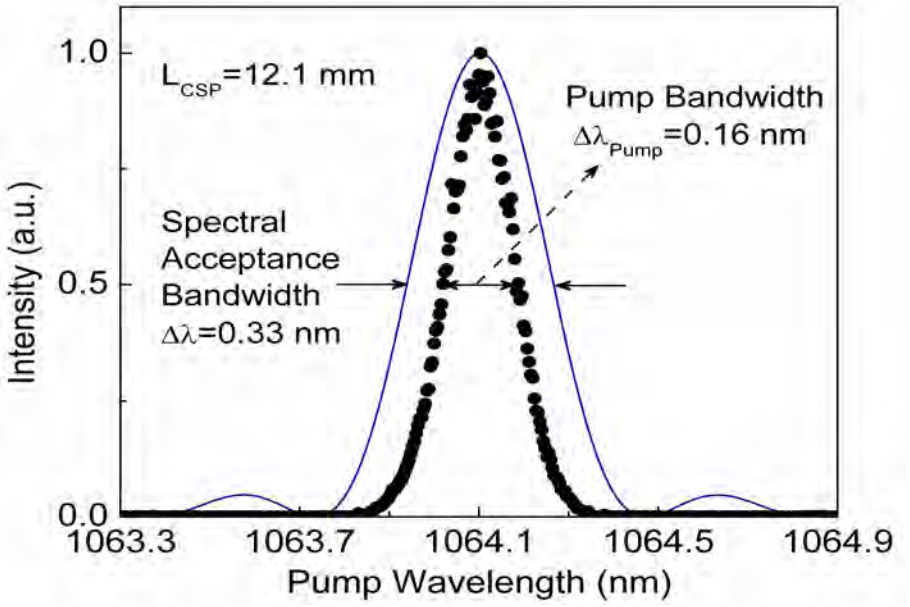

Figure 7.4: Pump laser spectrum relative to parametric gain bandwidth for 12.1-mm-long CSP crystal.

samples [105, 106, 107, 108]. Further, using this data, we have estimated the energy band gap (E_g) resulting in the values of 2.08 eV (e) and 2.06 eV (o), confirming the large band gap of CSP [110]. The OPO is configured as a singly-resonant oscillator in a compact linear standing wave cavity comprising two curved mirrors, M_1 and M_2, with radius of curvature r=3 m (ZnSe substrate). Both mirrors are highly reflecting (R>99%) for signal over 1200-1400 nm, and highly transmitting at 1064 nm (T>97%) and for the idler over 5500-7500 nm (T>98%). The pump beam has a waist radius of w_0~1.5 mm after the input mirror (M_1) to avoid any damage, while using the maximum aperture of the crystal. A dichroic mirror, M_3, highly reflecting (R>99%) at 1064 nm and highly transmitting (T>95%) for idler, separates the generated idler from the undepleted pump. In the measurements of energy and efficiency, all the data were corrected for transmission and reflection coating losses. The total round-trip optical length of the cavity, including the CSP crystal, is 666 mm, corresponding to a 450 MHz repetition rate, ensuring the synchronization with the pump laser.

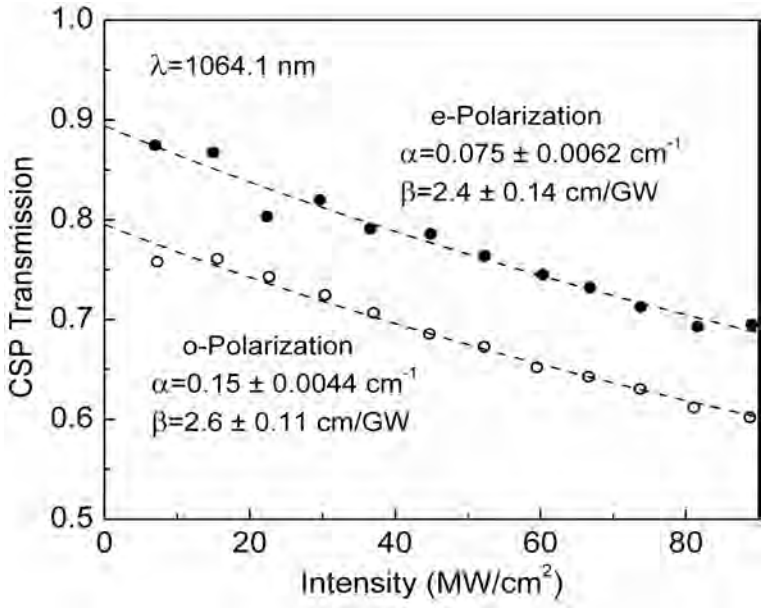

Figure 7.5: CSP transmission as a function of pump intensity for o- and e-polarization at 1064.1 nm.

7.4 Results and discusion

7.4.1 Tuning

We characterized the OPO with regard to output pulse energy and tunability by varying the crystal temperature at constant pump energy of 30 mJ. Figure 7.6 shows the generated idler wavelengths as a function of temperature along with the theoretically estimated wavelengths calculated from equations 7.1, 7.2 and 7.3. The idler wavelength changes at a rate of 3 nm/°C. The discrepancy between the calculated and experimental data points could be due to equation 7.3, indicating that the temperature dependent Sellmeier equations have to be further modified. Figure 7.7 shows the extracted idler energy as well as the transmission of CSP crystal across the tuning range. Using a 500 μm fused silica etalon, we extracted part of the intracavity signal to monitor the wavelength. The signal wavelength was recorded by using a low-resolution (∼10 nm) InGaAs spectrometer (Ocean optics, NIR Quest), and was further confirmed by single-pass second harmonic generation into the red

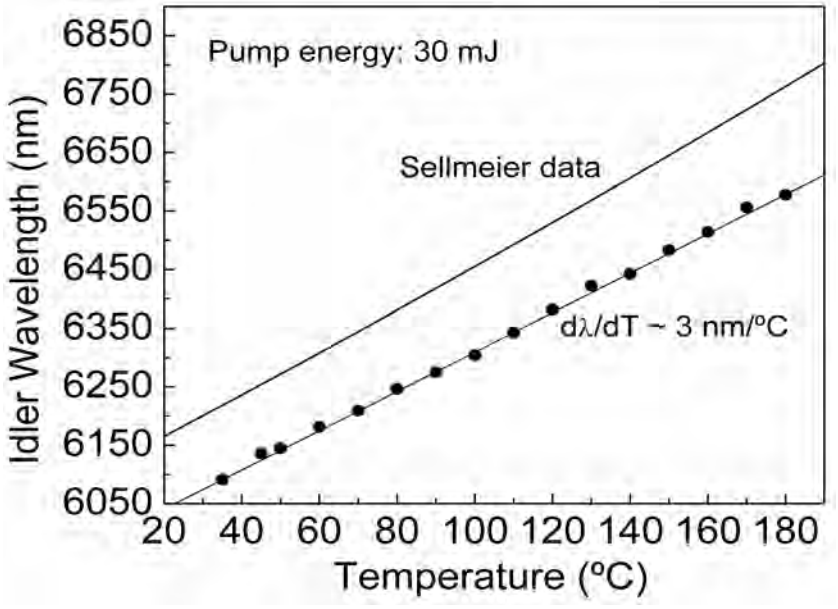

Figure 7.6: Temperature tuning of CSP OPO.

in a 5 mm Type-I ($oo \rightarrow e$) BBO crystal. The idler wavelength was inferred from the second harmonic of the signal, which was measured using a high resolution ($\sim$1) CCD array spectrometer (Ocean optics, USB 4000). By changing the CSP crystal temperature from 30 °C to 180 °C, we could tune the idler wavelength from 6091 to 6577 nm, corresponding to a total tuning range of 486 nm. The generated idler energy varies from 1.3 mJ at 6091 nm to 1 mJ at 6577 nm, reaching a maximum of 1.5 mJ at 6275 nm, with >1.2 mJ over >68% of the tuning range. This represents a maximum idler energy conversion efficiency of 5% and a photon conversion efficiency of 29.5%. The drop in the idler energy towards the longer wavelengths is attributed to the water absorption peak near 6.4 μm and residual multi-phonon absorption in the CSP crystal, resulting in reduced transmission, as evident from Fig. 7.7. The corresponding pump depletion is recorded to be >42% over more than 64% of the tuning range with a maximum pump depletion of 51% at 6483 nm. Also shown in the inset of Fig. 7.7 is the macro-pulse envelope of the input and the depleted pump, measured using a fast photodiode, at 30 °C, corresponding to an idler wavelength of 6091 nm, clearly showing >50% depletion.

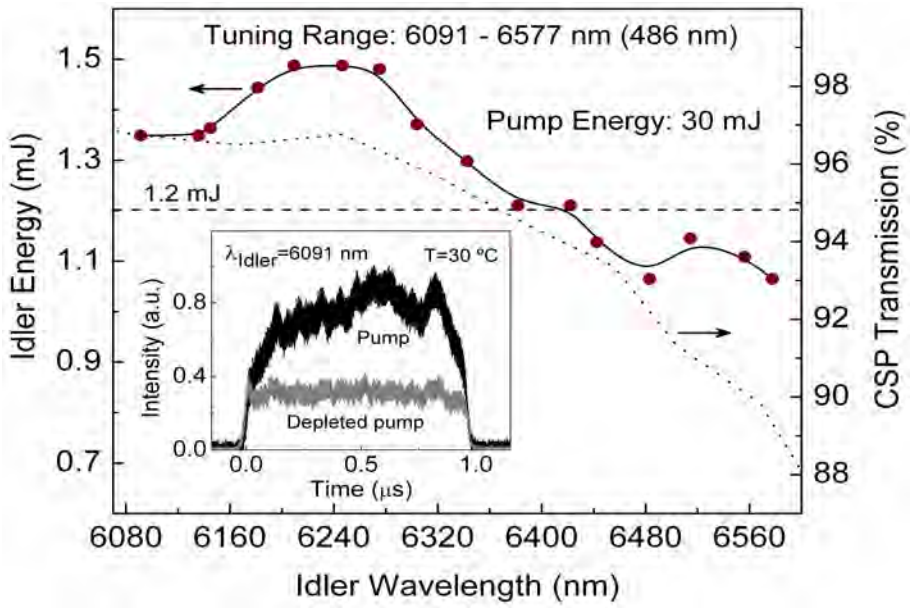

Figure 7.7: Idler energy and CSP transmission across the tuning range. Inset: Macro-pulse envelope of the input pump and the depleted pump.

7.4.2 Energy scaling

We also performed idler energy scaling measurements at different wavelengths across the OPO tuning range. The variation of the idler energy and pump depletion as a function of the pump energy obtained at a temperature of 30 °C, corresponding to an idler wavelength of 6091 nm, is shown in Fig. 7.8. As evident from the plot, 1.35 mJ of idler is obtained for a pump energy of 30 mJ at a slope efficiency, η=4.6%, implying a peak idler energy efficiency of 4.5%, representing a photon conversion efficiency of 25.7%. The threshold pump energy is measured to be 0.7 mJ, corresponding to single micro-pulse energy of 1.5 μJ, and strong pump depletion reaching >50% is achieved above input pump energy of 5 mJ. The peak efficiency in this experiment was limited by the low optical damage threshold of the single layer sapphire coating on the CSP crystal, observed beyond 30 mJ of pump energy. Increasing the pump energy to 31.5 mJ, representing a peak intensity of 100 MW/cm^2, resulted in surface damage on the input face of the crystal, while no damage was observed on the exit face, indicating that the damage is due to the pump beam. Although the damage

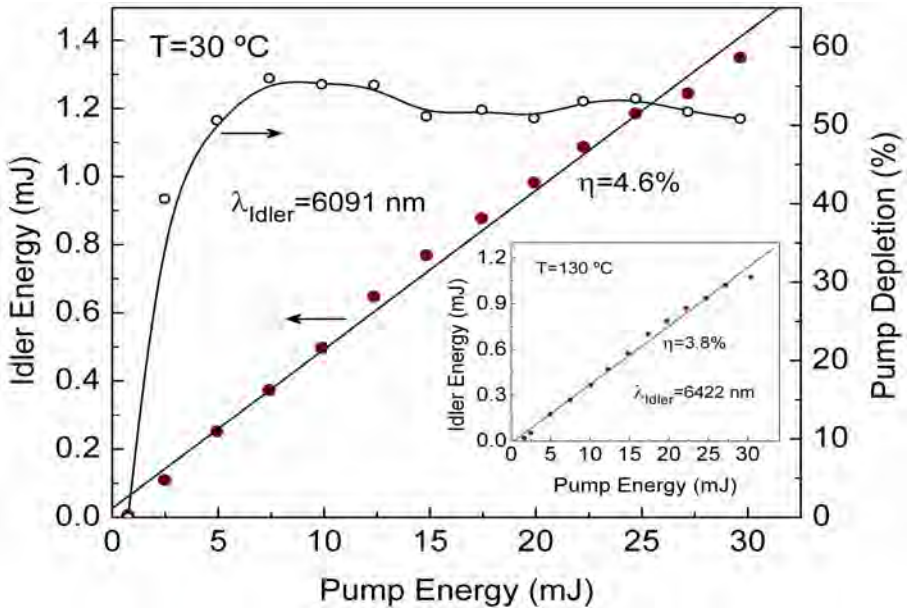

Figure 7.8: Idler energy scaling and pump depletion as a function of input pump energy at λ_{Idler}=6091 nm. Inset: Idler energy scaling at 6422 nm.

did not prevent OPO operation, a substantial drop of 37% in the idler energy was noticed. We also characterized the OPO near 6400 nm, a technologically important wavelength for surgical applications [100], as shown in the inset of Fig. 7.8. At 130 °C, corresponding to an idler wavelength of 6422 nm, an idler energy up to 1.1 mJ is generated for a pump energy of 30 mJ at a slope efficiency of η=3.8%, with an increased threshold pump energy of 1.6 mJ due to water absorption and reduced crystal transmission.

7.4.3 Spatial and temporal characteristics

Further, we have measured the duration of the signal pulses extracted from the OPO using a home-made autocorrelation setup. Figure 7.9 shows the measured autocorrelation profile at 1289 nm, where the amount of signal energy extracted from the cavity was >1.3 mJ for an incident pump energy of 30 mJ. The FWHM of the trace is 16.3 ps, resulting in the signal pulse duration of 10.6 ps, assuming a $sech^2$ pulse shape. This value of pulse duration was confirmed by repeating the

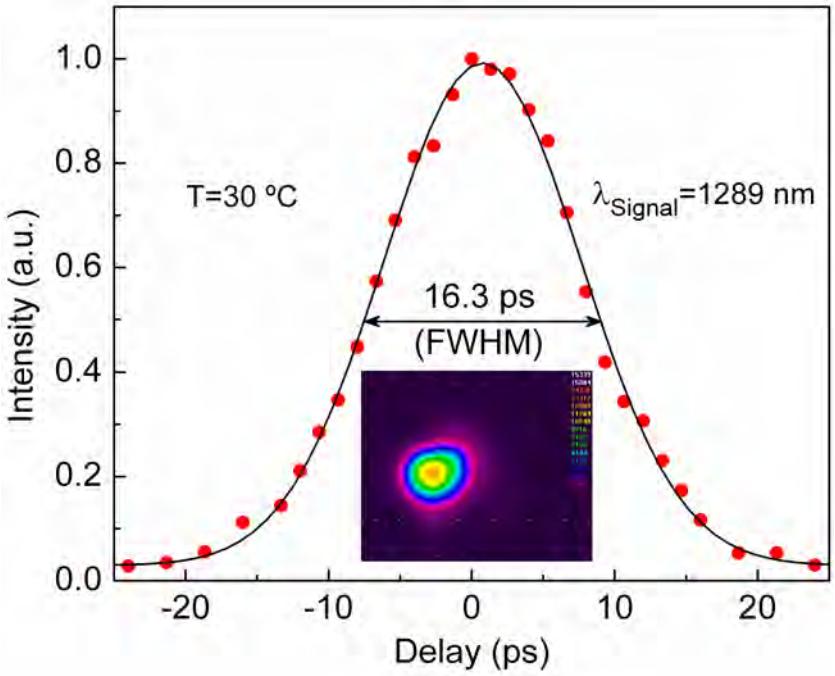

Figure 7.9: Typical autocorrelation of the OPO signal pulse at 1289 nm, with a duration of 10.6 ps (x1.54, assuming sech2 pulse shape). Inset: Signal beam profile at 1289 nm.

measurement several times, and similar pulse duration is expected across the tuning range. Also shown in the inset of Fig. 7.9 is the signal beam profile at 1289 nm, measured using a pyroelectric camera (Spiricon, Pyrocam-III). The corresponding idler beam profile at 6091 nm, recorded at full output energy, is shown in Fig. 7.10. Both signal and idler beam profiles confirm good beam quality with Gaussian profiles, which is important for surgical applications.

7.5 Conclusions

In this chapter, we have demonstrated a compact, high-energy, high-repetition-rate picosecond OPO based on CSP, pumped at 1064.1 nm, generating as much as 1.5 mJ of idler energy at 6275 nm. The OPO is tunable over 486 nm across the technologically important wavelength range of 6091-6577 nm for surgical applications, with >1.2 mJ over >68% of the tuning range. The compact design, high energy, suitable

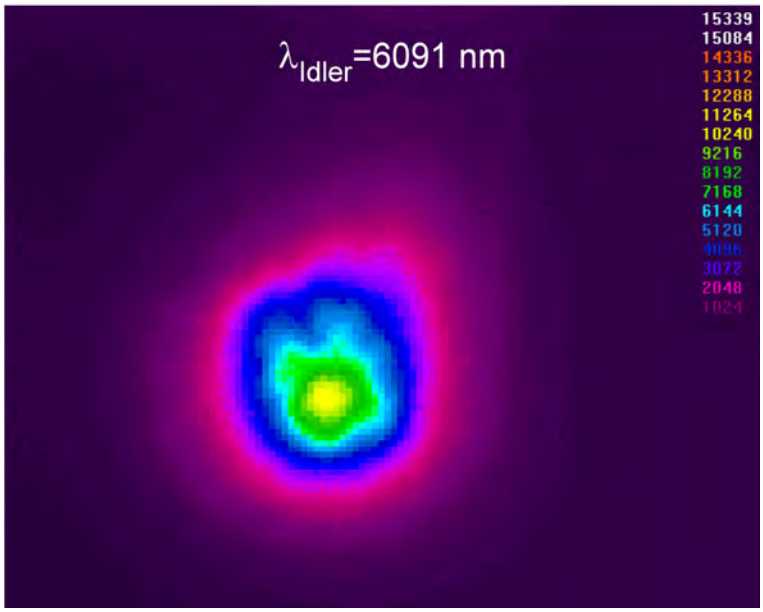

Figure 7.10: Spatial beam profile of the idler pulse at 6091 nm, showing TEM_{00} mode.

pulse structure, and the potential for energy scaling using larger aperture crystals, make the OPO a promising source for practical surgical applications in the mid-IR.

8 Fiber-laser second-harmonic-pumped Ti:sapphire laser

This chapter constitutes the following publications:

1. *High power, continuous-wave Ti:sapphire laser pumped by a fiber-laser green source at 532 nm*
   G. K. Samanta, **S. Chaitanya Kumar**, K. Devi, and M Ebrahim-Zadeh
   Optics and Lasers in Engineering 50, 215-219 (2012).

2. *Single-frequency, high-power, continuous-wave fiber-laser-pumped Ti:sapphire laser*
   S. Chaitanya Kumar, G. K. Samanta, K. Devi, S. Sanguinetti and M. Ebrahim-Zadeh
   Applied Optics (In press)

8.1 Motivation

The titanium-doped sapphire ($Ti : Al_2O_3$) laser is a remarkable addition to the class of tunable solid state lasers, which now is a reliable source of single-frequency continuous-wave (cw) radiation as well as ultrashort pulses in the near infrared spectral region [111, 112, 113, 114, 115, 116]. Its wide emission spectrum spanning from 680-1100 nm with peak around 800 nm has led to diverse applications such as spectroscopy, imaging of biological tissues, and many others. Since the absorption bands

of Ti:sapphire laser are located in the blue-green region of the visible spectrum, the pump sources for Ti:sapphire laser relied mainly on argon ion lasers and frequency doubled Nd-based lasers. Soon after the first demonstration of the Ti:sapphire laser pumped by argon ion laser [111, 112], cw, single frequency operation was realized by employing a ring cavity [113] and frequency stabilization [114], resulted in a linewidth as narrow as 1 kHz rms. Although the argon ion laser was powerful enough, it was very inefficient, expensive and bulky, resulting in a quick takeover by frequency doubled solid state lasers. The first cw single frequency all-solid-state Ti:sapphire laser, pumped by a diode pumped intracavity doubled Nd:YAG laser, operated at a threshold as low as 119 mW, generating 3.1 mW of output power at 800 nm for a pump power of 173 mW [115]. Recently, a cw Ti:sapphire laser pumped directly by a GaN diode laser in the blue was reported [116], but much is yet to be done in this direction to achieve practical output power. On the other hand, optically-pumped-semiconductor-lasers (OPSL) in the green can, in principle, be used to pump cw Ti:sapphire laser [117], but limited progress has been achieved in this area so far, leaving open the need for the development of powerful alternative green sources with high spatial quality and in simple, practical all-solid-state design to pump high-power cw or mode-locked Ti:sapphire lasers. Although Ti:sapphire laser technology is now fairly mature, it is interesting to note that Ti:sapphire oscillators are principally limited by the progress in green pump sources [118]. Fiber lasers have recently attracted much attention for their compact design, robustness, power scalability with turnkey operation and cost effectiveness. The combination of a cw infrared fiber laser and a simple single-pass second-harmonic-generation (SHG) scheme based on periodically poled nonlinear crystals is a potentially attractive approach for high-power cw green generation, not only because of its compact and practical architecture, but also due to the narrow linewidth and high spatial beam quality that are inherently transferable from the fiber pump laser to the green output. We have developed such a green source based on single-pass SHG of a Yb-fiber-laser in a 30-mm-long MgO:sPPLT

nonlinear crystal, generating as high as 9.6 W of single-frequency green power [40, 41]. Further efforts have been directed to scale the single-pass SHG efficiency up to 56% by using a novel multi-crystal scheme [43, 44], which is described in the next chapter . This fiber-laser-based green source has already demonstrated its potential as a successful pump source for a cw OPO [119], and hence it is worthwhile to explore its potential to pump a Ti:sapphire laser, which is a major application for a high-power, cw, green source.

In this chapter, we demonstrate for the first time, a high-power, cw, single-frequency, Ti:sapphire ring laser pumped by a fiber laser green source, with active frequency stabilization, generating as much as 2.25 W of output power at 812 nm for an incident green pump power of 11.3 W with a slope efficiency as high as 33.7 %. The laser is coarsely tunable over 47 nm, maintaining single-frequency output over the entire tuning range, and is continuously tunable over 181 MHz in 5 sec. Various cavity configurations have been systematically investigated to optimize the Ti:sapphire laser performance.

8.2 Single-pass SHG of Yb-fiber laser in MgO:sPPLT

Compact, high-power, green lasers are of interest for a variety of scientific and technological applications such as material processing, human surgery, and laser display technology. In cw, single-frequency operation, they hold promise as pump sources for singly-resonant optical parametric oscillators (SROs) [119] and Ti:sapphire lasers. With the rapid advances in fiber laser technology, access to high cw fundamental powers of tens of Watts is also no longer a limitation, making the choice of nonlinear material the most critical factor in the attainment of high optical powers and practical single-pass SHG efficiencies. In this regard, the most important material properties include high optical nonlinearity, long interaction length, noncritical phase-matching capability, and high optical damage threshold to withstand the large cw optical intensities. These requirements can be met by the new generation of quasi-phase-

Transmission range (μm)	0.2–6
Maximum available crystal length (mm)	40
Maximum available crystal thickness (mm)	3
Effective nonlinear coefficient (pm/V)	~9
Coercive field (kV/mm)	1.4
Absorption at 1064 nm ($\%/cm$)	0.17
Absorption at 532 nm ($\%/cm$)	1.57
Green induced absorption at 1064 nm (cm/GW)	5
Thermal conductivity ($W/m/K$)	8.4 (0.5% MgO)
Photorefractive damage threshold (MW/cm^2)	>2
Photorefractive damage threshold (MW/cm^2)	0.57

Table 8.1: Optical and thermal properties of MgO:sPPLT.

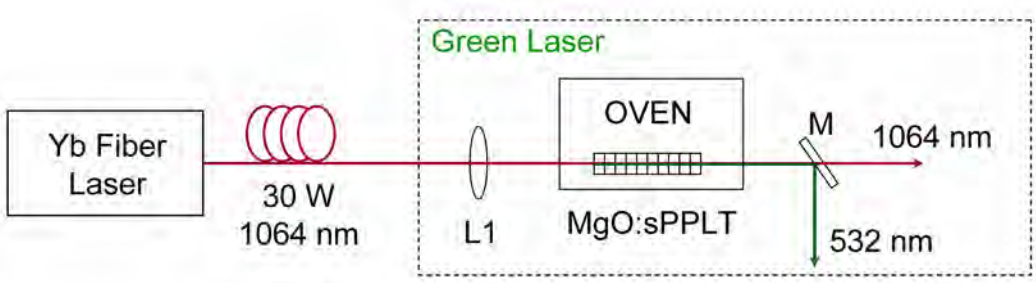

Figure 8.1: Experimental setup for single-pass second harmonic generation. L: Lens, M: Dichroic mirror.

matched (QPM) nonlinear crystals. In the section, we describe the Yb-fiber laser green source, based in single-pass SHG in MgO:sPPLT nonlinear crystal. The choice of the nonlinear crystal has been made by considering various important optical and thermal properties of the material, which are listed in Table 8.1.

8.2.1 Experimental setup

The schematic of experimental setup for single-pass SHG experiments is shown in Fig. 8.1. The fundamental pump source is a cw Yb-fiber laser (IPG Photonics,

YLR-30-1064-LP-SF) delivering linearly polarized single-frequency radiation at 1064 nm with a maximum output power of 30 W with a power stability of <1% over 1 hour and a nominal linewidth of 89 kHz, the same as that described in previous chapters. Using a confocal scanning Fabry-Perot interferometer (free-spectral-range $\sim$ 1 GHz, finesse $\sim$400), we confirm single-frequency operation of the laser, with a measured linewidth of 12.5 MHz, limited by the resolution of the interferometer. The frequency stability of the fiber laser is measured to be <120 MHz over 1 hour and <50 MHz over 30 minutes, while the power stability is measured to be <1% over 65 minutes. A Faraday isolator at the output end of the fiber protects the laser from any back-reflections. Using a 25 cm focal length lens and a scanning beam profiler, we measured the laser beam quality factor of M^2 <1.01. In order to maintain stable output characteristics, the pump laser is operated at maximum power and the input power to the SHG crystal is adjusted by using a combination of half-wave plate and polarizing beamsplitter cube. A second half-wave plate is used to obtain the correct polarization for phase-matched SHG in the nonlinear crystal. The fundamental beam is focused into the MgO:sPPLT crystal using a single lens, with the resulting beam waist of 31 μm corresponding to a confocal focusing parameter of ($\xi \sim 2.48$), positioned at the center of the crystal. The MgO:sPPLT crystal was 30-mm-long, 1-mm-thick, 2.14-mm-wide, with a single grating period of 7.97 μm. The end faces of the crystals was antireflection-coated (R<1%) at 1064 nm and 532 nm. Each crystal was directly mounted in an oven with a temperature stability of better than $\pm$0.1 °C. No interface material such as thermal paste or copper foil was used for heat exchange between the crystal and oven. A dichroic mirror, M, coated for high reflectivity (R>99%) at 1064 nm and high transmission (T>94%) at 532 nm, was used to extract the generated green output from the fundamental.

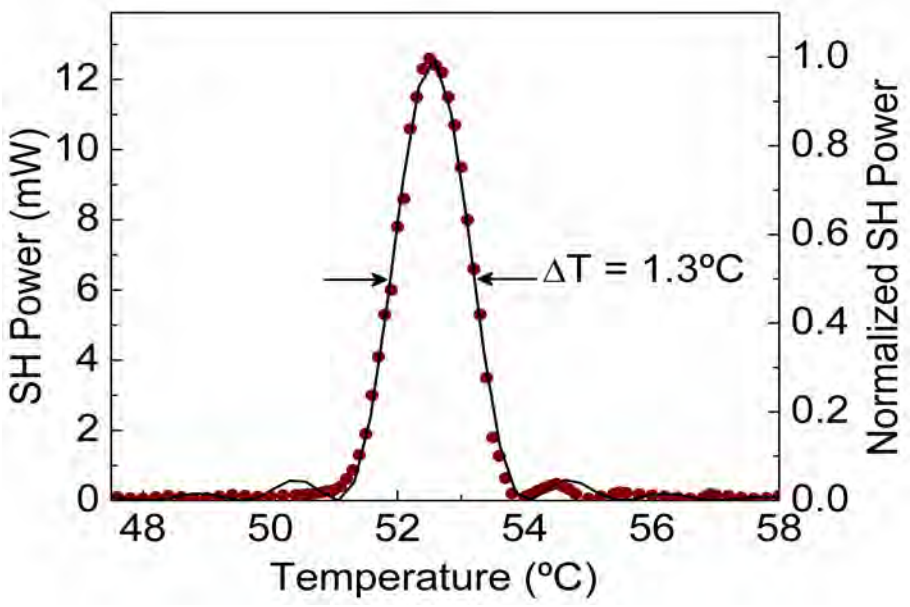

Figure 8.2: Temperature tuning curves of MgO:sPPLT, at 1 W of fundamental power.

8.2.2 Temperature acceptance bandwidth of MgO:sPPLT

In order to achieve efficient SHG, we first studied temperature phase-matching properties of the crystal, evaluating the acceptance bandwidth and phase-matching temperature. The variation of the second harmonic output with temperature at a fixed fundamental wavelength determines the temperature acceptance bandwidth of the nonlinear crystal and provides information about the uniformity of phase-matching throughout the crystal length. The SHG temperature tuning curve obtained for MgO:sPPLT crystal is shown in Fig. 8.2. The measurements were performed using a fundamental beam waist radius 37 μm corresponding to a focusing parameter of ξ = 1.74, at a fundamental power of approximately 1 W, in order to avoid any unwanted contributions from thermal effects. The $sinc^2$ fit to the experimental data has a fullwidth at half-maximum (FWHM) bandwidth of T = 1.3 °C at a phase-matching temperature of 52.5 °C. This value is slightly wider than the calculated value of 0.96 °C using the relevant Sellmeier equation [57]. The temperature acceptance bandwidth is calculated using equation 2.30 of chapter 2 [56]. The discrepancy between

the calculated and measured temperature acceptance bandwidth values arises from various factors including focusing, non-uniformity of the grating period and thermal effects. As the measurements were performed at low fundamental power, avoiding any contribution from thermal effects, the mismatch in the calculated and measured temperature acceptance bandwidth values can be possibly associated with focusing and non-uniformity of the grating period along the length of the crystal. The close agreement between the measured temperature tuning data and the ideal $sinc^2$ functions in Fig. 8.2 implies good homogeneity of refractive index at lower input power levels, resulting in a symmetric phase-matching curve.

8.2.3 SHG power scaling

The SHG power scaling results are shown in Fig. 8.3. We measured a SH power of 9.6 W at conversion efficiency of 32.7%, for a maximum fundamental power of 29.5 W. Although the characterization of the fiber based green source is performed at a fundamental power of 29.5 W, further increasing the fundamental power to ∼33 W provides >11 W of green power from our source. However, a clear saturation effect is evident from the deviation of the SHG efficiency from linearity. The saturation in the SHG efficiency is attributed to thermal effects due to absorption at both fundamental and SHG wavelengths. Therefore, we performed linear absorption measurements at both the wavelengths, confirming the major contribution to crystal heating is clearly from the absorption of 1.57%/cm due to the generated green power, which necessitates the reduction of the crystal temperature to achieve optimum phase-matching. However, given a significant linear absorption of 0.17%/cm at 1064 nm, the role of fundamental absorption to crystal heating can not be entirely neglected.

In order to further study the effects of crystal heating due to light-induced linear absorption on SHG conversion efficiency, we also investigated two different thermal management schemes based on different oven designs shown in Fig. 8.4. In the first design (close-top), the oven encloses the crystal on all sides, except the input and

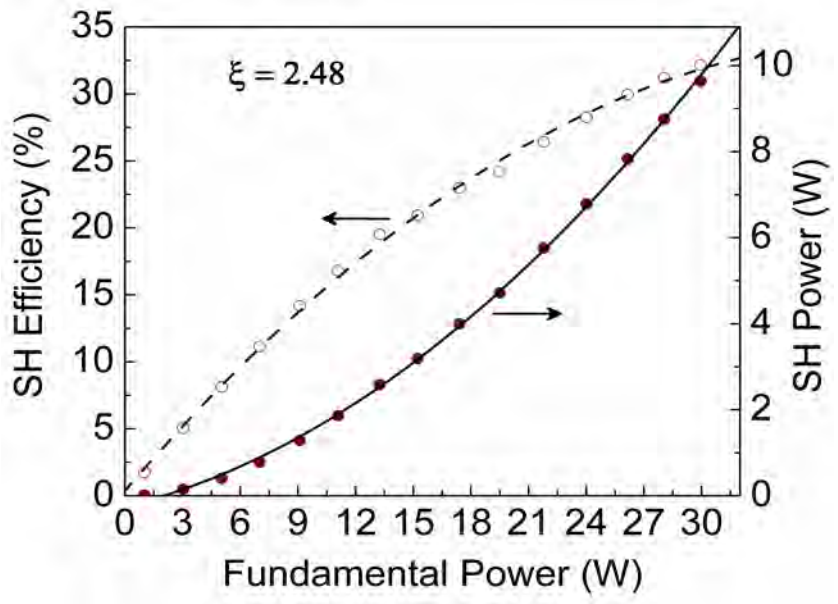

Figure 8.3: Dependence of measured SH power and corresponding conversion efficiency on the fundamental power.

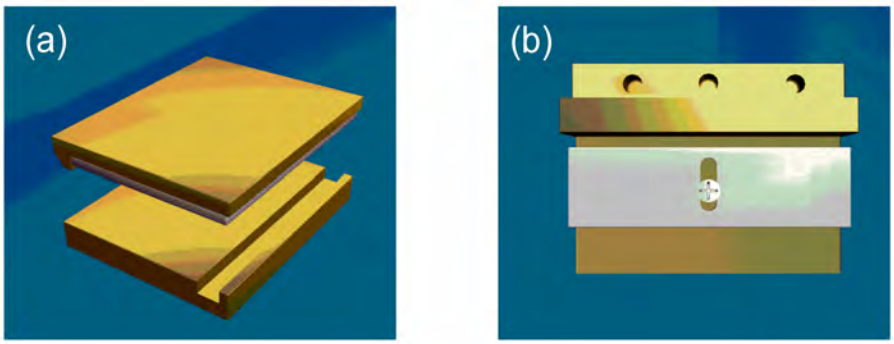

Figure 8.4: (a) Close-top (CT), and (b) Open-top (OT) crystal housing configurations used for single-pass SHG in MgO:sPPLT.

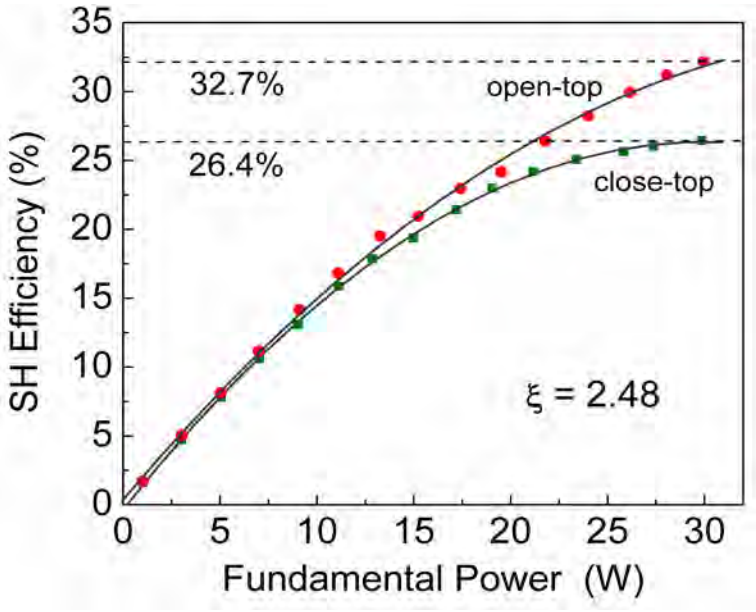

Figure 8.5: SHG efficiency as a function of fundamental power in close-top and open-top configurations.

output facets. In the second (open-top), the crystal is exposed to the ambient from the top as well as the input and output facets. We performed power scaling measurements using both designs under identical focusing conditions, using a fundamental optimum beam waist radius of 31 μm (ξ=2.48). The results are shown in Fig. 8.5. From the plot, we clearly observe a significant difference in the SHG efficiency using the two different oven designs, with the difference increasing at higher fundamental powers. The maximum SHG efficiency achieved at the full fundamental power using the close-top oven design is 26.43%, while the open-top oven configuration results in a maximum SH efficiency of 32.7%. We attribute this significant difference to the easier heat exchange between the crystal and the ambient air in the open-top oven design, which permits the required reduction in crystal temperature for optimum phase-matching to be achieved and maintained, whereas in the close-top design this optimum equilibrium condition is difficult to achieve. These observations imply that careful design of crystal heating components and the oven can also play an important role in the attainment of highest SHG efficiency.

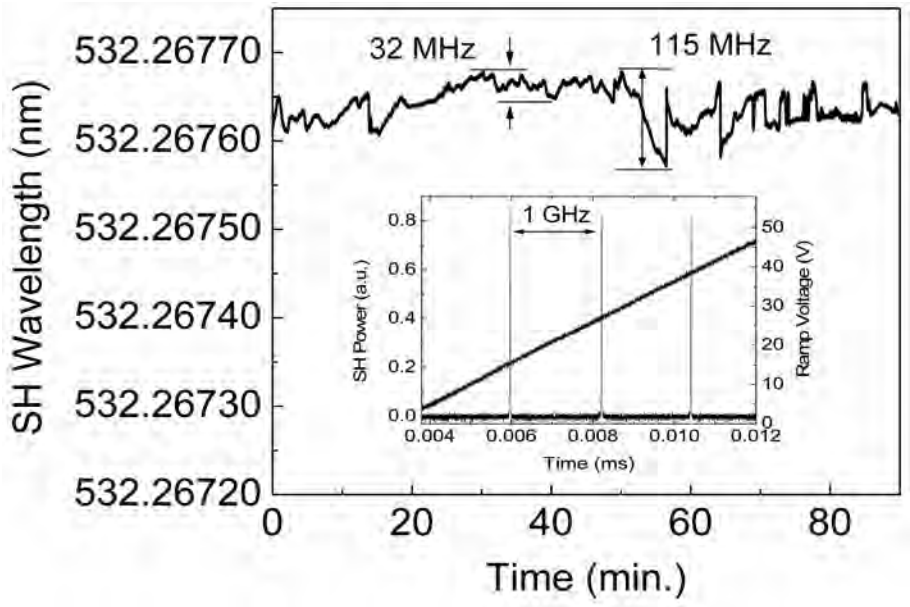

Figure 8.6: Frequency stability of MgO:sPPLT recorded over 90 minutes at 9.6 W of SH power.Inset: Single-frequency operation of the fiber laser based green source.

8.2.4 Frequency stability and single-frequency operation

We also investigated the frequency stability of the generated green radiation in MgO:sPPLT using a wavemeter (HighFinesse, WS-U 30). The measurements were performed at the maximum green power, close to the maximum SHG efficiency, under free-running conditions, and in the absence of any thermal isolation. The results are shown in Fig. 8.6, where it can be seen that the green output exhibits a passive frequency stability with a peak-to-peak fluctuation of <115 MHz over 90 minutes. Further, a short-term stability of <32 MHz over 30 minutes and a long-term stability of <370 MHz over 12 hours have been recorded for SHG from MgO:sPPLT.

Also shown in the inset of Fig. 8.6 is the single-frequency operation of the green source. Using a confocal scanning Fabry-Perot interferometer (free-spectral-range of 1 GHz; finesse of 400), we recorded the transmission fringes of the green output. The measurements resulted in an instantaneous SHG linewidth of 6.5 MHz, limited by the resolution of the interferometer.

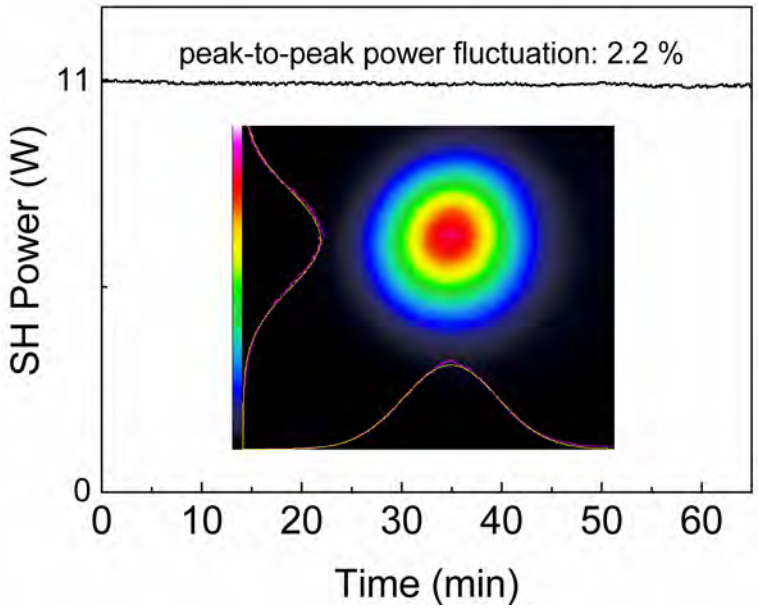

Figure 8.7: SH power stability of the fiber based green source. Inset: Beam profile of the generated green radiation.

8.2.5 Power stability and beam quality

We have also characterized the fiber based green source in terms of power stability and beam quality, whose results are shown in Fig. 8.7. Using a novel uniform crystal heating configuration, where the crystal is placed at the center of a large-area oven used to heat the 50-mm-long crystal, we recorded a peak-to-peak power fluctuation of 2.2% over 1 hour. Similar measurement using a small area oven has resulted in a peak-to-peak fluctuation of 7.6% over 8 hours and 9% over 13 hours [40, 41]. As compared to the small-area oven, the central part of the new large-area oven provides higher temperature uniformity and is less sensitive to the instability (±0.1 °C) of the temperature controller. As a result, it maintains improved temperature stability over the full crystal length, resulting in higher green output power stability.

The far-field energy distribution of the SHG is determined by recording the spatial beam profile of the green beam, which is shown in the inset of Fig. 8.7. Further, we have also measured the M^2 value of the generated green beam by scanning a beam profiler across the Rayleigh range of the focused beam. The measurements resulted

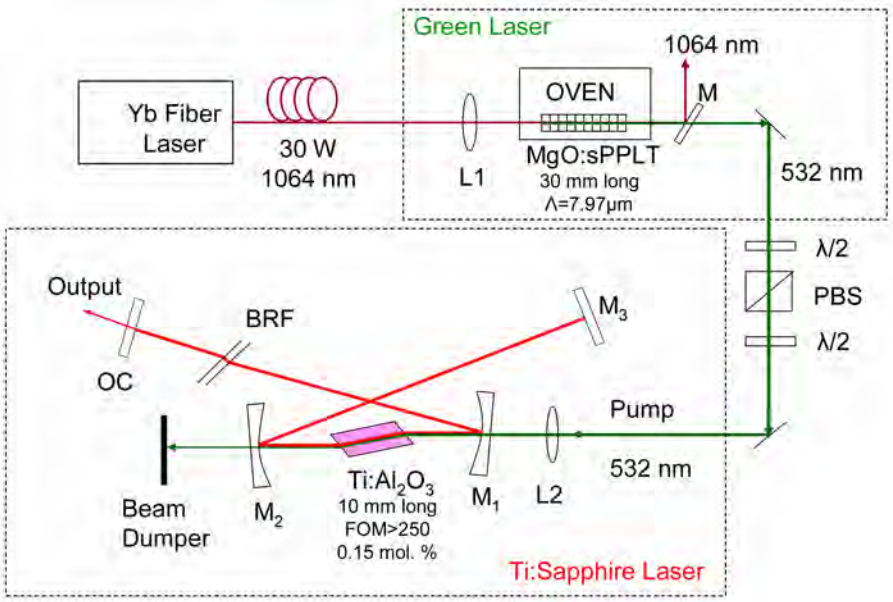

Figure 8.8: Schematic of the cw fiber-laser-green-pumped Ti:sapphire laser. $\lambda/2$: half-wave plate; PBS: polarizing beam splitter; L: lenses; M: mirrors; OC: output coupler, BRF: birefringent filter.

in a value of M_x^2<1.29 and M_y^2<1.33 at maximum green power.

8.3 Fiber-laser-SHG pumped Ti:sapphire laser

8.3.1 Experimental setup

In order to characterize the Ti:sapphire ring laser for optimum performance, we initially operated the laser in standing wave, X-cavity configuration. The schematic of the experimental setup is shown in Fig. 8.8. The pump source is the Yb-fiber laser based green source described earlier in this chapter. To maintain stable output characteristics, we operate our green source at maximum power and the input green power to the Ti:sapphire laser is varied using a half- wave-plate and a polarizing beam-splitter. The pump beam is focused at the center of the 10-mm-long, Brewster-cut Ti:sapphire crystal (0.15 wt.% doping, FOM>270), which is located on a brass slab, and is water-cooled only on the lower side. The green beam is polarized along the c-axis of the crystal in order to maximize absorption [113], which we measured

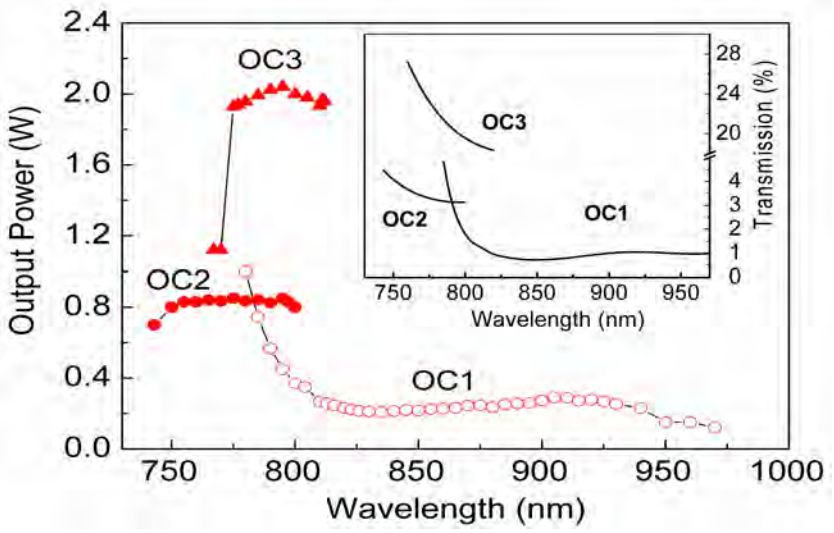

Figure 8.9: Output power across the tuning range of the Ti:sapphire laser using three different output couplers and two sets of cavity mirrors. Inset: transmission of the output couplers OC1, OC2 and OC3 versus wavelength.

to be >80%. The laser is configured in an astigmatic-compensated, standing-wave cavity, comprising two concave mirrors, M_1 and M_2 (r=10 cm), a plane mirror M_3, and an output coupler (OC). To access the widest tuning range, we used two sets of mirrors, all of the same radius of curvature (r=10 cm) and with high reflectivity (>99%) across 760-840 nm and 840-1000 nm. For wavelength tuning and control, we used a birefringent filter (BRF).

8.3.2 Ti:sapphire laser tuning

We measured the output power of the Ti:sapphire laser across the tuning range using both sets of concave mirrors, by deploying different output couplers of varying transmission across 740-970 nm, as shown in Figure 8.9. Tuning was achieved using the BRF. In Figure 8.9, the output power across the obtained tuning range is plotted for three different output couplers. For OC1 (T=5%-0.74% over 780-970 nm), the output power exactly follows the transmission curve (inset of Fig. 8.9) up to the wavelength ~940 nm, with no evidence of the expected drop in output power due to gain reduction in the Ti:sapphire crystal at longer wavelengths. This can be

attributed to the high intracavity power due to the combination of high pump power (10.5 W) and low output coupling, pointing to the possibility of extracting higher power across the tuning range using larger output coupling. However, beyond ∼940 nm, there is a drop in output power with the increase in output coupling, due to the lower gain of the Ti:sapphire crystal [111]. Tuning below 780 nm is limited by the higher loss due to increased output coupling at shorter wavelengths. Therefore, using OC1 and both sets of cavity mirrors, the Ti:sapphire laser can be continuously tuned over 780-970 nm with a maximum power of 1 W at 780 nm. To enhance the tuning range and output power, we deployed two additional output couplers of varying transmission, OC2 (T=4.4%-3.12% across 743-800 nm) and OC3 of (T=25%-18.6% across 767-812 nm), also shown in the inset of Fig. 8.9. With OC2, we obtain tuning across 743-800 nm with a maximum power of 0.85 W at 795 nm. With OC3, we obtain an output power up to 2.04 W at 795 nm for an output coupling of 20%, with >1.12 W available across 767-812 nm. Hence, using two sets of cavity mirrors and three output couplers, we achieve a total wavelength tuning range of ∼227 nm across 743-970 nm and generate up to 2.04 W of output power. Wavelength tuning below 743 nm is limited by the reflectivity fall-off of the cavity mirrors, whereas coverage beyond 970 nm is limited by the free spectral range of the BRF.

8.3.3 Output coupling optimization

To optimize the output coupling for maximum power extraction, we operated the Ti:sapphire laser in free-running cavity at a fixed pump power of ∼10.5 W (at the Ti:sapphire crystal) and used several additional output couplers with transmission ranging from 1.4% to 40.7% at ∼812 nm, where the laser operated due to the lowest cavity loss in the absence of BRF. We measured the extracted power and corresponding operation threshold of the Ti:sapphire laser as a function of output coupling, with the results shown in Fig. 8.10. The output power rises from 1 W to 2.24 W with the increase in output coupling from 1.4% to 19.9%. However, further increase in output

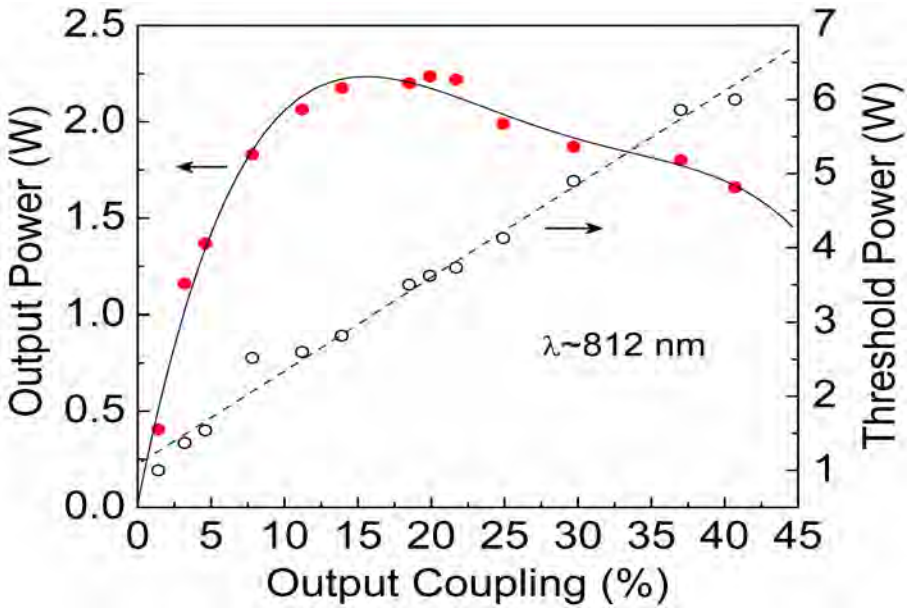

Figure 8.10: Output power and threshold power of the Ti:sapphire laser as a function of output coupling at ∼812 nm.

coupling results in reduced output power with a clear peak near 20%, implying an optimum output coupling of 20% for our laser. As expected, the laser threshold increases linearly with the output coupling and reaches 6 W at 40.7% with an output power of 1.66 W. Higher output coupling is possible with our laser for the available pump power, but will result in reduced output power. It is to be noted that the temperature rise in the Ti:sapphire crystal due to pump absorption effectively decreases the fluorescence lifetime and quantum efficiency by ∼10% and thermo-optical aberrations due to temperature gradients in the crystal also limit the laser output power [118, 120]. Therefore, an enhancement in output power is feasible by implementing thermal management of the crystal by water cooling from all four sides.

8.3.4 Power scaling

Having determined the optimum output coupling of 20%, we investigated power scaling of the Ti:sapphire laser. Figure 8.11(a) shows the variation of output power as the function of pump power without the BRF, for two different pump beam waist

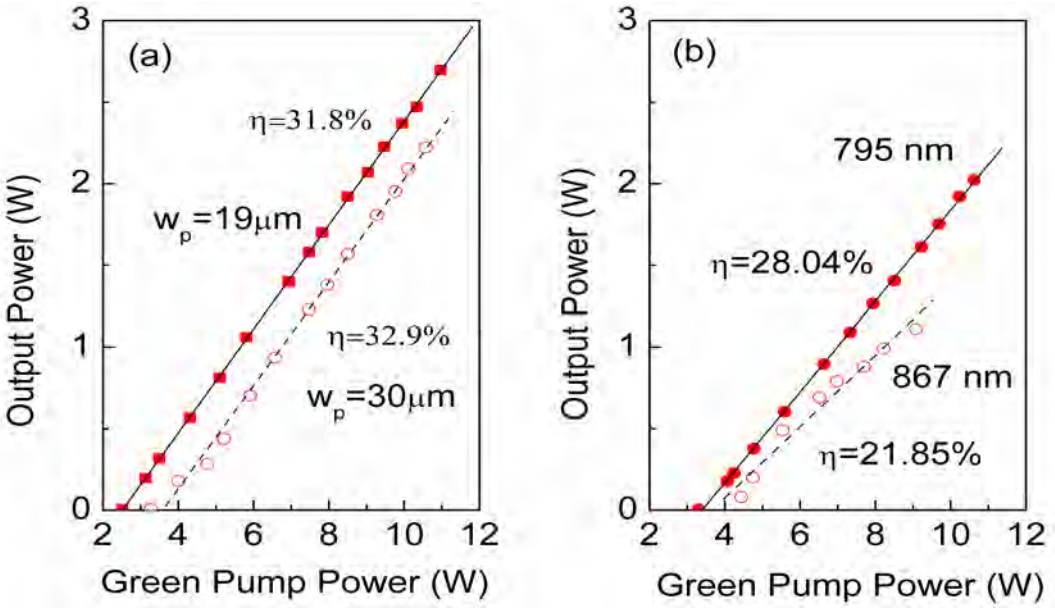

Figure 8.11: Variation of the output power of the Ti:sapphire laser with input power (a) for different pump waists, and (b) at different wavelengths, for an output coupling is 20%.

radii of 25 μm and 30 μm. With a pump beam waist of 25 μm and 20% output-coupling, the Ti:sapphire laser has a threshold of 2.51 W and the output power increases with pump power with a slope efficiency of 31.8%, reaching a maximum value of 2.7 W at ∼11 W of pump power. With a pump beam waist of 30 μm, the laser threshold increases to 3.27 W, but the output power rises with a slope efficiency as high as 32.9%, reaching 2.22 W for 10.57 W of pump power. It may, thus, be concluded that the laser operates robustly with an output power >2.2 W and slope efficiency >31.8% for a range of focused pump beam waists from 25 μm to 30 μm. Further enhancement in output power is also expected by using tighter pump focusing.

Using the BRF, we also measured the power scaling of the Ti:sapphire laser at two different wavelengths of 795 nm and 867 nm for the same pump beam waist of 30 μm, as shown in Fig. 8.11(b). At 795 nm, the laser has a threshold of 3.33 W and generates an output power as high as 2.02 W with a slope efficiency of 28%. On the

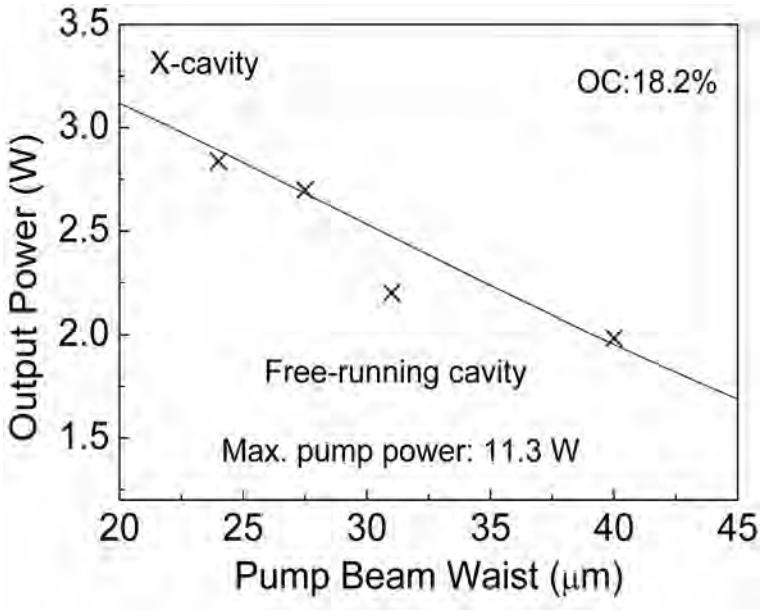

Figure 8.12: Ti:sapphire laser output power as a function of pump beam waist in X-cavity configuration.

other hand, at 867 nm we have a maximum output power of 1.1 W, a slope efficiency of 21.8%, and higher threshold of 4 W, due to gain reduction in the Ti:sapphire crystal away from the emission peak at 795 nm.

8.3.5 Beam waist optimization

Under free-running condition, with an experimentally determined optimum output coupling of ∼18.6% at 812 nm for a pump beam waist ∼30 μm, we investigated the optimum pump beam waist at the center of the Ti:sapphire crystal. Using four different plano-convex lenses of focal length f=50, 75, 100, 125 mm, we focused the pump beam to waist radii, w_p=24, 27, 30, 40 μm, respectively, in the Ti:sapphire crystal. The laser is optimized in each case to achieve maximum output power, which is recorded as a function of the pump beam waist, as shown in Fig. 8.12. The solid line corresponds to the theoretically calculated achievable output power as a function of the pump beam waist [113]. As evident from Fig. 8.12, a maximum output power of 2.84 W is achieved for pump beam waist of 24 μm, which drops down to 1.96 W

at a beam waist of 40 μm, for a maximum available pump power of 11.3 W. So, we use the 50 mm focal length lens and 18.6 % output coupler to operate the laser in astigmatism compensated four mirror ring cavity.

8.4 Single-frequency Ti:sapphire laser

8.4.1 Experimental setup

The schematic of the single-frequency Ti:sapphire laser experimental setup is shown in Fig. 8.13. The pump source is a cw, single-frequency Yb-fiber laser based green source described in section 8.2. At the highest available fundamental power of ∼33 W from the fiber laser, our SHG source provides as much as 11.3 W of green power in a TEM_{00} spatial profile. Using a suitable plano-convex lens (L2=50 mm), we focused the green pump beam to a waist radius of 24 μm at the center of the 10-mm-long, Brewster-cut Ti:sapphire crystal (0.15 wt.% doping, FOM>270). In the present experiment, the laser is configured in an astigmatic-compensated, four mirror ring cavity comprising two plano-concave mirrors, M_1 and M_2 of radius of curvature (r=10 cm), a plane mirror M_3 mounted on a piezo (PZT), and a plane output coupler (OC). All the mirrors are broadband anti-reflection coated and provide high transmission (T>97%) at 532 nm and high reflectivity (>99.5%) across 760-840 nm. The transmission of the output coupler varies from 24% at 773 nm to 18% at 822 nm. The total length of the cavity is 109 cm (FSR∼275 MHz). A BRF is used to tune the laser wavelength. An intracavity optical diode, comprising a Faraday rotator in combination with a half-wave-plate ensures unidirectional operation of the ring laser and an intracavity etalon provides single-mode operation. A home-made ultra-stable Fabry-Perot interferometer is used as an external reference to maintain the long-term frequency stability of the Ti:sapphire ring laser, with the help of the usual lock-in techniques, thoroughly described in the following section. We will see that the reference can be easily tuned and this feature allows continuous tuning of

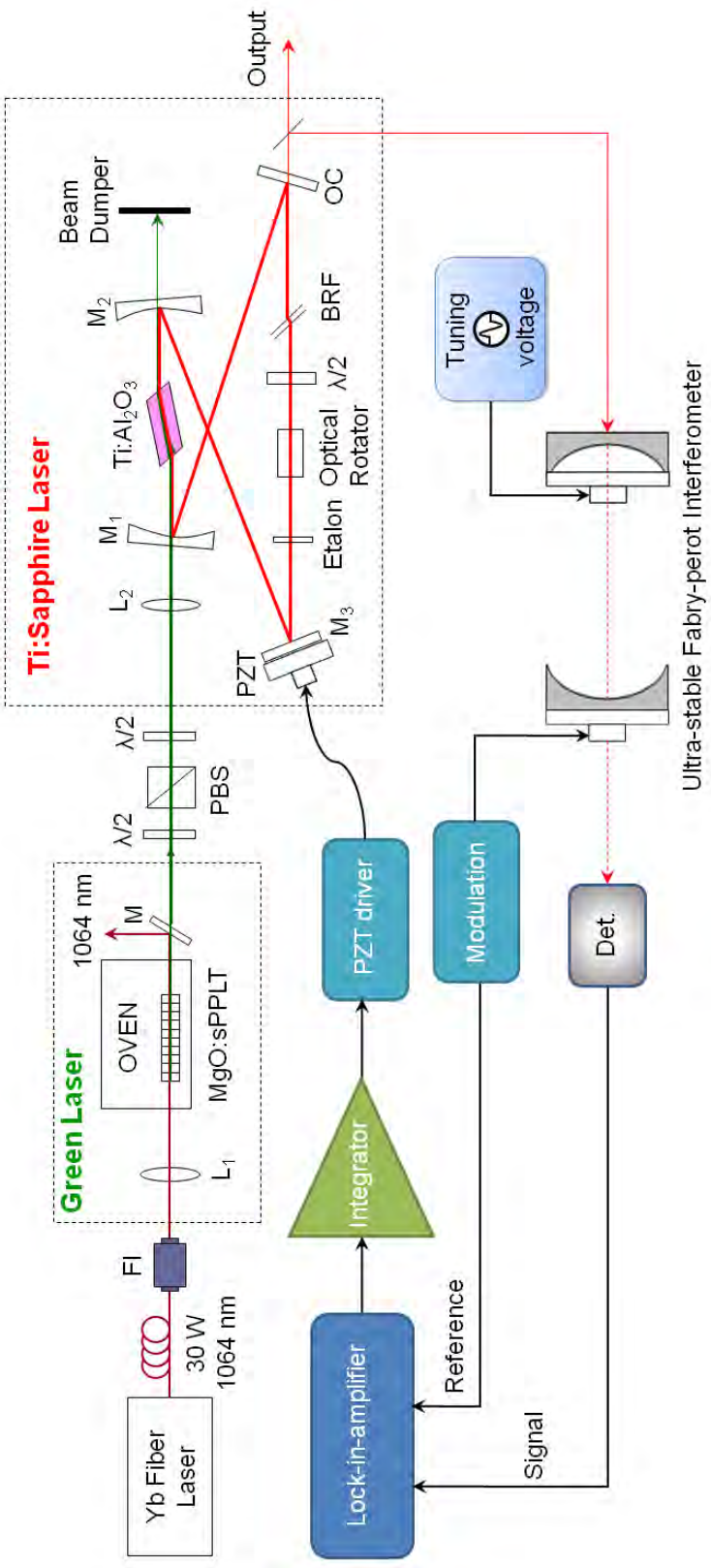

Figure 8.13: Schematic of the fiber-laser-based green-pumped cw single-frequency Ti:sapphire ring laser. FI, faraday isolator; λ/2, half-wave-plate; PBS, polarizing beam splitter; L, lens; M, mirrors; OC, output coupler; PZT, Piezo; BRF, birefringent filter; Det., detector.

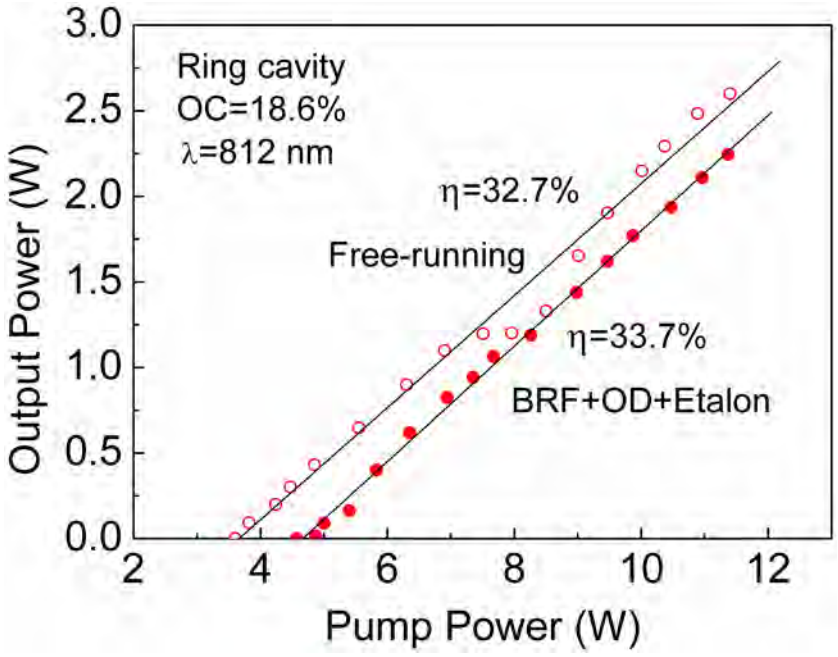

Figure 8.14: Power scaling characteristics of Ti:sapphire ring laser in free-running condition as well as with the intracavity elements(BRF, optical diode and etalon).

the stabilized laser.

8.4.2 Power scaling

The power scaling results of the Ti:sapphire ring laser, with and without (free-running condition) intra-cavity elements such as BRF, optical diode and etalon, are shown in Fig. 8.14. In free-running condition, the bidirectional ring laser operated at a threshold pump power of 3.6 W, generating a total output power of 2.6 W for a pump power of 11.3 W with a slope efficiency of 32.7%. Unidirectional operation of the ring laser is achieved by introducing an optical diode. Introducing all the intracavity elements leads to an increase in the threshold pump power to 4.5 W and a 16% reduction in the output power as compared to the free-running condition, generating a maximum single-frequency output power as high as 2.25 W for the same incident pump power of 11.3 W at a slope efficiency of 33.7 %. The corresponding optical-to-optical efficiency with respect to the incident and absorbed pump power

are 20% and 25%, respectively. No sign of saturation is observed while pumping up to the maximum available pump power.

8.4.3 Tuning and single-frequency operation

Owing to the broad emission bandwidth of the Ti:sapphire laser, tuning of the output wavelength over 47 nm, from 774 nm to 821 nm, is achieved by using BRF. The output power across the tuning range for a constant pump power of 11.3 W, along with the coating curve of the output coupler transmission, which varied from 24% at 773 nm to 18.2% at 822 nm, is shown in Fig. 8.15(a). The Ti:sapphire ring laser tunability is only limited by the coating specifications of the cavity mirrors.

Although the output coupling is decreasing, the output power of the Ti:sapphire ring laser is found to increase with a maximum of 2.25 W at 812 nm, as seen in Fig. 8.15(a). This is attributed to the fact that the Ti:sapphire has a gain peak around 800 nm, resulting in high output power, in spite of the low output coupling. Also, the 18.6% output coupling is optimum for the 812 nm wavelength, beyond which the output power also decreases as the output coupling decreases. Further, the spectral characteristics of the Ti:sapphire laser are studied using a commercial scanning Fabry-Perot interferometer (free-spectral-range of 1 GHz, finesse 400). The typical fringe pattern corresponding to a wavelength of 812 nm, recorded at the maximum output power, is shown in Fig. 8.15(b), with a measured instantaneous linewidth of 5.4 MHz, verifying the single-frequency operation of the laser. The single-frequency nature of the Ti:sapphire laser at different output wavelengths is found to be maintained over the entire tuning range.

8.4.4 Frequency stability and continuous tuning

In order to improve the performance of the Ti:sapphire ring laser in terms of frequency stability, we set up a stabilization system. The external reference for the laser frequency is provided by a home-made Fabry-Perot interferometer, carefully designed

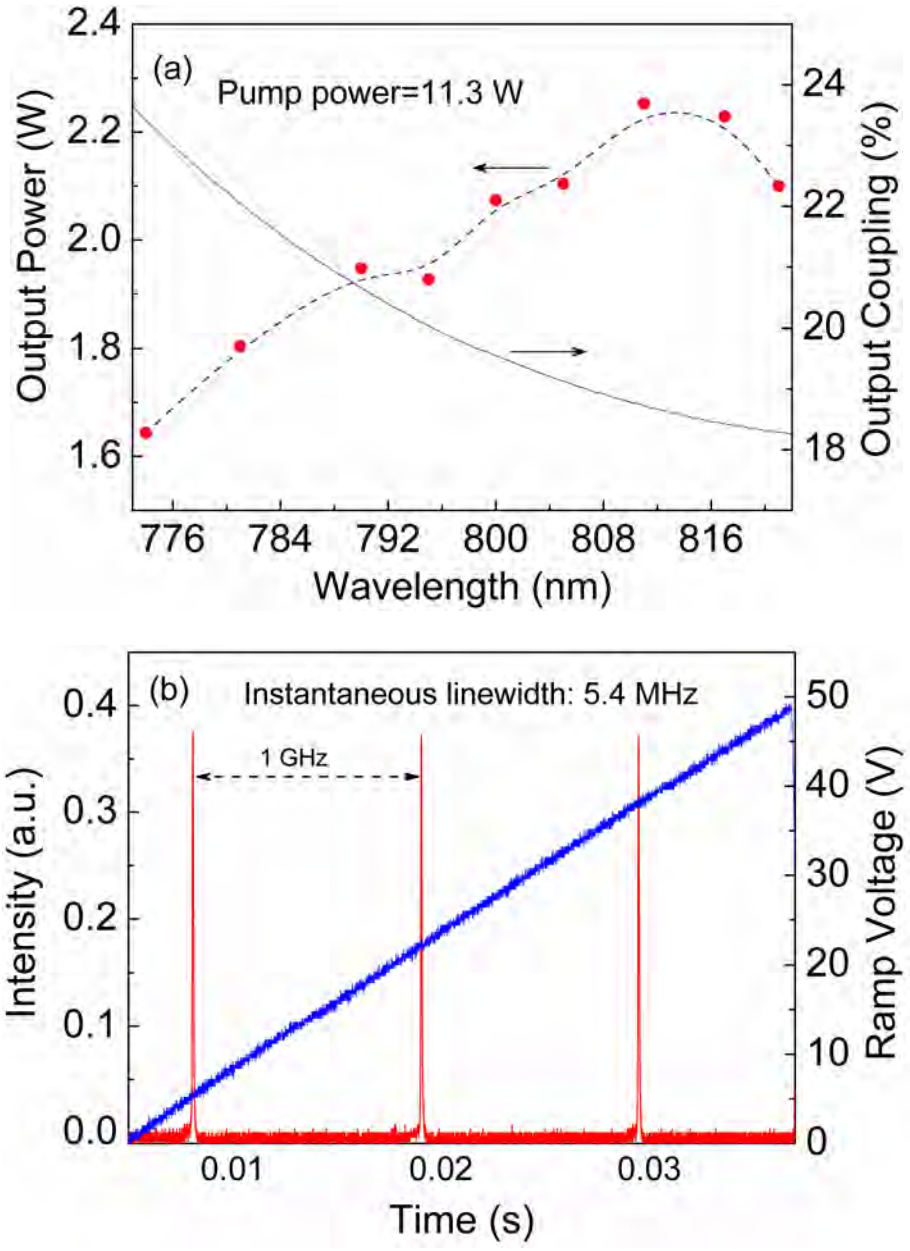

Figure 8.15: (a) Extracted power and output coupler transmission, of the Ti:sapphire ring laser across the tuning range, (b) Single-frequency spectrum of the Ti:sapphire ring laser output recorded by a scanning Fabry–Perot interferometer (free-spectral-range 1 GHz and finesse 400) at 812 nm.

to be as stable as possible. The main structure, which supports the mirror holders, is a thick super-invar cylinder. All parts of the interferometer (except piezos and mirrors) are made of this ultra-low thermal-expansion material, with the intention of minimizing the dependence of the reference on temperature. Two identical piezos drive the position of the cavity mirrors and provide two independent fine adjustments for the resonator length. Again, with the aim of reducing thermal instabilities, our piezos are only 3 mm long and they are placed in the same direction (both glued on the left side of each mirror, as shown in Fig. 8.13), in order to compensate the effect of their thermal expansion on the cavity length. The mirror spacing can be adjusted at any value between 2 and 12 cm. In the present work, we operated in a confocal geometry with a 10 cm resonator length, corresponding to a 750 MHz free spectral range. A small part of the Ti:sapphire beam is sent into the interferometer and a feedback loop stabilizes the laser frequency to the maximum of a transmission peak. In practice, one piezo of the interferometer is modulated at a frequency of about 10 kHz and the signal from the detector is demodulated by a lock-in amplifier, thus providing our error signal. After integration, this signal drives the piezo on which the plane cavity mirror (M_3) is mounted, in such a way that the laser frequency is maintained to the maximum of the transmission peak. The output wavelength of the stabilized Ti:sapphire laser was recorded using a very high-resolution wavemeter (HighFinesse, WS-U30). The observed a stability was better than 12 MHz over 10 minutes (Fig. 8.16(a)) at the maximum output power of 2.23 W around 817 nm. We also tried to use a commercial Fabry-Perot with an aluminum mechanical structure as a reference, instead of the super-invar home-made interferometer. In this case, as shown in Fig. 8.16(b), the frequency drift is measured to be within 30 MHz over 7 minutes. The better result obtained with the home-made Fabry-Perot is attributed to the superiority of super-invar over aluminum, for mechanical stability and low thermal expansion.

Along with the frequency stability, many applications such as spectroscopy also

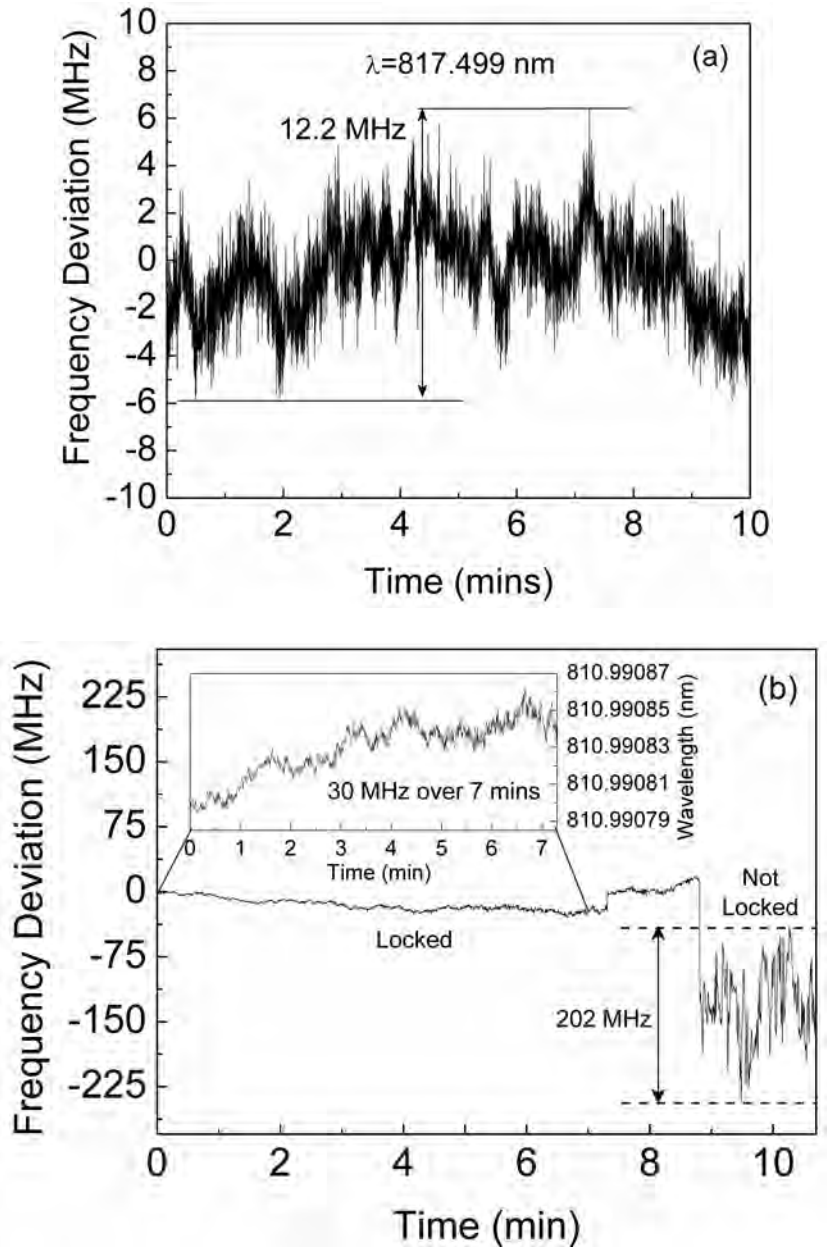

Figure 8.16: Frequency stability of the Ti:sapphire ring laser: (a) with stabilization to the home-made super-invar Fabry-Perot; (b) with stabilization to the commercial Fabry-Perot and without stabilization.

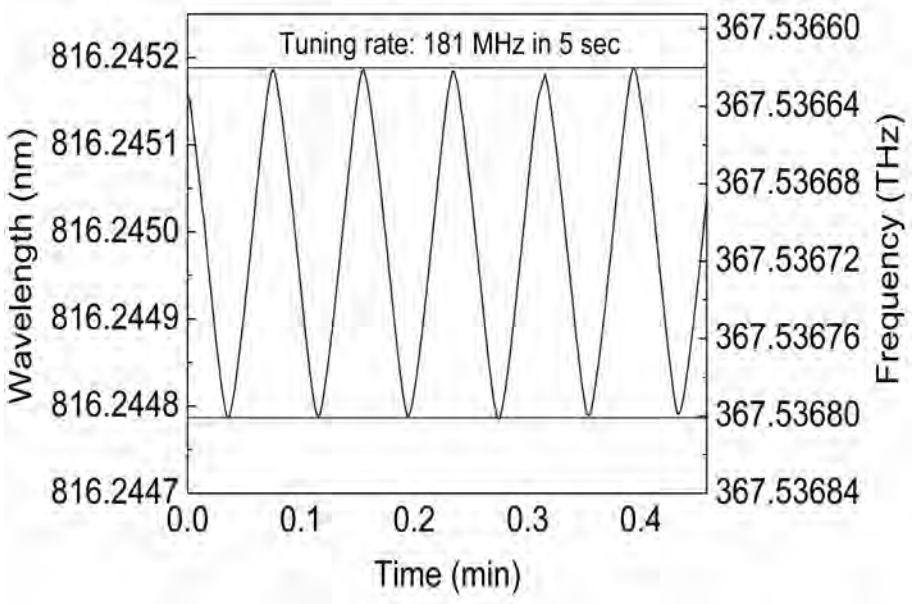

Figure 8.17: Continuous tuning of the Ti:sapphire ring laser at 816 nm at a rate of 181 MHz in 5 sec.

require continuous tunability about a certain wavelength. By applying a voltage on the second piezo of our Fabry-Perot interferometer, we obtain a fine-tuning of the mirror-spacing that allows us to smoothly adjust the frequency corresponding to the maximum of a transmission peak, hence the frequency of the stabilized laser. In order to demonstrate the potential of the fiber-based green source pumped Ti:sapphire ring laser for such practical applications, we applied a sinusoidal signal to the second piezo of the interferometer and recorded the output wavelength of the stabilized Ti:sapphire laser with the wavemeter. We then checked the continuous tuning of the output wavelength over 181 MHz (corresponding to mode-hop-free tuning of our laser) in 5 seconds, yet maintaining the frequency stable operation, as shown in Fig. 8.17.

8.4.5 Power stability and beam quality

In order to completely characterize the Ti:sapphire ring laser, we investigated the power stability of the output by recording the variation of the output power with

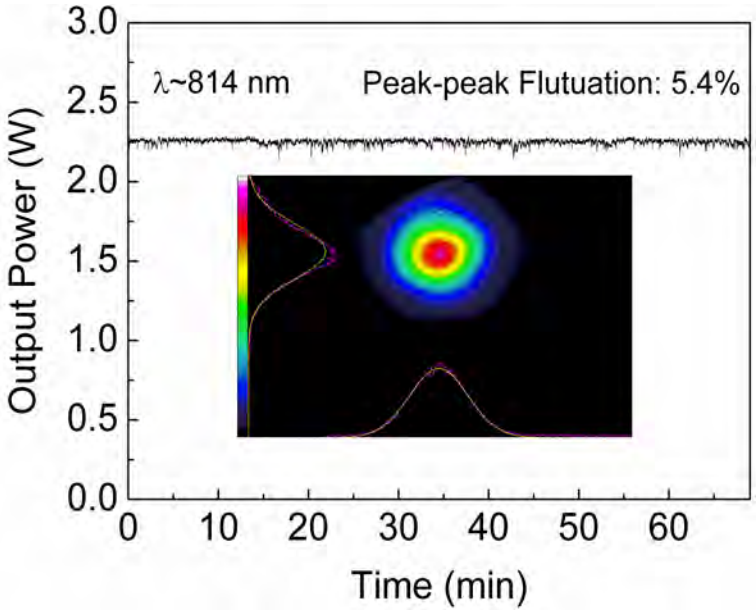

Figure 8.18: Power stability of the Ti:sapphire output at 2.25 W recorded over a period of 75 mins. Inset: Far-field energy distribution of the Ti:sapphire ring laser output beam at 812 nm.

time. Figure 8.18 shows the long-term power stability of the Ti:sapphire output at a wavelength of 814 nm recorded at a maximum output power of 2.2 W. The peak-peak power fluctuation is measured to be 5.4% over more than 75 minutes, which compares to that of the fiber-based green source, which is 3.3% over 1 hour. The power stability can be further improved by providing proper isolation from the mechanical vibration and air turbulence in the laboratory environment. Also shown in the inset of Fig. 8.18 is the far-field energy distribution of the Ti:sapphire output at 812 nm recorded at a distance of >2 m, together with the intensity profiles and the Gaussian fits at the maximum output power. Using a scanning beam profiler and a focusing lens, we measured the M^2beam quality factor, of the output beam. The measurement resulted in a value of M_x^2~1.22 and M_y^2~1.34, confirming the Gaussian nature of the output beam.

8.5 Conclusions

In this chapter, we have demonstrated that a high-power, cw, single-frequency, green source based on single-pass SHG of a Yb-fiber laser in MgO:sPPLT nonlinear crystal is a viable alternative to pump a cw Ti:sapphire ring laser. Careful design and optimization of the Ti:sapphire ring laser provided as much as 2.25 W of single-frequency output power at 812 nm for an incident green pump power of 11.3 W with a slope efficiency of 33.7% and an instantaneous linewidth of 5.4 MHz. The laser is coarsely tunable over 47 nm, from 774 nm to 821 nm, limited by the cavity optics, and maintains single-frequency operation over the entire tuning range. We have actively stabilized the Ti:sapphire ring laser to an external reference provided by a specifically designed ultra-stable Fabry-Perot interferometer. The resulting frequency stability is better than 12 MHz over 10 minutes and the laser is continuously tunable over 181 MHz in 5 sec. Moreover, a measured peak-peak power fluctuation of 5.4% over more than one hour at the maximum output power for a wavelength of 812 nm, in high spatial beam quality with M^2<1.34, proves the fiber-laser-based green source as a robust, reliable and competitive pump source for the near-infrared spectral region.

9 Single-pass multicrystal second harmonic generation

This chapter constitutes the following publications:

1. *High-efficiency, multicrystal, single-pass, continuous-wave second harmonic generation*
   S Chaitanya Kumar, G K Samanta, K. Devi, and M Ebrahim-Zadeh
   Optics Express **19**, 11152–11169 (2011).

2. *Multicrystal, continuous-wave, single-pass second-harmonic generation with 56% efficiency*
   G. K. Samanta, **S. Chaitanya Kumar**, K. Devi, and Majid Ebrahim-Zadeh
   Optics Letters **35**, 3513–3515 (2010).

9.1 Motivation

Single-pass second-harmonic-generation (SP-SHG) of continuous-wave (cw) solid-state lasers near 1 μm in quasi-phase-matched (QPM) ferroelectric crystals has recently been shown to be an attractive approach for the generation of high-power green radiation of high beam quality, offering simple, compact and low cost architecture [121, 123, 122, 40]. Vital in the attainment of practical powers and efficiencies in this scheme is the exploitation of long interaction lengths under noncritical phase-matching (NCPM) together with the high optical nonlinearity offered by QPM

materials. Among all existing QPM materials, MgO:sPPLT has been demonstrated to be most promising material for high-power green generation its high photorefractive damage threshold. Using a 20 mm crystal, a cw SP-SHG efficiency of 35% was achieved into the green for a pump power of 19.6 W [121], while 24.4% efficiency was obtained with a 40 mm PPLT crystal at a high fundamental power of 75 W [123]. Using a pump power of 100 W, a cw SP-SHG efficiency of 17% was also reported in a 10-mm-long MgO:sPPLT crystal [123]. We also recently achieved 33% efficiency in cw SP-SHG of a 30 W Yb fiber laser with a 30-mm-long MgO:sPPLT crystal, generating 9.6 W of green power at 532 nm [40]. While at high fundamental powers (>10 W), short interaction lengths can be tolerated to provide practical cw power at reduced efficiency, at low to moderate powers (<10 W) longest interaction lengths must be used to achieve maximum cw SP-SHG efficiency and power. In practice, however, the maximum available interaction length in QPM crystals is limited by material growth and fabrication technology (30-40 mm in MgO:sPPLT). To improve efficiency, double- or multi-pass [124, 125] pumping has been used to increase the effective interaction length, but the need for phase control in the return pass, increased thermal loading and damage risk in the same crystal are limitations of this approach.

In this chapter, we present a simple approach for the attainment of highest conversion efficiency and output power in cw SP-SHG using multiple nonlinear crystals in cascade, and compare the performance characteristics with regard to the most important parameters including SHG power and efficiency, from single-crystal to multicrystal scheme. The optimization of various critical parameters including mode-matching and focusing, phase-matching temperature and pump depletion at the output of each individual stage to maximize SHG efficiency is discussed in detail. Also, the effect of crystal housing configuration on SHG efficiency is studied. Using this technique, we demonstrate an increase in cw SP-SHG efficiency by ∼4 times from the single-crystal (SC) to double-crystal (DC) scheme in the high-power

regime, providing 13 W of green power at an overall efficiency of 51.8 % for 25.1 W of fundamental power. Using multicrystal (MC) scheme involving three crystals, we further enhance the cw SP-SHG efficiency by ∼8 times in the low- to moderate-power regime compared to SC scheme, generating 5.6 W of green power for 10 W of fundamental power at an overall efficiency as high as 56%. Relevant theoretical calculations are presented to estimate the effect of dispersion between the fundamental and the SH beam while traversing between the successive stages in the MC scheme. The quasi-cw measurements illuminate the role of thermal effects and SHG efficiency roll-off, which such systems involving high optical powers are known to exhibit. To our knowledge, the conversion efficiency of 56% is the highest in cw SP-SHG achieved to date, using bulk QPM or birefringent nonlinear crystals. Moreover, the described technique is generic, and can be extended to more than three crystals in a cascade to achieve the highest overall cw SP-SHG efficiency and output power for any given input fundamental power. Combined with the rapid advances in cw Yb fiber lasers, the approach offers a highly effective route for the realization of simplified, compact, efficient, and cost-effective green sources from a few watts to several watts of output power.

9.2 Experimental setup

The schematic of experimental configuration for the MC cw SP-SHG experiments is shown in Fig. 9.1. The fundamental pump source is a cw Yb fiber laser (IPG Photonics, YLR-30-1064-LP-SF) delivering linearly polarized single-frequency radiation at 1064 nm with a maximum output power of 30 W and a nominal linewidth of 89 kHz and M^2<1.01, the same as that used in the previous experiments. In order to maintain stable output characteristics, the fiber laser is operated at maximum power and the input power to the SHG crystal is adjusted by using a combination of half-wave plate and polarizing beamsplitter cube. A second half-wave plate is used to obtain the correct polarization for phase-matched SHG in the nonlinear crystal.

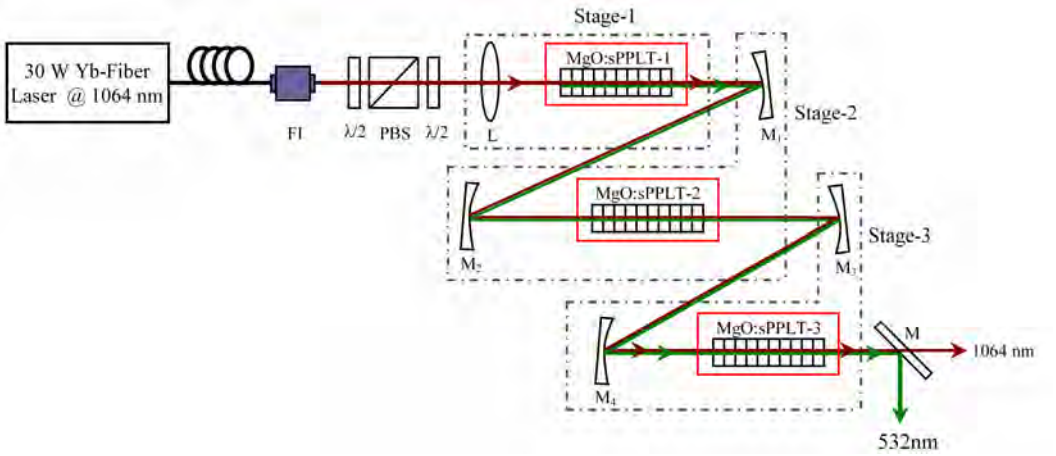

Figure 9.1: Schematic experimental setup for the multicrystal cw single-pass SHG.

We use three identical MgO:sPPLT crystals, each 30-mm-long, 2-mm-wide and 1-mm-thick, and containing a single grating period of Λ=7.97 μm. The end faces of all three crystals are antireflection-coated (R<1%) at 1064 nm and 532 nm. Each crystal is housed in a separate oven with temperature stability better than ±0.1 °C. Our earlier studies on nonlinear crystal housing configurations discussed in chapter 8, has revealed that a significant improvement in the SHG efficiency can be obtained by proper design of the mount for the crystal, to provide efficient thermal management. Using two different oven designs for the crystal, we have found a significant difference in the generated green power and cw SP-SHG conversion efficiency between the two configurations. The two crystal housing configurations, open-top (OT) and close-top (CT), are the same as those shown in Fig. 8.4 of chapter 8. The OT configuration resulted in better performance, due to the easier exchange of heat between the nonlinear crystal and the ambient air, permitting the optimum phase-matching to be achieved and maintained. The MC SP-SHG setup consists of three stages. In stage-1, the fundamental beam is focused into the nonlinear crystal using a lens of focal length f=175 mm, resulting in a beam waist radius of w_1∼31 μm, positioned at the center of the crystal. In stage-2, the generated SH and undepleted fundamental from stage-1 are collimated using a plano-concave mirror, M_1, and refocused into the

second crystal using M_2. The SH thus generated, and the un-depleted fundamental are again collimated and refocused by using plano-concave mirrors, M_3 and M_4, into the third crystal in stage-3. The radius of curvature of all mirrors, $M_1 - M_4$, are chosen according to the required beam waist for mode-matching at the center of each crystal. The angle of incidence on each mirror is limited by the mechanical constraints and kept as small as possible. All plano-concave mirrors are coated for high reflectivity (R>99%) at 1064 nm and 532 nm, and are mounted on translation stages, so as to adjust the inter-crystal spacing, to compensate for the accumulated phase due to dispersion in air, if there is any. A plane dichroic mirror, M, coated for high reflectivity (R>99%) at 532 nm and high transmission (T>99%) at 1064 nm, is used to extract the generated green output from the fundamental. Unlike lenses [126], using plano-concave mirrors to collimate and refocus the beams into the successive stages, avoids any additional phase retardation issues between the fundamental and SH wavelengths due to material dispersion.

9.3 Single-crystal cw single-pass SHG

In order to achieve efficient SHG, we systematically characterized the setup in DC and then in MC schemes and the results thus obtained were compared to evaluate the performance. A complete characterization of cw SP-SHG in SC scheme based on MgO:sPPLT was performed and discussed in chapter 8, where the temperature phase-matching properties were studied in detail. The SC cw SHG was characterized by focusing the fundamental beam to a waist radius of $w_1 \sim 31\ \mu m$ inside a 30-mm-long MgO:sPPLT crystal housed in an oven in the CT configuration. The temperature acceptance bandwidth was measured to be 1.3 °C, centered at a phase-matching temperature of 52 °C. Using a single MgO:sPPLT crystal in the CT oven configuration, we generated 7.8 W of green for a fundamental power of 29.5 W at a cw SP-SHG efficiency of 26.4%, while by employing the OT design we improved the green power to 9.6 W at 32.7% conversion efficiency for the same input fundamental

power.

9.4 Double-crystal cw single-pass SHG

The DC cw SP-SHG setup is characterized by focusing the SH green and the undepleted fundamental from stage-1 into the second identical MgO:sPPLT crystal by a proper choice of M_1 and M_2. The net physical length of the nonlinear crystal in DC scheme is 60 mm (2 × 30 mm). The second crystal is initially mounted in the CT housing configuration. In order to scale the SHG efficiency, radius of curvature of M_1 and M_2 are chosen to be r=150 mm, such that a mirror image of the beam waist in the first crystal is formed at the center of the second crystal, resulting in a beam waist radius of w_2∼30 μm. The fundamental power is measured before stage-1 and the SH power is measured after stage-2 for scaling. The SHG efficiency scaling results under this focusing condition are shown in Fig. 9.2(a). The SHG efficiency increases linearly up to a fundamental power of 7 W, above which saturation behavior is observed. A maximum efficiency of 48.5% is achieved at a fundamental power of 20.4 W. Further increase in the fundamental power resulted in catastrophic damage of the second crystal. The origin of this damage could be attributed to the strong focusing of both the fundamental as well as the SH beam, or poor quality of the crystal sample used in stage-2. Further experiments are needed to understand this damage phenomenon in detail. In order to avoid the damage, we replaced M_2 with another mirror of longer radius of curvature, r=250 mm, resulting in beam waist radius of w_2∼46 μm at the center of the second crystal and performed SHG efficiency scaling measurements, the results of which are also shown in Fig. 9.2(a). The stage-2 is maintained at a distance of ∼37 cm from stage-1. The SHG efficiency in case of w_2∼46 μm follows that at w_2∼30 μm very closely at low fundamental power level. Although saturation is observed under both focusing conditions, the maximum achievable SHG efficiency increased to 50.7% for a fundamental power of 18.4 W at the input of stage-1. To investigate the role of crystal mounting configurations, we

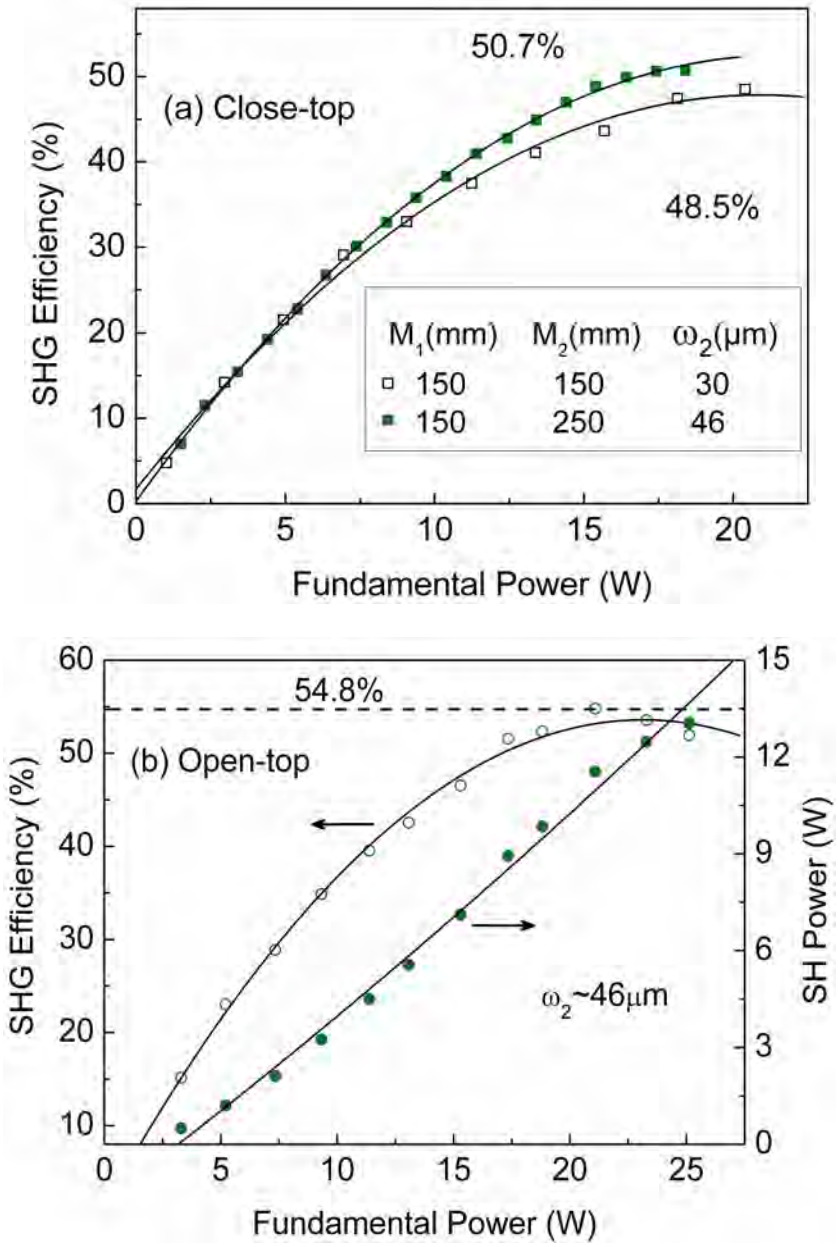

Figure 9.2: (a) Variation of SHG efficiency as function of fundamental power for a beam waist radius of w_2∼30 μm and 46 μm in CT configuration, (b) SH power and efficiency scaling for a beam waist radius of w_2∼46 μm in OT configuration.

performed SHG power and efficiency scaling measurements in the OT design for the same beam waist of w_2∼46 μm in the second crystal, with the results shown in Fig. 9.2(b). Using the OT configuration, maximum SHG efficiency as high as 54.8% is achieved with a SH power of 11.6 W for a fundamental power of 21.1 W, confirming the better performance of OT configuration. It is also to be noted that we were able to use an input fundamental power greater than 20 W without any catastrophic damage to the second crystal, generating as much as 13 W of green power for a fundamental power of 25.1W. However, the SHG efficiency roll-off occurs when the fundamental power increased above 21.1 W. Having achieved SHG efficiency as high as 54.8% in the DC scheme, we extend this technique to one more stage, by deploying a third crystal in the cascade, to further increase the SHG efficiency and power.

9.5 Multicrystal cw single-pass SHG

The MC cw SP-SHG scheme is realized by focusing the SH green as well as the undepleted fundamental from the output of the DC scheme into a third crystal by using another pair of plano-concave mirrors, M_3 and M_4. A laboratory picture of the MC SP-SHG setup is shown in Fig. 9.3. The net physical length of the nonlinear crystal in the MC scheme is 90 mm (3 × 30 mm). Efficient mode-matching, proper choice of the confocal focusing parameter, and careful control of the pump depletion, enables the exploitation of the maximum effective interaction length to achieve highest SHG efficiency. The radius of curvature of M_3 and M_4 are chosen to be r=150 mm and r=100 mm, respectively, resulting in a beam waist radius of w_3∼40 μm at the center of the third MgO:sPPLT crystal. The stage-3 is separated by a distance of ∼86.5 cm from stage-2. The MC SP-SHG is characterized using the CT oven configuration for stage-1 and stage-2, while employing the OT design for stage-3, where the nonlinear crystal is expected to suffer maximum thermal effects. The SHG efficiency scaling results at the output of each stage in the MC scheme are shown in Fig. 9.4(a). For this measurement, the phase-matching temperature of each of the three crystals is

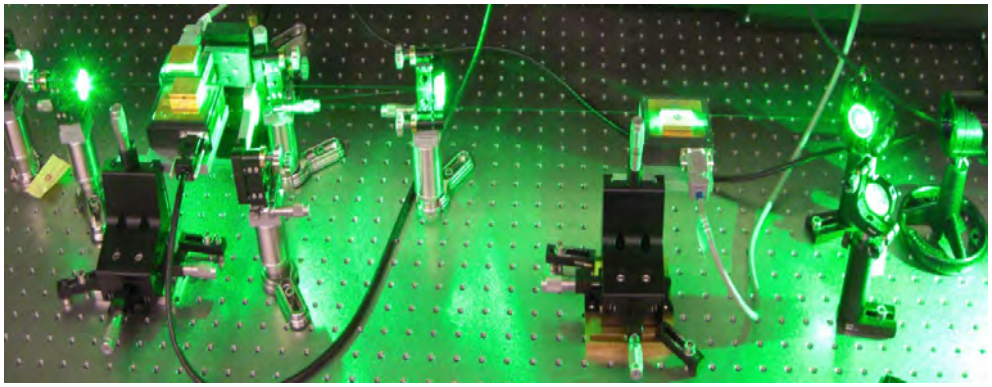

Figure 9.3: Practical MC SP-SHG setup in the laboratory.

adjusted every time the fundamental power is increased, so as to achieve maximum overall SH green power at the output of stage-3. The input fundamental power is measured before stage-1, while the green power is measured at the output of the respective stages. The SH power in MC scheme at the output of stage-3 increases quadratically up to a fundamental power of 10 W, providing a maximum green power of 5.6 W at a maximum SHG efficiency of 56%. Further increase in the fundamental power up to 12 W results in saturation of SH power, leading to efficiency roll-off. We attribute this behavior to thermal phase-mismatch effects, back-conversion and pump depletion. These issues are discussed in section 9.7. The corresponding maximum SHG efficiencies, measured at the output of stage-1 and stage-2 are 11.2% and 36.2%, respectively, which are not necessarily the maximum achievable efficiencies for the respective stages. These values at a similar fundamental power level are lower than the SHG efficiencies achieved in the SC (17.5%) and DC (42.3%) schemes. It is to be noted that the optimization procedure for SC and MC schemes is different. In case of SC scheme, we obtained maximum green power by operating the crystal at its phase-matching temperature. On the other hand, if we keep all the crystals at their respective phase-matching temperatures in MC scheme, the overall green power is low. This is obvious as higher depletion of the fundamental power in one stage reduces the fundamental power to get depleted in the succeeding stages thereby lowering the overall efficiency. Hence, while optimizing the MC scheme for maximum SH

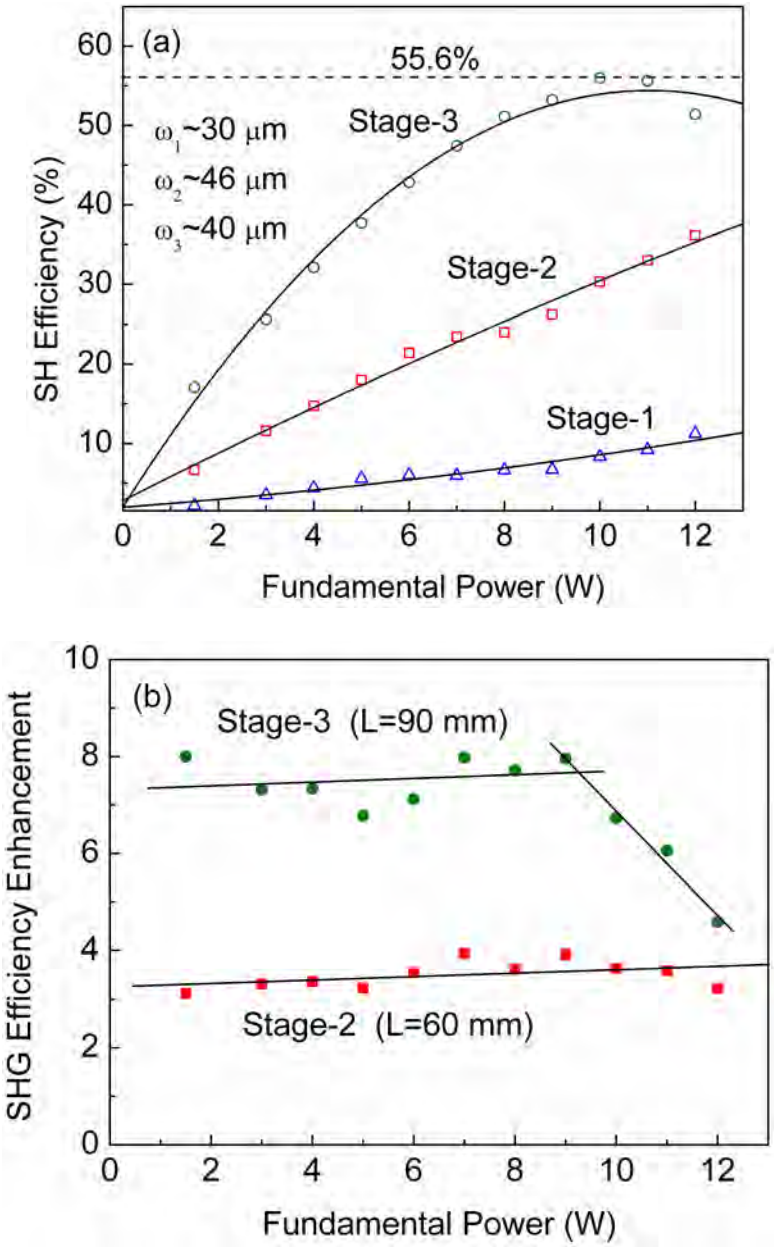

Figure 9.4: Variation of (a) SHG efficiency and (b) SHG efficiency enhancement factor, as a function of fundamental power at the different stages in the MC SHG scheme for w_1∼30 μm, w_2∼46 μm, w_3∼40 μm.

power at the output of stage-3, we slightly detuned the temperature of the crystals in stage-1 and stage-2 from their phase-matching temperature, as a result of which the generated green power at the output of stage-1 and stage-2 in the MC scheme is not optimum, however a clear enhancement in the overall SHG efficiency is recorded in the MC scheme, as shown in Fig. 9.4(a). The detuning of the phase-matching temperature in the MC scheme permits the control of pump depletion and SH power in each conversion stage, as well as the distribution of thermal load in the different crystals, resulting in maximum overall SHG efficiency and output power. This freedom also has the additional advantage of reducing the risk of optical damage in each crystal. The flexibility of controlling the phase-matching temperature in different conversion stages is one of the greatest advantages of the MC SP-SHG scheme, particularly in the high-power regime. This is the reason why perfect phase control due to the air dispersion is not required. Therefore, any slight phase shift between the fundamental and SH due to dispersion in air can be compensated by controlling the pump depletion. As the SHG efficiency scales quadratically with the length of the nonlinear crystal, an efficiency enhancement factor of 4 and 9 is expected at the output of stage-2 (L=60 mm) and stage-3 (L=90 mm), respectively, in comparison with stage-1(L=30 mm). So, we also compared the SHG efficiency enhancement at the output of stage-2 and stage-3 with respect to stage-1, up to a fundamental power of 12 W, as shown in Fig. 9.4(b). It can be seen that the measured SHG efficiency resulted in an enhancement of ∼4 times after stage-2, as expected, while there appears to be a slight deviation after stage-3, with a recorded value of ∼8 times up to a fundamental power of 9 W, above which it decreases linearly to ∼4.6 times at 12 W of fundamental power. This decrease in the SHG efficiency enhancement factor is attributed to the efficiency roll-off due to thermal phase-mismatch effects, back-conversion, and pump depletion.

In order to investigate the role of focusing in stage-3, we used a different set of plano-concave mirrors for M_3 and M_4, with r=150 mm and r=200 mm, respectively,

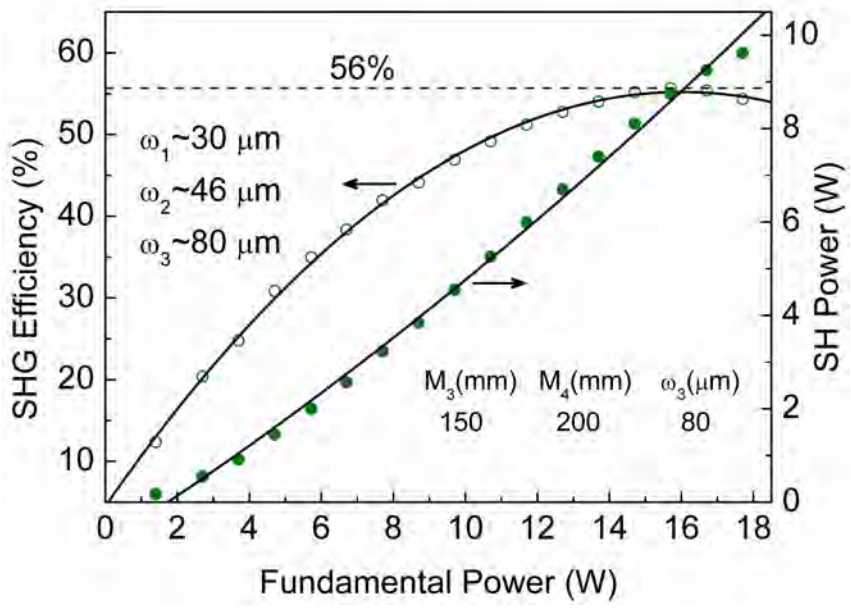

Figure 9.5: Power scaling of MC SHG scheme with w_3∼80 μm.

resulting a beam waist radius of w_3∼80 μm at the center of the third MgO:sPPLT crystal. The power scaling results for the MC scheme with w_3∼80 μm in the third crystal are shown in Fig. 9.5, where it can be seen that loose focusing enabled pumping up to a higher fundamental power level of 17.7 W, providing a maximum SH power of 9.6 W at an efficiency of 54.3%. However, the maximum efficiency achieved still remains 55.6% at a fundamental power of 15.7 W. Hence, depending on the available pump power, the maximum SH power or the maximum efficiency can be achieved by proper choice of the focusing condition as well as length of the nonlinear crystals in the MC scheme.

Further, we compare the performance of all three schemes, with the power scaling results shown in Fig. 9.6(a). In the MC scheme, a maximum green power of 6.1 W is achieved for a fundamental power of 11 W at an SHG efficiency of 55.5%. The corresponding SH power generated in the SC, DC schemes are 9.6 W and 13 W, respectively. The maximum SH power generated in the MC scheme is limited by the SHG efficiency roll-off. Importantly, SHG efficiency as high as 56% is achieved for a fundamental power as low as 10 W in the MC scheme, while achieving a SHG

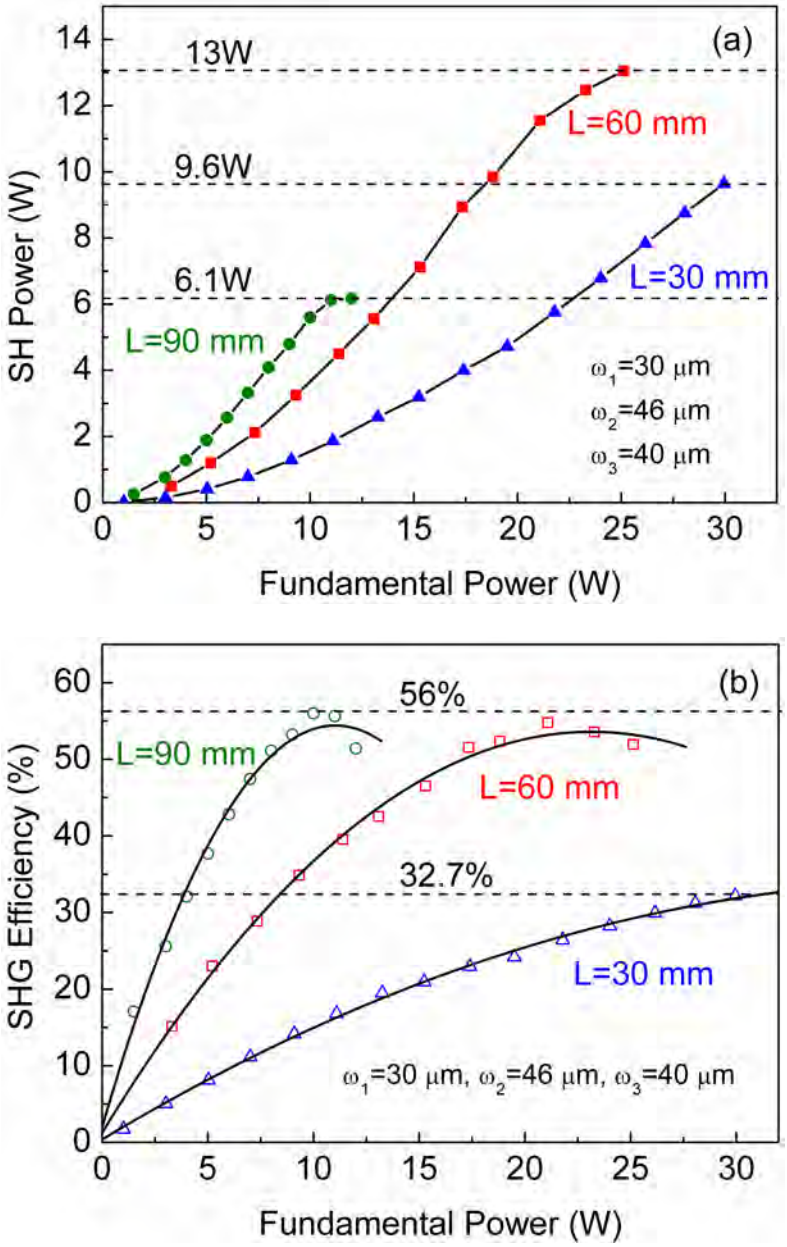

Figure 9.6: Comparison of (a) SH power scaling, and (b) SHG efficiency in SC, DC, and MC schemes.

efficiency of 54.8% in the DC scheme requires 21.1 W of fundamental power, as evident in Fig. 9.6(b). These values of the required fundamental power are in close agreement with the theoretical estimates made from Fig. 2.7. Clearly, the required fundamental power to achieve similar maximum SHG efficiency reduces by ∼2 times (or 50%) in the MC scheme as compared to DC scheme, while such efficiency could not be achieved in the SC scheme using a single 30-mm-long MgO:sPPLT crystal with the available 30 W fundamental power, as evident from Fig. 9.6(b). The corresponding low-power normalized conversion efficiencies are 1.4 %/W, 5 %/W and 7.8 %/W for the SC, DC and MC scheme, respectively.

9.6 Effect of dispersion in air

In order to study the effect of the inter-crystal spacing on the SHG efficiency enhancement due to of the phase accumulation between the fundamental and the SH, arising from the dispersion in air in the DC scheme, we used the formalism developed by G.C. Bhar et al. [128]. Any additional phase accumulation due to the mirrors is also accounted for. Considering an experimentally measured SH efficiency enhancement factor of 3.8 for a separation of 37 cm between the two stages in the DC scheme, we estimated a relative phase accumulation of $\Delta\varphi$=17.4 radians due to the mirrors. With this estimate of $\Delta\varphi$, we investigated the effect of inter-crystal spacing on the SHG efficiency. The calculated variation of the SHG efficiency enhancement factor as a function of inter-crystal spacing in the DC scheme is shown in Fig. 9.7. For this calculation, we used a linear absorption coefficient of 0.17 %/cm, 1.57 %/cm for MgO:sPPLT crystal at the fundamental and the SH wavelengths, respectively [41]. The phase shift of 27.4°/cm between the fundamental and the SH waves due to dispersion in air is assumed. As evident from Fig. 9.7, a considerable change in the SHG efficiency enhancement requires the distance between the crystals to be varied by few centimeters. The vertical dashed line in Fig. 9.7 represents the SHG efficiency enhancement for a distance of 37 cm between the crystals, which we

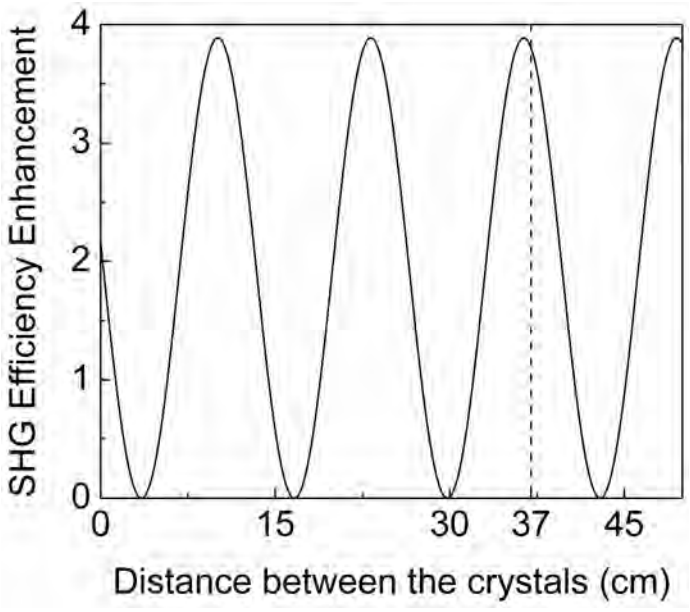

Figure 9.7: Theoretically calculated variation of the SHG efficiency enhancement factor as a function of the distance between the crystals in DC scheme for $\Delta\varphi$=17.4 radians.

used in the present experiment for the DC scheme. This distance is very close to the optimum separation which can provide a theoretical maximum SHG efficiency enhancement.

9.7 Thermal effects and SHG efficiency roll-off

In order to study the role of thermal effects in the MC cw SP-SHG scheme, we performed temperature tuning measurements in stage-3, where the heaviest thermal load is expected due to the highest SH power, since the residual absorption of the crystal is ∼9 times higher at 532 nm than at 1064 nm. While performing these measurements, stage-1 and stage-2 are optimized for maximum SH power. The dependence of the normalized SH power on the temperature of the nonlinear crystal in stage-3 at a fundamental power of 11 W is shown in Fig. 9.8(a). It is to be noted that a non-zero SH power is measured even when the stage-3 is completely out of phase-matching because of the contribution from stage-1 and stage-2. The

solid curve is the $sinc^2$ fit to the data, which has a full-width at half maximum (FWHM) bandwidth of ΔT=1.3 °C at a phase-matching temperature of 50.9 °C. This is slightly wider than the theoretically calculated value of ΔT=0.96 °C for a 30-mm-long MgO:sPPLT crystal using the Sellmeier equations for the material [57]. The temperature acceptance bandwidth is similar to that measured in the SC scheme [40, 41]. The discrepancy between the calculated and measured temperature acceptance bandwidth values arises from various factors including focusing, possible non-uniformity of the grating period, and thermal effects. A wider temperature acceptance bandwidth is anticipated for SHG process, because it indicates that the generated SH power is less susceptible to minor temperature fluctuations about the phase-matching temperature. As the temperature acceptance bandwidth is inversely proportional to the length of the nonlinear crystal, employing a single 90-mm-long MgO:sPPLT crystal would result in a ΔT=0.32 °C, which is 3 times lower than that for a 30-mm-long crystal. However, by deploying the MC SHG scheme, we can exploit the advantage of a much longer total interaction length, but without incurring the penalty for a reduced temperature acceptance bandwidth. This would also be true for spectral acceptance bandwidth. Additionally, since the beam focusing condition in the MC scheme can be independently controlled for each stage, one can achieve a similar angular acceptance bandwidth for the total number of crystals in the cascade as for a single crystal.

The rate of change of phase-matching temperature with respect to fundamental power up to 16 W, in all the three schemes, is shown in Fig. 9.8(b). The phase-matching temperature in the SC scheme decreases from 50.6 °C to 49.7 °C at a rate of 0.06 °C/W. In the DC scheme, while the phase-matching temperature of the nonlinear crystal in stage-1 is optimized for maximum SH power, the phase-matching temperature of stage-2 decreases from 52 °C to 50.8 °C at a rate of 0.08 °C/W. Similarly, with the phase-matching temperature of stage-1 and stage-2 optimized for maximum SH power, the phase-matching temperature of stage-3 in MC scheme

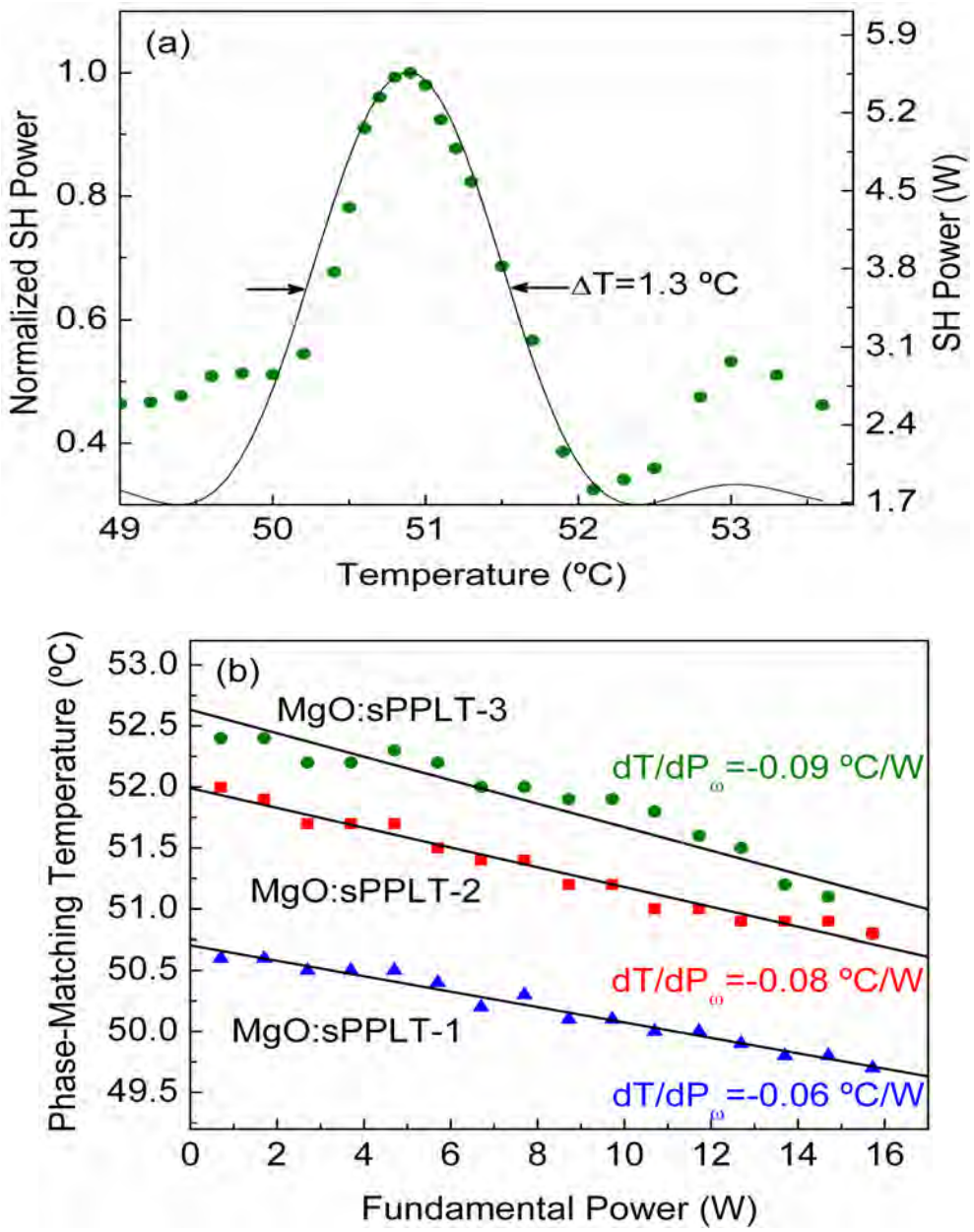

Figure 9.8: (a) Temperature acceptance bandwidth of the third crystal, and (b) Change in phase-matching temperature as a function of fundamental power in SC, DC and MC schemes.

decreases from 52.4 °C to 50.8 °C at a rate of 0.09 °C/W. This value in the MC SHG scheme is similar to that of PPKTP in the SC scheme, also measured up to a fundamental power level of 16.4 W [41], indicating the superior performance of MgO:sPPLT due to its high thermal conductivity. Further, owing to the fact that the absorption coefficient of MgO:sPPLT crystal at 532 nm (1.57 %/cm) is ∼9 times higher than that at 1064 nm (0.17 %/cm), it is expected that the crystal in the third stage is prone to the heaviest thermal load. However, as the length of the nonlinear crystal increases, which in the present case is achieved by using multiple crystals, the amount of fundamental power required to attain the maximum SHG efficiency before the onset of any roll-off decreases rapidly, not only reducing the thermal effects due to absorption of fundamental by 3 times in the MC scheme as compared to the SC scheme, but also distributes the thermal load due to the SH wavelength in all three stages. This thermal management can be seen as one of the main advantages of the MC scheme, which is very difficult in a single long crystal, in addition to the possibility of achieving high SHG efficiencies. In order to verify the contribution of thermal effects to SHG efficiency roll-off, we chopped the fundamental beam at a frequency of 510 Hz, with a 5.1% duty cycle, and performed power scaling measurements in DC and MC schemes, separately. The quasi-cw SH power and efficiency scaling results are shown in Fig. 9.9(a)-(b). The generated average SH power in the DC scheme reaches a maximum of 0.6 W for an average fundamental power of 1.3 W at a SHG efficiency of 48.9%, as can be seen from Fig. 9.9(a). Similar measurement for pure cw pumping resulted in a SHG efficiency of 54.8%, as shown in Fig. 9.2(b). In MC scheme, a maximum average SH power of 0.4 W is generated for an average fundamental power of 0.7 W at a SHG efficiency of 55%, above which SH power saturation and efficiency roll-off sets in, as evident from Fig. 9.9(b). The maximum SHG efficiency achieved by quasi-cw pumping is similar to that achieved by pure cw pumping (56%, as shown in Fig. 9.6(b)), indicating minimal contribution of thermal effects to SHG efficiency roll-off in MC scheme, leaving pump depletion

as a possible reason.

9.8 Power stability and output beam quality

In order to completely characterize the MC cw SP-SHG scheme, we have measured the power stability and beam quality of the SH beam at the output of stage-3. The power stability of the SH output beam is influenced by various factors such as power stability of the fundamental, fluctuations in the temperature of the nonlinear crystal, air currents and mechanical vibrations in the laboratory environment. The power stability of the Yb fiber laser fundamental beam is measured to be better than 1% over 65 minutes and the SH beam at the output of the SC scheme was measured to be better than 2.2 % over 1 hour, as presented in the previous chapter, which has been achieved by using a more uniform heating configuration for the MgO:sPPLT crystal, where the 30-mm crystal is placed at the center of a large-area oven for heating. As compared to the small-area oven, the central part of the large-area oven has better temperature uniformity and is less sensitive to the instability (±0.1 °C) determined by the temperature controller. As a result, the large-area oven maintains improved temperature stability across the full length of the crystal, and hence a better green output power stability. Due to the limited availability of large-area ovens in our laboratory, they are only deployed in stage-1 and stage-2 of the MC SHG scheme, while stage-3 uses a small-area oven. Figure 9.10 shows the green power stability measurement at the output of the MC scheme at a SH power of 5.5 W and a SHG efficiency of 55%, resulting in a peak-to-peak fluctuation of 6.5% over >2 hours. We have also recorded long-term peak-to-peak power stability better than 10.5% over 10 hours. Further improvement in the SH power stability is possible by incorporating the entire MC SHG setup in a mono-block, thereby minimizing the influence of air currents and mechanical vibrations. Further, we have also characterized the SH beam quality at the output of the MC SP-SHG setup. The inset of Fig. 9.10 shows the far-field energy distribution of the SH green beam, as measured at an

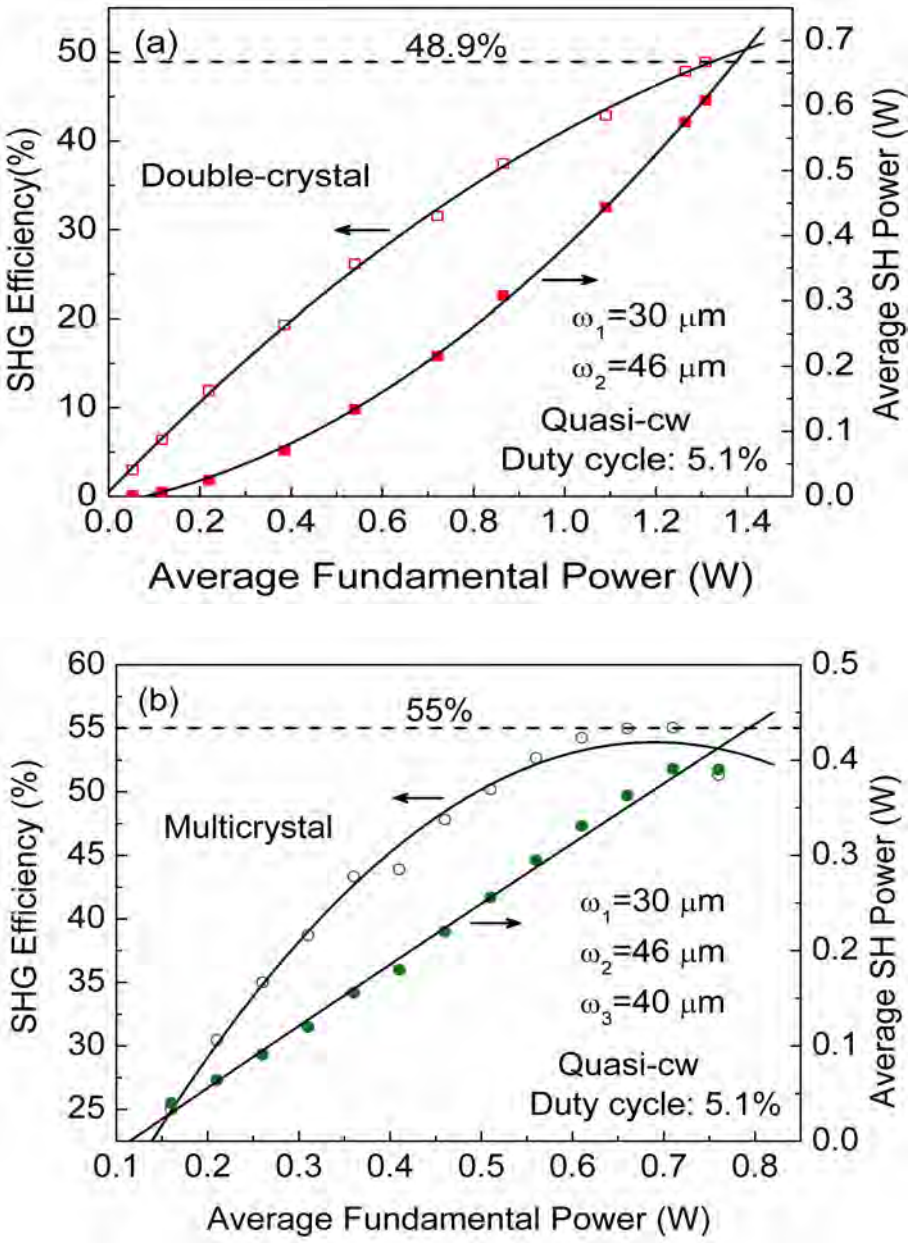

Figure 9.9: Quasi-cw power scaling of (a) double-crystal, and (b) multicrystal schemes.

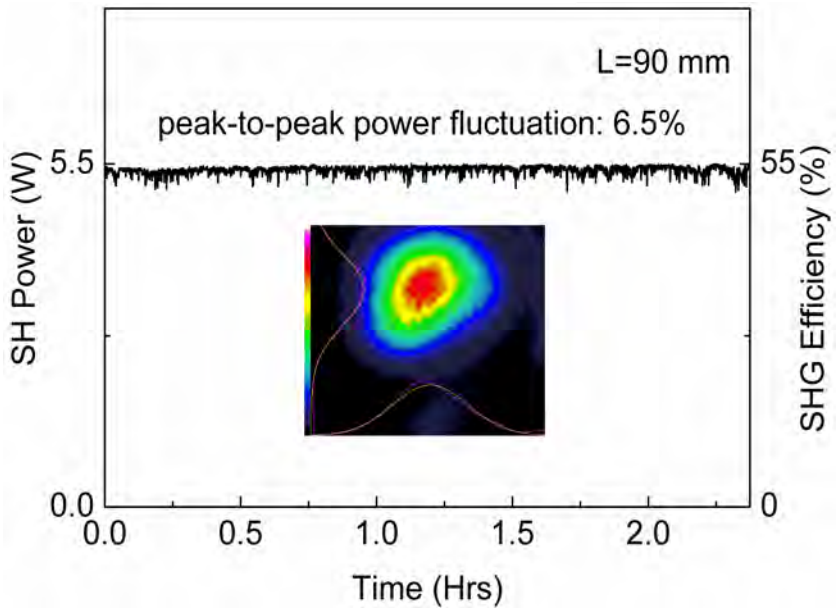

Figure 9.10: Second harmonic power stability at the output of MC scheme.

incident fundamental power of 11 W and maximum SHG efficiency, together with the horizontal and vertical intensity profiles, confirming a Gaussian beam profile. The slight asymmetry in the beam profile may be attributed to the number of plano-concave mirrors used at a small angle away from normal incidence in the MC scheme, and so could be overcome by further design improvements to reduce the angles of incidence on the focusing mirrors. Using a scanning beam profiler and a f=20 cm focal length lens, we measured the beam diameter over the Rayleigh range of the focused SH beam at the output of the MC SHG setup, and determined the corresponding M^2 values in the horizontal and vertical directions. This measurement was performed at a SHG efficiency of 55% and resulted in a value of M_x^2~1.6 and M_y^2~1.34. These values are comparable to M_x^2~1.6 and M_y^2~1.52 measured in the DC scheme at a SHG efficiency of 50%, and M_x^2~1.29 and M_y^2~1.23 in the SC scheme at a SHG efficiency of 32.7%, confirming TEM_{00} spatial mode in the MC scheme.

9.9 Conclusions

In this chapter, we have presented detailed studies of a novel multicrystal scheme for efficient SP-SHG of cw laser radiation. Using a cw Yb fiber laser in combination with three MgO:sPPLT nonlinear crystals, record cw SHG efficiencies as high as 54.8% and 56% into the green have been achieved, for fundamental powers of 21.1 W and 10 W, in DC and MC schemes, respectively, and the efficiencies have been found to be in close agreement with the theoretical estimates. The optimization of various vital parameters including focusing and phase-matching temperature at the output of each individual stage to maximize the SHG efficiency has been investigated. The SC, DC and MC SHG schemes have been systematically characterized and their results compared, as summarized in Table 9.1. By employing different oven designs, the OT configuration enabled pumping at high fundamental power levels, thus permitting higher SHG efficiencies. We have observed SHG efficiency roll-off in DC and MC schemes, irrespective of the oven design and focusing conditions. In the MC scheme, although the maximum SHG efficiency achieved is similar (56%), loose focusing in the third crystal (w_3∼80 μm) not only postponed the SHG efficiency roll-off, but also allowed pumping to a higher fundamental power of 17.7 W, resulting in a maximum SH power as high as 9.6 W, while focusing to w_3∼40 μm resulted in a SH power of 6.1 W only at a fundamental power of 11 W. We have also recorded a SHG efficiency enhancement factor of ∼4 and ∼8 up to a fundamental power of 12 W and 9 W in stage-2 and stage-3 of MC scheme, respectively. The effect of dispersion between the fundamental and the SH beams in air has been estimated with relevant theoretical calculations, indicating that a substantial change in the SHG efficiency enhancement factor requires variation of the distance between the successive crystals on the order of a few centimeters.

Studies of thermal effects have included measurements of temperature acceptance bandwidth and rate of change of phase-matching temperature with fundamental power. Quasi-cw SHG studies have confirmed minimal contribution of thermal ef-

Scheme →	SC	DC	MC
Crystal length (mm)	30	60	90
Beam waist (μm)	w_1∼30	w_1∼30 w_2∼46	w_1∼30 w_2∼46 w_3∼80
Oven configuration	OT	CT-OT	CT-CT-OT
Highest SHG conversion efficiency (%)	32.7	54.8	56
Low power normalized SH conversion efficiency (%/W)	1.4	5	7.8
M^2 Value	<1.29	<1.6	<1.6

Table 9.1: Summary of multicrystal, single-pass SHG results.

fects to SHG efficiency roll-off in the MC scheme. Further, we have improved the peak-to-peak SH power stability of SC scheme to be better than 2.2% over an hour, by employing large-area oven for uniform heating of the nonlinear crystal and the peak-to-peak SH power stability in MC scheme is recorded to be better than 6.5% over more than 2 hours, and a long-term stability better than 10.5% over 10 hours. This performance has been achieved in high spatial beam quality with M_x^2∼1.6 and M_y^2∼1.34, as compared to M_x^2∼1.6 and M_y^2∼1.52 in a DC scheme, and M_x^2∼1.29 and M_y^2∼1.23 in SC scheme, confirming TEM_{00} mode profile. Further improvement in the stability and spatial beam quality are possible with proper design and optimization without any effect on SH power and efficiency. The generic nature of the multicrystal scheme described here offers a simple yet effective technique for the attainment of maximum SHG efficiency and output power in SP-SHG of cw laser radiation at other wavelengths and over a wide range of fundamental powers.

10 Summary and outlook

In this thesis we have demonstrated optical parametric oscillators (OPO) in continuous wave (cw) as well as ultrafast picosecond time scales spanning the near to mid-infrared spectral range. All the OPOs described in this thesis are configured as singly resonant oscillators (SROs). We also demonstrated nonlinear frequency conversion based on cw single pass SHG as well as pumping Ti:sapphire laser using the fiber based green source.

In the cw regime, we demonstrated three different OPOs based on MgO:PPLN and MgO:sPPLT nonlinear crystals.

- The first device is a stable, high-power, Yb-fiber laser pumped, mid-IR SRO based MgO:PPLN. Output coupling is implemented and optimized to efficiently manage thermal effects by extracting significant amount of signal power from the SRO, making it an output coupled SRO (OC-SRO). The OC-SRO is widely tunable from 1506-1945 nm in the signal wavelength range and 2304-3615 nm in the idler wavelength range, with record output power over the entire tuning range. Using 31 μm grating, the OC-SRO provides 17.5 W of power in the near- to mid-IR at an external efficiency of 61%, with nearly 90% of down-converted pump power extracted as useful output.

- Secondly, we investigated the performance of MgO:sPPLT nonlinear crystal for high-power, cw, mid-IR generation. The SRO is tunable over 430 nm, generating up to 5.5 W of mid-IR power, with >4 W over 60% of the tuning range, and can be operated close to room temperature. This tuning range can be fur-

ther extended using the appropriate grating periods of MgO:sPPLT nonlinear crystal. We also investigate mid-IR power scaling of the device and compare its performance with the well-established MgO:PPLN cw SRO pumped at 1064 nm.

- Thirdly, we demonstrated a cw SRO that can provide broadband radiation in the mid-IR at multiwatt power level, with excellent beam quality, and in a compact and practical design using a fiber laser pump source. Using a 8.3 nm broadband pump radiation, 76 nm broadband mid-IR idler radiation is generated. The SRO generated 5.3 W broadband radiation, while in OC-SRO configuration 4 W of broadband mid-IR radiation along with 7.2 nm of near-IR radiation at 1523 nm was generated. Despite the limitations of low nonlinear gain in the cw regime, by suitably exploiting the extended phase-matching bandwidth in MgO:PPLN, long interaction lengths can be deployed in the presence of a broadband pump to provide broadband mid-IR output with high extraction efficiency from cw OPOs.

In the picoseconds regime, two OPOs based on MgO:PPLN and a new nonlinear crystal, CSP, have been developed.

- In the MgO:PPLN based picosecond ring OPO, the main goal was to demonstrate a novel technique for absolute optimization of output power from ring optical oscillators. The OPO generated as much as 8 W of total (signal + idler) power at θ_{BS}=35° corresponding to an optimum output coupling of ∼48%. The signal output has pulse duration of 17 ps with a spectral width of 1.4 nm centered at 1529 nm. Further, this generic technique is wavelength independent and can be implemented in any type of oscillator.

- The high-energy CSP OPO is the first demonstration of a compact, high-repetition-rate OPO synchronously pumped by a master oscillator power amplifier system at 1064.1 nm, generating an idler energy as high as 1.5 mJ at

6246 nm with a photon conversion efficiency of 29.5%. The OPO is tunable over 486 nm from 6091-6577 nm, with more than 1.2 mJ over >68% of the tuning range in good beam quality. The compact design, high energy, suitable pulse structure, and the potential for energy scaling using larger aperture crystals, make the OPO a promising source for practical surgical applications in the mid-IR .

In the frequency conversion part, for the first time, we have we demonstrate a fiber-based-green source based on single-pass SHG in MgO:sPPLT, as an alternative pump source for Ti:sapphire laser. The cw fiber-laser-based green source pumped, single-frequency Ti:sapphire ring laser generated as much as 2.25 W of output power at 812 nm for an incident green pump power of 11.3 W with a slope efficiency as high as 33.7 %. The actively frequency stabilized Ti:sapphire laser is coarsely tunable over 47 nm, maintaining single-frequency output over the entire tuning range, and is continuously tunable over 181 MHz in 5 sec.

Further efforts were directed towards improving the efficiency of the fiber-based-green source by deploying a novel multicrystal scheme, generating 5.6 W of green power for 10 W of fundamental power at an overall efficiency as high as 56%. A systematic study of this novel scheme at different stages was performed. Effect of dispersion in air on the inter-crystal spacing has been discussed along with the involved thermal effects. To our knowledge, the conversion efficiency of 56% is the highest in cw SP-SHG achieved to date, using bulk QPM or birefringent nonlinear crystals.

As a direction for the future, one important consideration, not addressed in this thesis, is the continuous tuning of a cw OPOs. Intracavity elements such as etalons can be used to achieve continuous tuning of the cw OPO. Etalon narrowed OPOs may be tuned by adjusting the etalon tilt, the temperature of solid etalons, or the mirror spacing of air spaced etalons. Continuous tuning can also be achieved by using diffraction gratings. Improving the stability of the cw OPO requires better

temperature control necessitating the need the efficient oven designs. Apart from these improvements, new nonlinear materials for picosecond mid-IR generation can be explored. Future possible developments of this work include development of cw OPOs tunable in the spectral region beyond 5 μm using cascaded OPO schemes based on OP-GaAs and ZGP, Tm-fiber laser pumped cw OPOs for the mid-IR, deploying internal frequency doubling schemes in both cw and picosecond OPOs, resulting in the generation of high power near-IR radiation in the Ti:sapphire wavelength range, based on fiber laser pumping and extending the novel multicrystal scheme presented in this thesis to generate high-power UV radiation. Investigations in these directions are already ongoing.

Bibliography

[1] M. Ebrahim-Zadeh and I. T. Sorokina, "Mid-Infrared coherent sources and applications," 1st ed. (Springer, 2007).

[2] C. L. Tang and L.K. Cheng, "Fundamentals of optical parametric processes and oscillators" in Laser science and technology series,Vol-10, Harwood academic publishers (1995).

[3] M. Ebrahim-Zadeh, "Mid-Infrared ultrafast and continuous-wave optical parametric oscillators" in Solid-State Mid-Infrared Laser Sources, Springer-Verlag (2003).

[4] M. Ebrahim-Zadeh, "Continuous wave optical parametric oscillators," Handbook of optics, 3rd ed. (Optical Society of America, Washington, D.C.), Vol. 4, Chapter. 17 (2010).

[5] M. F. L 'Annunziata, "Radioactivity-Introduction and history," Elsevier (2007).

[6] E. Schrodinger, "Nonlinear optics," Proc. Royal Irish Academy 47 A, 77-117 (1942).

[7] E. Schrodinger, "A new exact solution in non-linear optics," Proc. Royal Irish Academy 49 A, 59-66 (1943).

[8] T. H. Maiman, "Stimulated optical radiation in ruby," Nature 187, 493-494 (1960).

[9] P. A. Franken, A. E. Hill, C. W. Peters, and G. Weinreich, "Generation of optical harmonics," Phys. Rev. Lett. 7(4), 118-119 (1961).

[10] M. Bass, P. A. Franken, A. E. Hill, C. W. Peters, and G. Weinreich, "Optical mixing," Phys. Rev. Lett. 8 (1), 18 (1962).

[11] J. A. Giodmaine, "Mixing of light beams in crystals," Phys. Rev. Lett. 8 (1), 19 (1962).

[12] P. D. Maker, R. W. Terhune, M. Nissenoff, and C. M. Savage, "Effects of dispersion and focusing on the productionof optical harmonics," Phys. Rev. Lett. 8, 21-22 (1962).

[13] P. K. Tien, "Parametric amplification and frequency mixing in propagating circuits," J. Appl. Phys. 29(9) 1347-1357 (1958).

[14] P. K. Tien, and H. Suhl, "A traveling-wave ferromagnetic amplifier," Proc. IRE, 700-706(1958).

[15] R. W. Terhune, P. D. Maker, and C. M. Savage, "Optical harmonic generation in calcite," Phys. Rev. Lett. 8(10) 404-406 (1962).

[16] R. H. Kingston, "Parametric amplification and oscillation at optical frequencies," Proc, IRE, 50, 472 (1962).

[17] S. A. Akhmanov and R. V. Khokhlov, Zh. Eksperim. i Teor. Fiz., 43:351, 1962.

[18] N. M. Kroll, "Parametric amplification in spatially extended media and application to the design of tuneable oscillators at optical frequencies," Phys. Rev. 127(4), 1207-1211 (1962).

[19] J. A. Armstrong, N. Bloembergen, J. Ducuing, and P. S. Pershan, "Interaction between light waves in a nonlinear dielectric," Phys. Rev. 127(6), 1918-1939 (1962).

[20] A. W. Smith and N. Braslau, "Observation of an optical difference frequency," J. Appl. Phys. 34, 2105-2106 (1963).

[21] J. A. Giordmaine and R. C. Miller, "Tunable coherent parametric oscillation in $LiNbO_3$ at optical frequencies," Phys. Rev. Lett. 14(24) 973-976 (1965).

[22] Y. X. Fan, R. C. Eckardt, R. L. Byer, R. K. Route, and R. S. Feigelson, "$AgGaS_2$ infrared parametric oscillator,"Appl. Phys. Lett. 45(4), 313-315 (1984).

[23] M. J. Rosker and C. L. Tang, "Widely tunable optical parametric oscillator using urea," J. Opt. Soc. Am. B 2, 691-696 (1985).

[24] L. K. Cheng, W. R. Bosenberg, and C. L. Tang, "Broadly tunable optical parametric oscillation in $\beta - BaB_2O_4$," Appl. Phys. Lett. 53(3), 175-177 (1988).

[25] M. Ebrahim-Zadeh, A. J. Henderson, and M. H. Dunn, "An Excimer-pumped $\beta - BaB_2O_4$ optical parametric oscillator tunable from 354 nm to 2.370 μm," IEEE J. Quantum Electron. 26, 1241-1252, (1990).

[26] D. C. Edelstein, E. S. Wachman, and C. L. Tang, "Broadly tunable high repetition rate femtosecond optical parametric oscillator" Appl. Phys. Lett. 54 (18), 1728-1730 (1989).

[27] S. T. Yang, R. C. Eckardt, and R. L. Byer, "Continuous-wave singly resonant optical parametric oscillator pumped by a single-frequency resonantly doubled Nd:YAG laser," Opt. Lett., 18(12) 971–973 (1993).

[28] S. Matsumoto, E. J. Lim, H. M. Hertz, and M. M. Fejer, "Quasiphase-matched second harmonic generation of blue light in electrically periodically-poled lithium tantalate waveguides," Electron. Lett. 27, 2040-2042 (1991).

[29] W. R. Bosenberg, A. Drobshoff, J. I. Alexander, L. E. Myers and R. L. Byer,

"93%-pump depletion, 3.5-W continuous-wave, singly resonant optical parametric oscillator," Opt. Lett. 21(17) 1336–1338, (1996).

[30] M. Ghotbi, A. Esteban-Martin, and M. Ebrahim-Zadeh, "BiB_3O_6 femtosecond optical parametric oscillator," Opt. Lett. 31(21) 3128–3130 (2006).

[31] M. Ghotbi, A. Esteban-Martin, and M. Ebrahim-Zadeh, "Tunable, high-repetition-rate, femtosecond pulse generation in the ultraviolet," Opt. Lett. 33(4) 345–347 (2008).

[32] P. E. Powers, Thomas J. Kulp, and S. E. Bisson, "Continuous tuning of a continuous-wave periodically poled lithium niobate optical parametric oscillator by use of a fan-out grating design," Opt. Lett., 23(3) 159–161 (1998).

[33] A. J. Henderson and R. Stafford, "Intra-cavity power effects in singly resonant cw OPOs," Appl. Phys. B, 85 181–184 (2006).

[34] S. Chaitanya Kumar, R. Das, G. K. Samanta, M. Ebrahim-Zadeh, "Optimally-output-coupled, 17.5 W, fiber-laser-pumped continuous-wave optical parametric oscillator," Appl. Phys. B: Lasers Opt. 102 (1), 31-35, (2011).

[35] G. K. Samanta, G. R. Fayaz, Z. Sun, and M. Ebrahim-Zadeh, "High-power, continuous-wave, singly resonant optical parametric oscillator based on MgOsPPLT," Opt. Lett., 32(4) 400–402 (2007).

[36] R. Das, S. Chaitanya Kumar, G. K. Samanta, M. Ebrahim-Zadeh, "Broadband, high-power, continuous-wave, mid-infrared source using extended phase-matching bandwidth in MgO:PPLN," Opt. Lett. 34 (24), 3836-3838 (2009).

[37] S. Chaitanya Kumar and M. Ebrahim-Zadeh, "High-power, continuous-wave, mid-infrared optical parametric oscillator based on MgO:sPPLT," Opt. Lett. 36(13), 2578-2580 (2011).

[38] S. Chaitanya Kumar, A. Esteban-Martin, and M. Ebrahim-Zadeh, "Interferometric output coupling of ring optical oscillators," Opt. Lett. 36 (7), 1068-1070 (2011).

[39] S. Chaitanya Kumar, A. Agnesi, P. Dallocchio, F. Pirzio, G. Reali, K. T. Zawilski, P. G. Schunemann, and M. Ebrahim-Zadeh, "1.5 mJ, 450 MHz, CdSiP2 picosecond optical parametric oscillator near 6.3 µm," Opt. Lett. 36(16), 3236-3238 (2011).

[40] G. K. Samanta, S. Chaitanya Kumar, M. Ebrahim-Zadeh, "Stable, 9.6 W, continuous-wave, single-frequency, fiber-based green source at 532 nm," Opt. Lett. 34 (10), 1561-1563 (2009).

[41] S. Chaitanya Kumar, G. K. Samanta, M. Ebrahim-Zadeh, "High-power, single-frequency, continuous-wave second-harmonic-generation of ytterbium fiber laser in PPKTP and MgO:sPPLT," Opt. Exp. 17 (16), 13711-13726 (2009).

[42] G. K. Samanta, S. Chaitanya Kumar, K. Devi, and M. Ebrahim-Zadeh, "High power, continuous-wave Ti:sapphire laser pumped by fiber-laser green source at 532 nm," Opt Laser Eng (2011) (In press).

[43] G. K. Samanta, S. Chaitanya Kumar, K. Devi, and M. Ebrahim-Zadeh, "Multicrystal, continuous-wave, single-pass second-harmonic-generation with 56% efficiency," Opt. Lett. 35 (20), 3513-3515 (2010).

[44] S. Chaitanya Kumar, G. K. Samanta, K. Devi, M. Ebrahim-Zadeh, "High-efficiency, multicrystal, single-pass, continuous-wave second harmonic generation," Opt. Exp. 19 (12), 11152-11169 (2011).

[45] R. W. Boyd, "Nonlinear Optics," Academic Press, San Diego, USA (2007).

[46] R. L. Byer, "Optical parametric oscillator," in Treatise in Quantum Electronics, H. Rabin and C. L. Tang, eds. Academic, 587–702, (1975).

[47] S. E. Harris, "Tunable optical parametric oscillators," Proc. of IEEE, 57, 2096-2113 (1992).

[48] M. Ebrahim-Zadeh and M. H. Dunn, "Optical parametric oscillators," Handbook of optics, 2nd ed. (Optical Society of America, Washington, D.C.), Chapter. 22 (2000).

[49] R. L. Sutherland, "Handbook of nonlinear optics," second edition, Marcel Dekker, Inc., (1996).

[50] R.W. Munn and C. N. Ironside, "Nonlinear optical materials," CRC Press (1993).

[51] A. M. Weiner, "Ultrafast optics," Wiley series in pure and applied optics (2009).

[52] D. A. Kleinman, "Nonlinear dielectric polarization in optical media," Phys. Rev. 126,1977-1979 (1962).

[53] P. A. Franken and J. F. Ward, "Optical harmonics and nonlinear phenomena," Rev. Mod. Phys. 35, 23-29 (1963).

[54] B.Jaffe, W.Cooke, and H.Jaffe, "Piezoelectric Ceramics," Academic Press (1971).

[55] F. Zernike and J. E. Midwinter, "Applied nonlinear optics," Wiley (1973).

[56] M. M. Fejer, G. A. Magel, D. H. Jundt, and R. L. Byer, "Quasi-phase-matched second harmonic generation: Tuning and tolerances," IEEE J. Quantum Elect. 28, 2631-2654 (1992).

[57] A. Bruner, D. Eger, M. B. Oron, P. Blau, M. Katz, and S. Ruschin, "Temperature-dependent Sellmeier equation for the refractive index of stoichiometric lithium tantalite," Opt. Lett. 28, 194-196 (2003).

[58] D.S. Hum, M.M. Fejer, "Quasi-phasematching," C. R. Physique 8, 108-198 (2007).

[59] G. D. Boyd and D. A. Kleinman, "Parametric interaction of focused Gaussian light beams," J. Appl. Phys. 39, 3597-3639 (1968).

[60] J. A. Armstrong, N. Bloemberger, J. Ducuing and P.S. Pershan, "Interactions between light waves in a nonlinear dielectric," Phys Rev. 127, 1918-1939 (1962).

[61] M. Abramowitz and I. Stegun, "Handbook of Mathematical Functions," Dover: Newyork (1965).

[62] R. C. Eckardt and J. Reintjes, "Phase matching limitations of high efficiency second harmonic generation," IEEE J. Quantum Elect. 20, 1178-1187 (1984).

[63] D. Eimerl, "High average power harmonic generation," IEEE J. Quantum Elect. 23, 575-592 (1987).

[64] L. E. Myers, "Periodically Poled Lithium Niobate and Quasi-Phase- Matched Optical Parametric Oscillators," IEEE J. Quantum Electron. 33, 1663-1672, (1992).

[65] O. Paul, A. Quosig, T. Bauer, M. Nittmann, J. Bartschke, G. Anstett, and J. A. L'Huillier, "Temperature-dependent Sellmeier equation in the MIR for the extraordinary refractive index of 5% MgO doped congruent $LiNbO_3$," Appl. Phys. B: Lasers Opt. 86, 111-115 (2007).

[66] U. Ströβner, J. P. Meyn, R.Wallenstein, P. Urenski, A. Arie, G. Rosenman, J. Mlynek, S. Schiller, and A. Peters, "Single-frequency continuous-wave optical parametric oscillator system with an ultrawide tuning range of 550 to 2830 nm," J. Opt. Soc. Am. B 19, 1419-1424 (2002).

[67] J. T. Verdeyen, "Lasers Electronics," Third Ed., Prentice Hall, Englewood Cliffs, New Jersey (1995).

[68] S.M. Cristescu, S.T. Persijn, S. Te Lintel Eckert, F.J.M. Harren, "Laser-based systems for trace gas detection in life sciences," Appl. Phys. B: Lasers Opt. 92, 343–349 (2008).

[69] D. Chen and T. S. Rose, "Low noise 10-W cw OPO generation near 3 µm with MgO doped PPLN," CLEO, CThQ2 (2005).

[70] S. T. Lin, Y. Y. Lin, Y. C. Huang, A. C. Chiang and J. T. Shy, "3-µm Continuous-Wave Singly Resonant OPO," CLEO, CTull (2008).

[71] M. Vainio, J. Peltola, S. Persijn, F.J.M. Harren, L. Halonen, "Thermal effects in singly resonant continuous-wave optical parametric oscillators," Appl. Phys. B: Lasers Opt. 94, 411-427 (2009).

[72] A. Henderson and R. Stafford, "Spectral broadening and stimulated Raman conversion in a continuous-wave optical parametric oscillator," Opt. Lett. 32, 1281-1283 (2007).

[73] M.M.J.V. van Herpen, S. Li, S.E. Bisson, S. Te Lintel Hekkert, F.J.M. Harren, "Tuning and stability of a continuous-wave mid-infrared high-power single resonant optical parametric oscillator," Appl. Phys. B: Lasers Opt. 75, 329–333 (2002).

[74] P. Gross, M. E. Klein, T. Walde, K.-J. Boller, M. Auerbach, P. Wessels, and C. Fallnich, "Fiber-laser-pumped continuous-wave singly resonant optical parametric oscillator," Opt. Lett. 27, 418-420 (2002).

[75] I. D. Lindsay, B. Adhimoolam, P. Groß, M. Klein, and K. Boller, "110 GHz rapid, continuous tuning from an optical parametric oscillator pumped by a fiber-amplified DBR diode laser," Opt. Exp. 13, 1234-1239 (2005).

[76] M. Vainio, M. Siltanen, J. Peltola, and L.Halonen, "Continuous-wave optical parametric oscillator tuned by a diffraction grating," Opt. Exp. 17, 7702-7707 (2009).

[77] G. K. Samanta and M. Ebrahim-Zadeh, "Continuous-wave singly-resonant optical parametric oscillator with resonant wave coupling," Opt. Exp. 16, 6883-6888 (2008).

[78] G. K. Samanta and M. Ebrahim-Zadeh, "Continuous-wave, single-frequency, solid- state blue source for the 425–489 nm spectral range," Opt. Lett. 33, 1228-1230 (2008).

[79] L.B. Kreuzer, "Single and multimode oscillation of the singly resonant optical parametric oscillator," Proc. Joint Conf. Lasers and Opt.-Elect. p. 52-63 (1969).

[80] R. Sowade, I. Breunig, J. Kiessling, K. Buse, "Influence of the pump threshold on the single-frequency output power of singly resonant optical parametric oscillators," Appl. Phys. B: Lasers Opt. 96, 25-28 (2009).

[81] J. Kiessling, R. Sowade, I. Breunig, K. Buse, and V. Dierolf, "Cascaded optical parametric oscillations generating tunable terahertz waves in periodically poled lithium niobate crystals," Opt. Exp. 17, 87-91 (2009).

[82] J. J. Longdell, M. J. Sellars, and N. B. Manson, "Demonstration of Conditional Quantum Phase Shift Between Ions in a Solid," Phys. Rev. Lett. 93, 130503 (2004).

[83] G. K. Samanta, G. R. Fayaz, and M. Ebrahim-Zadeh, "1.59 W, single-frequency, continuous-wave optical parametric oscillator based on MgO:sPPLT," Opt. Lett. 32, 2623-2625 (2007).

[84] N. E. Yu, S. Kurimura, Y. Nomura, M. Nakamura, K. Kitamura, J. Sakuma, Y. Otani, and A. Shiratori, "Periodically poled near-stoichiometric lithium tantalate for optical parametric oscillation," Appl. Phys. Lett. 84, 1662-1664 (2004).

[85] H. Ishizuki and T. Taira, "High energy quasi-phase matched optical parametric oscillation using Mg-doped congruent $LiTaO_3$ crystal," Opt. Exp. 18, 253-258 (2010).

[86] T. Hatanaka, K. Nakamura, T. Taniuchi, H. Ito, Yasunori Furukawa, and Kenji Kitamura, "Quasi-phase-matched optical parametric oscillation with periodically poled stoichiometric $LiTaO_3$," Opt. Lett. 25, 651-653 (2000).

[87] B. Dayan, A. Pe'er, A. A. Friesem & Y. Silberberg, "Two Photon Absorption and Coherent Control with Broadband Down-Converted Light," Phys. Rev. Lett. 93, 0230051-0230054 (2004).

[88] T. Yanagawa, O. Tadanaga, Y. Nishida, H. Miyazawa, K. Magari, M. Asobe, and H. Suzuki, "Simultaneous observation of CO isotopomer absorption by broadband difference-frequency generation using a direct-bonded quasi-phase-matched $LiNbO_3$ waveguide," Opt. Lett. 31, 960-962 (2006).

[89] Ł. W. Kornaszewski, N. Gayraud, J. M. Stone, W. N. MacPherson, A.K. George, J. C. Knight, D. P. Hand and D. T. Reid, "Mid-infrared methane detection in a photonic bandgap fiber using a broadband optical parametric oscillator," Opt. Exp. 15, 11219-11224 (2007).

[90] P. E. Powers, T. J. Kulp, and R. Kennedy, "Demonstration of differential backscatter absorption gas imaging," Appl. Opt. 39, 1440-1448 (2000).

[91] D. Brida, C. Manzoni, G. Cirmi, M. Marangoni, S. De Silvestri, and G. Cerullo, "Generation of broadband mid-infrared pulses from an optical parametric amplifier," Opt. Exp. 15, 15035-15040 (2007).

[92] P. J. Phillips, S. Das, and M. Ebrahimzadeh, "High-repetition-rate, all-solid-state, Ti:sapphire-pumped optical parametric oscillator for the mid-infrared," Appl. Phy. Lett. 77, 469-471 (2000).

[93] F. Adler, K. C. Cossel, M. J. Thorpe, I. Hartl, M. E. Fermann and J. Ye, "Phase-stabilized, 1.5 W frequency comb at 2.8–4.8 μm," Opt. Lett. 34, 1330-1332 (2009).

[94] W. R. Bosenberg, A. Drobshoff, J. I. Alexander, L. E. Myers and R. L. Byer, "Continuous-wave singly resonant optical parametric oscillator based on periodically poled $LiNbO_3$," Opt. Lett. 21, 713-715 (1996).

[95] A. Esteban-Martin, O. Kokabee, and M. Ebrahim-Zadeh, "Optimum output coupling in optical oscillators using an antiresonant ring interferometer," Opt. Lett. 35, 2786-2788 (2010).

[96] A. E. Siegman, "An antiresonant ring interferometer for coupled laser cavities, laser output coupling, mode locking, and cavity dumping," IEEE J. Quantum Electron. 9, 247–250 (1973).

[97] A. E. Siegman, "Laser beams and resonators: Beyond the 1960s," IEEE J. Sel. Top. Quantum Electron. 6, 1389-1399 (2000).

[98] W. S. Pelouch, S. Herrera, L.A. Schlie, P.E. Powers, and C.L. Tang, "Femtosecond Optical Parametric Oscillators," Proc. Soc. Photo-Opt. Instrum. Eng. 2166, 66 (1994).

[99] O. Kokabee, A. Esteban-Martin, and M. Ebrahim-Zadeh, "Efficient, high-power, ytterbium-fiber-laser-pumped picosecond optical parametric oscillator," Opt. Lett. 35, 3210-3212 (2010).

[100] G. Edwards, R. Logan, M. Copeland, L. Reinisch, J. Davidson, B. Johnson, R. Maciunas, M. Mendenhall, R. Ossoff, J. Tribble, J. Werkhaven and D. O'day, "Tissue ablation by a free-electron laser tuned to the amide II band," Nature 371, 416 - 419 (1994).

[101] J. Hildenbrand, J. Herbst, J. Wöllenstein, A. Lambrecht, "Explosive detection using infrared laser spectroscopy," Proc. of SPIE 7222 72220B (2009).

[102] P. G. O'Shea and H. P. Freund, "Free-Electron Lasers: Status and Applications," Science 292, 1853-1858 (2001).

[103] K. T. Zawilski, P. G. Schunemann, T. M. Pollak, D. E. Zelmon, N. C. Fernelius, and F. K. Hopkins, "Growth and characterization of large $CdSiP_2$ single crystals," J. Cryst. Growth 312, 1127-1132 (2010).

[104] V. Petrov, F. Noack, I. Tunchev, P. Schunemann, and K. Zawilski, "The nonlinear coefficient d36 of $CdSiP_2$," Proc. SPIE 7197, 71970M (2009).

[105] V. Petrov, P. G. Schunemann, K. T. Zawilski, and T. M. Pollak, "Noncritical singly resonant optical parametric oscillator operation near 6.2 μm based on a $CdSiP_2$ crystal pumped at 1064 nm," Opt. Lett. 34, 2399-2401 (2009).

[106] V. Petrov, G. Marchev, P. G. Schunemann, A. Tyazhev, K. T. Zawilski, and T. M. Pollak, "Subnanosecond, 1 kHz, temperature-tuned, noncritical mid-infrared optical parametric oscillator based on $CdSiP_2$ crystal pumped at 1064 nm," Opt. Lett. 35, 1230-1232 (2010).

[107] A. Peremans, D. Lis, F. Cecchet, P. G. Schunemann, K. T. Zawilski, and V. Petrov, "Noncritical singly resonant synchronously pumped OPO for generation of picosecond pulses in the mid-infrared near 6.4 μm," Opt. Lett. 34, 3053-3055 (2009).

[108] O. Chalus, P. G. Schunemann, K. T. Zawilski, J. Biegert, and M. Ebrahim-Zadeh, "Optical parametric generation in $CdSiP_2$," Opt. Lett. 35, 4142-4144 (2010).

[109] V. Kemlin, B. Boulanger, V. Petrov, P. Segonds, B. Ménaert, P. G. Schunneman, and K. T. Zawilski, "Nonlinear, dispersive, and phase-matching properties of the new chalcopyrite $CdSiP_2$[Invited]," Opt. Mater. Express 1, 1292-1300 (2011).

[110] M. Sheik-Bahae, D. C. Hutchings, D. J. Hagan, E. W. V. Stryland, "Dispersion of Bound Electron Nonlinear Refraction in Solids," IEEE J. Quamtum Electron. 27, 1296-1309 (1991).

[111] P. F. Moulton, "Spectroscopic and laser characteristics of Ti:A12O3," J. Opt. Soc. Am. B 3, 125-133 (1986).

[112] A. J. Alfrey, "Modeling of Longitudinally Pumped CW Ti: Sapphire Laser Oscillators," IEEE J. Quantum Electron. 25, 760-766 (1989).

[113] P. A. Schulz, "Single-Frequency $Ti : Al_2O_3$ Ring Laser," IEEE J .Quantum Electron. 24, 1039-1044 (1988).

[114] T. L. Boyd and H. J. Kimble, "Frequency stabilization of a continuous-wave Ti:sapphire laser, " Opt. Lett. 16, 808-810 (1991).

[115] J. Harrison, A. Finch, D. M. Rines, G. A. Rines, and P. F. Moulton, "Low-threshold, cw, all-solid-state $Ti : Al_2O_3$ laser," Opt. Lett. 16, 581-583 (1991).

[116] P. W. Roth, A. J. Maclean, D. Burns, and A. J. Kemp, "Directly diode-laser-pumped Ti:sapphire laser", Opt. Lett. 34, 3334-3336 (2009).

[117] B. Resan, E. Coadou, S. Petersen, A. Thomas, P. Walther, R. Viselga, J. M. Heritier, J. Chilla, W. Tulloch, and A. Fry, "Ultrashort pulse Ti:sapphire oscillators pumped by optically pumped semiconductor (OPS) pump lasers", Solid State Lasers XVII: Technology and Devices, SPIE, 6871, 687116 (2008).

[118] J. Klein and J. D. Kafka, "The Ti:Sapphire laser: The flexible research tool," Nature. Photon. 4, 289 (2010).

[119] G. K. Samanta, S. Chaitanya Kumar, R. Das, and M. Ebrahim-Zadeh, "Continuous-wave optical parametric oscillator pumped by a fiber laser green source at 532 nm", Opt. Lett. 34, 2255-2257 (2009).

[118] P. Albers, E. Stark, and G. Huber, "Continuous-wave laser operation and quantum efficiency of titanium-doped sapphire", J. Opt. Soc. Am. B 3(1), 134-139, (1986).

[120] P. A. Schulz and S. R. Henion, "Liquid-nitrogen-cooled $Ti : Al_2O_3$ laser", IEEE J. Quantum Electron. 27(4), 1039-1047, (1991).

[121] S. V. Tovstonog, S. Kurimura, and K. Kitamura, "High power continuous-wave green light generation by quasiphase matching in Mg stoichiometric lithium tantalite", Appl. Phys. Lett. 90, 051115 (2007).

[122] S. Sinha, D. S. Hum, K. Urbane, Y-w. Lee, M. J. F. Digonnet, M. M. Fejer and R. L Byer, "Room-temperature stable generation of 19 Watts of single-frequency 532-nm radiation in a periodically poled lithium tantalate crystal", J. Lightwave Technol. 26, 3866 (2008).

[123] S. V. Tovstonog, S. Kurimura, I. Suzuki, K. Takeno, S. Moriwaki, N. Ohmae, N. Mio, and T. Katagai, "Thermal effects in high-power CW second harmonic generation in Mg-doped stoichiometric lithium tantalate", Opt. Exp. 16, 11294 (2008).

[124] G. Imeshev, M. Proctor, and M.M. Fejer, "Phase correction in double-pass quasi-phase-matched second-harmonic generation with a wedged crystal", Opt. Lett. 23, 165 (1998).

[125] S. Spiekermann, F. Laurell, V. Pasiskevicius, H. Karlsson, and I. Freitag, "Optimizing non-resonant frequency conversion in periodically poled media", Appl. Phys B: Lasers and Optics 79, 211 (2004).

[126] R. Thompson, M. Tu, D. Aveline, N. Lundblad, and L. Maleki, "High power single frequency 780nm laser source generated from frequency doubling of a seeded fiber amplifier in a cascade of PPLN crystals", Opt. Exp. 11, 1709 (2003).

[127] J. M. Yarborough, J. Falk, and C. B. Hitz, "Enhancement of optical second harmonic generation by utilizing the dispersion of air", Appl. Phys. Lett. 18, 70 (1971).

[128] G. C. Bhar, U. Chatterjee and P. Datta, "Enhancement of second harmonic generation by double-pass configuration in barium borate," Appl. Phys. B 51, 317-319 (1990).